VILNIUS UNIVERSITY

CENTER FOR PHYSICAL SCIENCE AND TECHNOLOGY

DOVILĖ MEŠKAUSKAITĖ

SPECTROSCOPY OF DEFECTS IN WIDE BAND-GAP SEMICONDUCTORS AND HEAVILY IRRADIATED Si

Doctoral dissertation

Physical Sciences, Physics (02 P)

Vilnius, 2018

The dissertation was prepared at Vilnius University in 2014–2018.

Supervisor – Prof. Dr. Sc. Eugenijus Gaubas (Vilnius University, Physical Sciences, Physics – 02 P).

VILNIAUS UNIVERSITETAS

FIZINIŲ IR TECHNOLOGIJOS MOKSLŲ CENTRAS

DOVILĖ MEŠKAUSKAITĖ

DEFEKTŲ SPEKTROSKOPIJA PLAČIATARPIUOSE PUSLAIDININKIUOSE IR STIPRIAI APŠVITINTAME Si

Daktaro disertacija

Fiziniai mokslai, fizika (02P)

Vilnius, 2018

Disertacija parengta 2014 – 2018 metais Vilniaus universitete.

Mokslinis vadovas – prof. dr. Eugenijus Gaubas (Vilnius universitetas, fiziniai mokslai, fizika – 02P).

Table of Contents

List of abbreviations

AFM – atomic force microscopy

AT – ammonothermal

BELIV – barrier evaluation by linearly increasing voltage

CCD – charge coupled device

CCE – charge collection efficiency

CUD – capacitance device that is under test

CVD – chemical vapour deposition

CW – continuous-wave

DAP – donor-acceptor pair

DC – direct current

DD – dislocation density

DED – density of edge dislocations

DLTS − deep-level transient spectroscopy

DSD – densities of screw dislocations

ENR – electrically neutral region

ESR – electron spin resonance

FTIR – Fourier transform-infrared spectroscopy

GaN − gallium nitride

HPHT – high-pressure, high-temperature

HVPE – hydride vapour phase epitaxy

ICDC – injected charge drift current

LHC – Large Hadron Collider

MOCVD – metal-organic chemical vapour deposition

MW-PC − microwave probed photo-conductivity

NIEL – non-ionizing energy loss

OPO – optical parametric oscillator

PCB – printed circuit board

PG – pulse generator

PI-L – proton-induced luminescence

PL − photoluminescence

PPIS – pulsed photo-ionization spectroscopy

RMS – root mean square

SCR – space charge region

SER – stretched-exponential relaxation

SS – steady-state

TCT – transient current technique

TD – thermal donors

TDTL – temperature dependent trapping lifetime

TI – time-integrated

TR – time-resolved

TDD – threading dislocation density

WBG – wide band-gap

XRD – x-ray diffraction

1. Introduction

Wide band-gap (WBG) semiconductors exhibit superior material properties that make them beneficial compared to the conventional silicon (Si). Physical properties of the WBG semiconductors are suitable for device operation at high blocking voltages, high switching frequencies, and high temperatures [1,2]. The large threshold displacement energy for WBG semiconductors relative to Si and GaAs, is the essential feature for the radiation hardness of such materials [3]. Owing to this property, gallium nitride (GaN) and diamond materials are two of the most promising WBG semiconductors for fabrication of radiation tolerant particle detectors and solar-blind photo-sensors. The radiation hardness of detectors is important for application in harsh radiation environment at accelerator facilities, e.g. at CERN (European Organization for Nuclear Research), Fermilab (Fermi National Laboratory) and others. It is expected that the radiation damage over the lifetime of the experiments at the new generation accelerators (e.g. High-Luminosity LHC (HL-LHC)) will cause crucial impact on performance of the particle detectors [4]. This requires the deep experimental and theoretical efforts to handle radiation damage effects. From this point of view, it is very important to analyse the defects arising during the crystal growth and irradiations by high energy particles. Growth conditions make a tremendous impact on properties of the WBG semiconductors, as proven by many studies [5–11]. Therefore, characterization of defects is of paramount importance in evaluation of the material suitability for production of particle detectors. On the other hand, optimization of the growth processes is inevitable. GaN and diamond are well known as radiation hard materials [12,13]. However, there is a lack of detailed studies of defects in the pristine materials and their interaction with radiation induced defects, particularly in heavily irradiated samples. Experimental results presented in this thesis have been obtained by using photoluminescence, deep-level transient spectroscopy, microwave probed photo conductivity and other methods. These optical and electrical methods are commonly employed to detect and quantify defects and defect-related effects in semiconductors. In order to analyse radiation-induced defects, GaN samples

were irradiated by neutrons with fluences up to 5×10^{16} cm^{-2}. Such fluences are expected at tracking detector systems of CERN accelerator after 10 years of operation [4]. *In situ* measurements during proton irradiation were performed by combining the optical (proton induced luminescence (PI-L)) and electrical (barrier evaluation by linearly increasing voltage (BELIV)) methods in order to analyse the performance of thin MOCVD epilayer GaN-based sensors during irradiation by 1.6 MeV protons. Most of the earlier *in situ* investigations have been done by using ion irradiations [14,15], while very few studies have been performed to analyse *in situ* characteristics in MOCVD grown GaN during irradiation by hadrons [16]. Therefore, the monitoring of electrical and optical characteristics during hadron irradiations allow for trace evolution of performance of the LED-based sensors under harsh radiation.

Measurements of detector response, by using TCT technique [17], is a widely employed tool for the characterization of carrier transport features in the particle detectors. The TCT technique has been implemented in this studies using perpendicular and parallel injection of carrier domains (sheets). Since the fabrication of reasonable ohmic contacts in GaN and diamond by ion-implantation or radio frequency sputtering is rather difficult [18,19], the capacitor-type diamond detectors with pressed electrodes were used for the TCT measurements. Such structures are preferential for the investigations of the current transients in WBG semiconductors, which exhibit often the semi-insulating properties. Capacitor type detectors were made of different technology diamonds in order to reveal the impact of native defects on electrical properties of these detectors. The TCT measurements allow a direct evaluation of the most important parameters: carrier lifetime, mobility, space charge, and electric field configuration. In this work, the depth-distribution of native defects in diamond wafers has been identified within the profiles of current transients measured by scanning location of a focused injection beam.

Despite significant progress in development of WBG semiconductors based detectors, Si is the most used semiconductor for tracking detectors at

CERN. The donor removal and acceptor creation are most significant effects, which shorten the lifetime of the Si detectors. These effects lead to clustering of radiation defects [20]. The annealing procedures are commonly applied in order to extend the operation lifetime of particle detectors [21]. However, an identification of the radiation-induced defects becomes increasingly difficult due to extend densities of defects in heavily irradiated Si samples. Due to the large concentration of defects, the usage of two conventional methods, such as capacitance-mode deep-level transient spectroscopy or thermally stimulated currents, show limitations, e.g. the limit, inherent for C-DLTS, is determined by trap concentration, which must be less than 10% of the dopant concentration [22]. In this work, the annealing-induced transformations of defects in heavily irradiated Si have been studied by combining the current-mode deep-level transient spectroscopy and the temperature dependent carrier trapping lifetime techniques.

Objectives of research

● analysis of MW-PC transients in order to control the carrier recombination parameters of GaN and diamond materials;

● spectroscopy of technological and radiation induced defects for the comprehensive characterization of ammonothermally grown GaN (AT GaN) single crystals;

● analysis of carrier recombination mechanisms in MOCVD grown GaN epilayers;

● analysis of BELIV and PI-L characteristics in GaN-based sensors, recorded during 1.6 MeV proton irradiation;

● identification of technological defects in diamond materials grown by CVD and HPHT methods;

● analysis of the operational characteristics of the capacitor-type detectors based on HPHT and CVD diamond;

● identification of radiation-induced defects and their behaviour under annealing in heavily irradiated Si.

Scientific novelty and importance

The detailed investigations of technological and radiation-induced defects in AT GaN material have been performed. The impact of dopants (Mn and Mg) on the electrical and optical properties of the AT GaN material has been examined. This analysis revealed that AT GaN material is suitable for fabrication of the double-response particle sensors with properly low leakage currents. The long carrier lifetimes in AT GaN:Mg make this material applicable in formation of thick detectors. In contrast to AT GaN:Mg, GaN:Mn exhibit a short carrier lifetime. The material with short carrier lifetime is preferential for production of sensitive detectors with fast response time.

The dislocation-related effects on carrier recombination parameters in MOCVD GaN have been analysed by XRD and MW-PC techniques. Despite intense GaN research, there is still a lack of detail knowledge concerning the role of dislocations in anomalous diffusion phenomena related to random-walk processes.

The GaN-based sensors, which are suitable to detect both the electrical and optical signals in a harsh radiation environment, have been tested by performing the *in situ* BELIV and PI-L measurements during proton irradiation.

The model, based on Shockley-Ramo's theorem, has been proposed for the analysis of the drift-diffusion current transients of capacitor-type diamond detectors. This model is addressed to description of carrier transport, including trapping and detrapping mechanisms, in emulation of the operational characteristics of the capacitor-type detectors. The current transient profiling technique implemented through the cross-sectional scans of the injection location has been developed being a sensitive tool for tracing of the depth distribution of defects. This technique has been approved for native defect distribution in diamond samples. Different spectroscopic methods (ESR, FTIR, PPIS) have been developed and approved for the identification of native defects in CVD and HPHT diamond.

The effects of thermal annealing of the radiation-induced defects have been investigated in heavily hadrons irradiated Si detectors. The TDTL technique has

been developed for defect investigation, when standard techniques (e.g. DLTS) are not appropriate at high densities of defects.

Statements of the dissertation:

1. The Mg-doped AT GaN, semi-insulating material with sufficiently long carrier lifetimes, are suitable for detection of ionizing radiations with small interaction cross-section, while, GaN:Mn can be appropriate for production of fast response detectors.
2. The index β_{SER} of the stretched-exponential relaxation within the asymptotic stage of the excess carrier decay of MW-PC transient is relevant with the increase to adequately evaluated the disorder determined by threading dislocation density in MOCVD GaN epilayers.
3. MOCVD GaN-LED-based sensors are suitable to register simultaneously both the electrical and optical responses during irradiation by protons, and these detectors exhibit an enhanced radiation hardness owing to elevated doping level inherent for LED structures.
4. The developed detector operation models based on description of drift-recombination of the bipolar carrier domains correctly reproduce variations of detector response waveforms in the capacitor type detectors and are suitable for the reliable extraction of carrier mobility parameters.
5. TDTL technique is efficient method for spectroscopy and identification of radiation-induced defects in heavily hadron irradiated Si.

Author's contribution

The author performed majority of experimental measurements presented in the dissertation in collaboration with colleague dr. T. Čeponis, dr. J. Pavlov and dr. V. Rumbauskas. Measurements of FTIR and Raman spectra were performed in collaboration with PhD student M. Velička. The PPIS measurements with the spectrally tuned 40 fs excitation pulses were made in collaboration with Dr. R. Grigonis. AFM imaging, SS-, TR-, TI-PL and confocal microscopy PL measurements and XRD measurements were performed by co-

authors included in the list of authors [A4, A6]. The main analysis of experimental results has been performed by the author. Interpretation of results was implemented together with advisor Prof. Dr. Sc. E. Gaubas. Most of the drafts of publications were prepared by the author of the thesis under supervision of Prof. Dr. Sc. E. Gaubas.

Approbation of the research results
List of publications indexed by ISI:

[A1] E. Gaubas, T. Ceponis, D. Meskauskaite and N. Kazuchits, Profiling of current transients in capacitor type diamond sensors, *Sensors* 15, (2015) 13424.

[A2] E. Gaubas, T. Ceponis, D. Meskauskaite, R. Grigonis and V. Sirutkaitis, Spectroscopy of defects in HPHT and CVD diamond by ESR and pulsed photo-ionization measurements, *J. Instrum.* 11, (2016) C01017.

[A3] E. Gaubas, T. Ceponis, D. Meskauskaite and E. Simoen, Comparative study of current transients in HPHT and CVD diamond capacitor-sensors, *ECS J. Solid State Sci. Technol.* 5, (2016) P3101.

[A4] E. Gaubas, T. Ceponis, L. Deveikis, D. Meskauskaite, S. Miasojedovas, J. Mickevicius, J. Pavlov, K. Pukas, J. Vaitkus, et al., Study of neutron irradiated structures of ammonothermal GaN, *J. Phys. D. Appl. Phys.* 50, (2017) 135102.

[A5] E. Gaubas, T. Ceponis, D. Dobrovolskas, T. Malinauskas, D. Meskauskaite, S. Miasojedovas, J. Mickevicius, J. Pavlov, V. Rumbauskas, et al., Study of recombination characteristics in MOCVD grown GaN epi-layers on Si, *Semicond. Sci. Technol.* 32, (2017) 125014.

[A6] E. Gaubas, T. Ceponis, L. Deveikis, D. Meskauskaite, J. Pavlov, V. Rumbauskas, J. Vaitkus, M. Moll and F. Ravotti, Anneal induced transformations of defects in hadron irradiated Si wafers and Schottky diodes, *Mater. Sci. Semicond. Process.* 75, (2018) 157.

Publication in reviewed journal:

[A7] D. Meskauskaite, E. Gaubas, T. Ceponis, J. Pavlov and V. Rumbauskas, Characteristics of 1.6 MeV proton-irradiated GaN-based sensors, *RAD Assoc. J.* 2, (2017) 118.

List of the presentations in conferences:

1. D. Meskauskaite, T. Ceponis, E. Gaubas, J. Vaitkus, R. Grigonis, V. Sirutkaitis, Spectroscopy of defects in HPHT and CVD diamond by EPR and pulsed photo-ionization measurements. In 17th International Workshop on Radiation Imaging Detectors; Hamburg, 2015.
2. T. Ceponis, E. Gaubas, D. Meskauskaite, Comparative study of current transients in HPHT and CVD diamond capacitor type sensors. In 17th International Workshop on Radiation Imaging Detectors; Hamburg, 2015.
3. J. Pavlov, T. Ceponis, E. Gaubas, D. Meskauskaite, I. Reklaitis, J. Vaitkus, R. Grigonis, V. Sirutkaitis, Comparative study of deep levels in HVPE and MOCVD GaN by combining O-DLTS and pulsed photo-ionization spectroscopy. In 17th International Workshop on Radiation Imaging Detectors; Hamburg, 2015.
4. D. Meskauskaite, T. Ceponis, E. Gaubas, Srovės kinetikų profiliavimas deimanto kondensatorinio tipo dalelių detektoriuose. In 6th Conference of Young Scientists “Interdisciplinary investigations in Physical and Technological Science”; Vilnius, 2016.
5. V. Rumbauskas, D. Meskauskaite, T. Ceponis, E. Gaubas, Elektronais apšvitintų n- ir p- tipo Si bandinių mikrobangomis zonduojamo fotolaidumo temperatūrinių kitimų ir DLTS tyrimai. In 6th Conference of Young Scientists “Interdisciplinary investigations in Physical and Technological Science”; Vilnius, 2016.
6. D. Meskauskaite, T. Ceponis, E. Gaubas, Study of GaN material and radiation sensor structures. In 18th International Workshop on Radiation Imaging Detectors; Barcelona, 2016.
7. V. Rumbauskas, D. Meskauskaite, T. Ceponis, E. Gaubas, Anneal induced transforms of radiation defects in heavily electron irradiated silicon. In 18th International Workshops on Radiation Imaging Detectors; Barcelona, 2016.
8. D. Meskauskaitė, E. Gaubas, T. Ceponis, L. Deveikis, S. Miasojedovas, J. Mickevičius, J. Pavlov, K. Pūkas, J. Vaitkus, M. Zajac, R. Kucharski, Amonoterminiu būdu užauginto GaN tyrimai. In 7th Conference of Young

Scientists “Interdisciplinary investigations in Physical and Technological Science”; Vilnius, 2017.

9. D. Meskauskaite, E. Gaubas, T. Ceponis, V. Rumbauskas, J. Vaitkus, Anneal induced transforms of radiation defects in heavily irradiated Si detectors. In German Physical Society Spring Meeting; Dresden, 2017.
10. D. Meskauskaite, E. Gaubas, T. Ceponis, J. Pavlov, V. Rumbauskas, J. Vaitkus, M. Moll, F. Ravotti, C. Gallrapp, L. Makarenko, Anneal induced transforms of radiation defects in hadron and electron irradiated Si. In RD50-30th Workshop on Radiation hard semiconductor devices for very high luminosity colliders; Krakow, 2017.
11. D. Meskauskaite, E. Gaubas, T. Ceponis, L. Deveikis, J. Pavlov, K. Pukas, Evolution of GaN-based sensor characteristics during proton irradiation. In 5th International Conference on Radiation and Applications in Various Fields of Research; Budva, 2017.
12. L. Deveikis, T. Ceponis, E. Gaubas, D. Meškauskaitė, J. Pavlov, V. Rumbauskas, Iškaitinimų nulemtos radiacinių defektų transformacijos elektronais, protonais ir pionais apšvitintuose Si dariniuose. In 42th Lithuanian National Physics Conference; Vilnius, 2017.
13. D. Meskauskaite, E. Gaubas, T. Ceponis, J. Pavlov, V. Rumbauskas, Radiacinių defektų įtakos GaN spinduliuočių jutiklių charakteristikų kaitai tyrimai. In 42th Lithuanian National Physics Conference; Vilnius, 2017.
14. D. Meskauskaite, E. Gaubas, T. Ceponis, J. Pavlov, V. Rumbauskas, J. Vaitkus, M. Moll, F. Ravotti, Si and GaN for large fluence irradiation monitoring. In AIDA-2020 WP15 satellite meeting during 6th BTTB Workshop; Zurich, 2018.
15. D. Meskauskaite, E. Gaubas, T. Ceponis, J. Pavlov, V. Rumbauskas, S. M. Otajonov, N. E. Alimov, Comparative analysis of GaN and CdTe thin films for radiation detectors. In 6th International Conference on Radiation and Applications in Various Fields of Research; Ohrid, 2018.

Layout of the thesis

The thesis consists of six Chapters. Chapter 1 provides a short introduction, which includes goal and novelty of the work, statements of the dissertation, author's contribution and approval of the research results. General properties and applications of wide band-gap materials are presented in Chapter 2. In Chapter 3, the employed spectroscopy methods and other measurement techniques are described. In Chapters 4 and 5, the experimental spectroscopy results obtained on GaN and diamond structures, respectively, are presented and discussed. Also in Chapter 5, the dynamic carrier transport and detector current models based on Shockley-Ramo's theorem, are described, and results of current transient profiling are demonstrated. In Chapter 6, results of spectroscopy of the radiation-induced defects in heavily irradiated Si are discussed. In Chapter 7, the main results are summarized. List of references is provided at the end of the dissertation.

2. General properties and applications of wide band-gap materials

2.1. Basic properties of wide band-gap semiconductors

Wide band-gap (WBG) semiconductors exhibit superior material properties compared to the conventional semiconductor materials such as silicon (Si) or gallium arsenide (GaAs). Physical properties of the WBG semiconductors enable devices to operate at high blocking voltages, high switching frequencies, and high temperatures. Parameters, such as the bandgap, the breakdown field, the thermal conductivity, the saturated drift velocity of carriers and their mobilities for Si, 4H-SiC, GaN, natural and CVD diamond are compared in Table 2.1 [1]. The potential device applications are also noted.

Table 2.1 Comparison of physical parameters of Si, 4H-SiC, GaN, natural and CVD diamond [1].

	Si	**4H-SiC**	**GaN**	**Natural Diamond**	**CVD Diamond**	**Potential device application benefit**
Bandgap (eV)	1.1	3.2	3.44	5.47	5.47	High temperature
Breakdown field ($MVcm^{-1}$)	0.3	3	5	10	10	High voltage
Thermal conductivity ($Wcm^{-1}K^{-1}$)	1.5	5	1.3	22	24	High power
Electron saturation velocity ($\times 10^7 cm\ s^{-1}$)	0.86	3	2.5	2	2	High frequency
Hole saturation velocity ($\times 10^7 cm\ s^{-1}$)	n/a	n/a	n/a	0.8	0.8	
Electron mobility ($cm^2\ V^{-1}s^{-1}$)	1450	900	440	200-2800	4500	
Hole mobility (cm2 $V^{-1}\ s^{-1}$)	480	120	200	1800-2100	3800	

GaN and diamond materials exhibit the high breakdown field and high threshold displacement energy [23]. These properties are essential for fabrication of radiation tolerant particle detectors and solar-blind photo-sensors. However, presence of defects is unavoidable and plays a crucial role in determining of the optical and electrical properties of WBG semiconductors [24]. Different types of point defects and their complexes are formed during crystal growth and act as the undesirable carrier traps or recombination/generation centres. Identifying of the radiation defects, introduced by particles through energy loss due to ionizing processes and through NIEL (the non-ionizing energy loss) [25,26] is essentially important. The radiation-induced defects lead to harmful effects on operation of devices.

On the other hand, in some cases the defects are favourable and the production of advanced semiconductor devices require the introduction of specific defects in small areas of devices, e.g. single nitrogen-vacancy (NV) type defects in diamond might play a key role for implementations of quantum computing or fabrication of devices of the ultra-high density optical storage technology [27–29].

2.1.1. GaN: material properties and defect centres

Gallium nitride is a III-V group semiconductor with a direct bandgap of 3.4 eV [30]. GaN crystallizes in either the cubic crystal structure (zinc blende phase) or a hexagonal (wurtzite) crystal structure (Fig. 2.1).

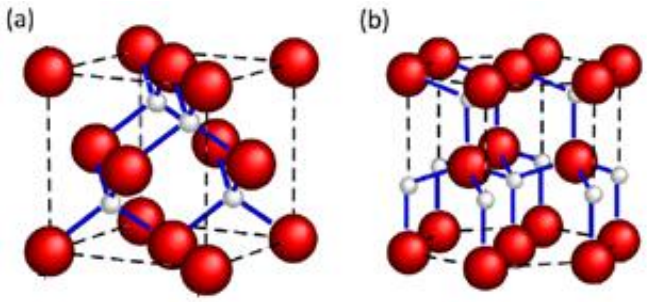

Fig. 2.1 Crystal structure of zinc-blende (a) and wurtzite (b) GaN [31].

The hexagonal wurtzite and cubic zinc blende GaN materials are two polytypes of the same material [31]. The both polytypes have similar crystallography. The bonds between the Ga ions and the N ions are tetrahedrally coordinated, and the inter-ionic distances within the close packed planes are approximately the same for both phases. Also, due to similar formation energy for both phases [32], it is possible that fractions of both polytypes can be formed during the growth, resulting in the imperfect crystal structure. Metalorganic chemical vapour deposition (MOCVD) and molecular beam epitaxy (MBE) technologies are widely used methods for growing of epitaxial III-V group semiconductors, such as GaN, GaAlN, InGaN, and InAlGaN. Large diameter sapphire and Si substrates are available at low cost, and these materials are widely used as substrates for GaN epitaxy [33]. However, the epitaxial growth of GaN on lattice-mismatched substrates (Sapphire: ~13.7 %, Si: ~17 % [33]) is the main reason for high density of dislocations. Also, discrepancy among

thermal conductivity coefficients between GaN epilayer and substrates leads to thermally induced strain. Great progress has been made in solving these problems by growing buffer layers [34], using ELOG [35] (Epitaxial lateral overgrowth) technique or by nitridation [36,37]. The methods, such as dislocation elimination by epitaxial growth with inverse-pyramidal pits (DEEP) [38], void-assisted separation [39] or cross-stacked carbon nanotubes [40] have been developed for the production of freestanding GaN. For some applications, e.g. GaN-on-GaN LEDs and GaN-based laser diodes, the bulk GaN seed are necessary to reduce formation of the non-radiative recombination centres, to increase of carrier lifetime, etc. [41]. Hydride vapour phase epitaxy (HVPE), Na-flux, and ammonothermal (AT) methods are commonly used for growth of the large scale GaN substrates (Table 2.2) [42,43]. These technologies are developed to obtain high quality and crack-free bulk GaN [44].

Table 2.2 The comparison of different GaN growth methods [43].

Growth method	HVPE	AT	Na-flux
Conditions	1 atm, 1000−1100 C	400 MPa, 600 C	5–10 MPa, 600–900 C
Growth rate	100−500 μm/h	0.1 mm/day	20−30 μm/h
Quality	Normal	High	High
Thickness	mm-scale	cm-scale	< 10 mm
Mass production	Good	Good	Good
Cost	Cheap	Expensive	Expensive

Despite of significant improvements of structural quality, achieved in recent years, formation of defects during growth is unavoidable. The defects usually are classified based on dimensionality [45] as:

● point defects (0D), associated with a single atomic site (e.g. vacancies),

● line defects (1D), associated with a direction (e.g. dislocations),

● planar defects (2D), associated with an area or a plane (e.g. grain boundaries, stacking faults, inversion domain boundaries and twins). Planar defects refer to the boundary between two crystalline regions of a crystal.

● volume defects (3D), associated with the changes in crystal pattern over a finite volume (e.g. voids, nano pipes and cracks).

Formation of point defects, e.g. vacancies, incorporation of the interstitials and substitutional atoms into a crystal lattice, strongly depends on growth conditions. Proper growth conditions allow to reduce the density of point defects to a negligible level. Substitutional impurities can be introduced into the crystal either intentionally (as a controlled doping) or unintentionally (as contaminants) during the various growth or treatment processes. The common unintentional substitutional impurities in GaN are oxygen (O) and carbon (C). Oxygen usually occupies N sites [37]. Calculations show that carbon is an amphoteric impurity in GaN, where C_{cation} is a shallow donor, while carbon in nitrogen sites (C_N) is a rather shallow acceptor [46]. The incorporation of C_N is preferable since the formation energy is rather low [37]. Dislocation densities can now be reduced to low densities as 10^3 cm^{-2}, e.g., AT GaN crystals, grown on HVPE-GaN seeds, contain dislocation density of about 7×10^4 cm^{-2} [47] or less than ~10^3 cm^{-2} when using the small-size seeds ('point seed') [48]. The planar defects are boundaries between regions of different crystallographic orientations. The most of planar defects are introduced owing to the vertical mismatch of lattices or the disordering of crystallographic planes (also named, stacking faults). Epitaxial growth of GaN on Si-substrates (GaN-on-Si) leads to formation of volume defects, such as cracks [33]. For the films, those are under a uniform stress σ, cracking occurs when the thickness reaches a critical value. Theoretical estimations show that tangential strains lead to formation of cracks, if the thickness of an epitaxial GaN layers, grown on Si(111), is higher than the critical value h_{crit} [49]. The critical value can be estimated as: $h_{crit} = E^*\Gamma/Z\sigma^2$, where $E=E/(1-\upsilon^2)$ – is the Young's modulus, υ – is the Poisson's ratio (0.18 for GaN [50]), Γ – is the parameter of layer resistivity determined by the hardness value. Γ is equal to 2γ for the pure brittle fracture, where γ is the specific surface energy (1.95 for GaN [51]), Z=1.976 for a homogeneous layer of GaN. Estimation of h_{crit} value for GaN/AlN/Si structures shows that h_{crit} equals to ~250 nm for GaN grown on Si (with a buffer AlN-layer of 100 nm) [52] and for the GaN/Si structure with a gradient buffer AlGaN-layer h_{crit} is increased up to 1 μm [53].

Although the GaN-based devices have been commercialized, a few issues for reliability and for applications are still necessary to examine.

2.1.2. Diamond: material properties and defect centres

Diamond is a wide band-gap semiconductor with an indirect bandgap E_g = 5.47 eV at room temperature [2]. Each carbon atom in diamond lattice has four neighbours, forming a tetrahedron (Fig. 2.2). The three-dimensional stability of the tetrahedral bonding arrangement and the short length of the C-C bond are responsible for material hardness [54].

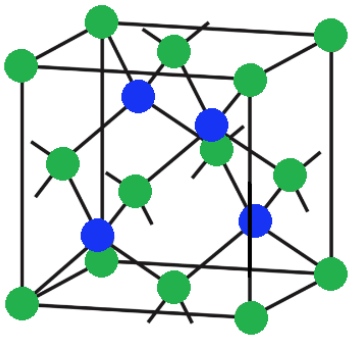

Fig. 2.2 Crystal structure of diamond [55].

The superior physical properties and chemical stability make diamond promising material for fabrication of devices, which are suitable to use in extreme environments (harsh radiation and high temperature) [2].

Diamond exhibits the highest electron and hole mobilities at room temperature over those inherent for other WBG semiconductor. Electron and hole mobilities are reported to be 4500 $cm^2V^{-1}s^{-1}$ and 3800 $cm^2V^{-1}s^{-1}$, respectively, for high quality single-crystal diamond grown by CVD method [56]. Impurity scattering causes a drop of mobility [2]. However, the doping of diamond is an extremely difficult process, particularly to get the n-type material.

The HPHT and CVD are two the most developed methods for manufacturing of synthetic diamond. Synthetic diamond is widely known as CVD diamond or HPHT diamond, referring to crystal formation methods. The combination of high pressure (5−6 GPa) and high temperature (1300−1500 °C), required for implementation of the HPHT growing method, causes the carbon atoms to deposit on the surface of the seeds [57]. CVD technique utilizes deposition of carbon atoms on the substrate of diamond seeds from the gaseous

phase at near-atmospheric pressures and with temperatures below 1000 °C [58]. Over the past decade, there have been major progress in the production of high quality CVD diamond. Moreover, CVD method is more superior than HPHT owing the possibility to grow both, very high purity single-crystalline and poly-(or nano)-crystalline diamond. Single crystal, polycrystalline (μm grain size) and nanocrystalline (5 nm to 100 nm grain size) forms, with wafer sizes up to 25 mm (in single-crystal form) and 200 mm (in the non-single crystal form) are available nowadays.

Diamond has the elementally carbon crystal structure, formed from pure carbon. However, chemical impurities cannot be avoided during formation of the natural or synthetic diamonds. The dominant impurity atoms in diamond are hydrogen, nitrogen and boron. Impurities modify many properties of diamond material.

Diamond can be classified into two types according to the N concentration. Type I diamond contains significant nitrogen concentration, whereas type II diamond is considered as containing low nitrogen concentration, which is non-detectable (less than 20 at ppm [11]) by infrared or ultraviolet absorption measurements [59]. Almost all natural diamonds are type I, which can be subdivided into type Ia and type Ib, depending on the nitrogen (N) attributed defects. The N atoms in type Ia diamond are present in various aggregated forms (e.g. paired N, double paired N), whereas in type Ib diamond, they are dispersed in isolated substitutional sites [11]. Ib is the common type of the synthetic diamond [11]. The classification of diamond types is presented in Table 2.3 [60].

Table 2.3 Classification of colours and states of existence of N in natural diamonds [60].

Type of diamond	Colour	State of existence of N				Rate of natural existence
		Isolated N	Paired N	Double paired N	Triple N	
Ia	Colourless	No	Yes	Yes	No	10%
Ia	Pale yellow	No	Yes	Yes	Small	90%
Ia	Yellow	Yes	Yes	Yes	Yes	
Ia	Brown	Large	Yes	Yes	Large	
IIa	Colourless	No	No	No	No	1%
Ib	Light yellow	Yes	No	No	No	0.2%
IIb	Blue	No (contains B)	No	No	No	Almost 0%

Type II diamond can be subdivided into type IIa and type IIb depending on the concentration of boron (B). Type IIa diamond is usually colourless, whereas type IIb diamond exhibits blue colour due to the B impurities. The presence of substitutional B acceptors, that are uncompensated (due to a lack of N donors), leads to the p-type conduction material. Nitrogen exists as a simple point defect or as their aggregates. N defects are often linked by making complexes with lattice vacancies (V) or with other impurities. Vacancies are usually produced by radiation damage in order to create the NV complex (Fig. 2.3a) [61]. The NV complex (owing to the structure of energy level (Fig. 2.3b)) has advantageous optical and electron spin properties. Therefore, diamond with NV defects is promising in applications for quantum computing, for production of the nanoscale sensors applied in physics and biology [62].

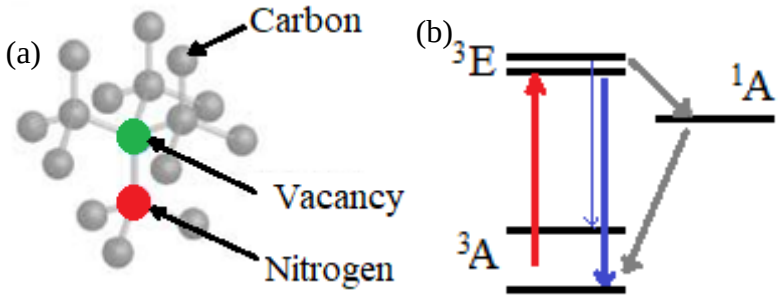

Fig. 2.3 a - structure of a diamond containing NV defect, b - the energy level scheme of the NV defect centre in diamond showing non-radiative decay from the ^{3}E (m_s=±1) excited state [61,63]. The ^{3}A is the ground state and the ^{3}E is excited state, the ^{1}A state located in between them.

NV defects can be generated by *ex-situ* ion-beam nitrogen implantation combined with anneal treatments or directly grown-in by intentionally adding nitrogen to the gas phase during crystal growth by the microwave plasma assisted CVD (MW-PACVD) method [10,63].

Hydrogen atoms are very small and usually act as the interstitial defects, incorporated in to lattice during growth (hydrogen is a precursor in the CVD growth process). Hydrogen usually is the undesirable technological impurity due to the passivation of the electrically active boron and phosphorus in p-type [64] and n-type diamond [65], respectively. Nitrogen and boron atoms are similar in size to carbon atoms and, therefore, are incorporated in substitutional diamond lattice sites. Nitrogen and phosphorous introduce donor level at ~1.37 eV and at

~0.52 eV, below the conduction band, respectively, while boron introduces quite shallow acceptor level at 0.37 eV above the valence band. Boron is commonly found in natural type IIb diamond. Boron doped diamond material can be produced by ion-implantation or by boron-source precursors during growth via CVD method [66]. n-type doping of diamond is more complicated [66]. The breakthrough in n-type doping came with the finding that the phosphorus dopants yield a relatively shallow energy. Phosphorus atoms can be introduced into an electrically active site by microwave enhanced plasma CVD using phosphine (PH3) as a dopant source. [66,67]. The planar (2D) and volume (3D) defects are quite rare in bulk-diamond grown by HPHT or CVD methods. However, extended defects, e.g. planar defects and small voids, are commonly observed in the diamond films [68,69]. The platelets are the planar defects, that are only found in type Ia natural diamond, i.e. those containing nitrogen predominantly in aggregated forms [69], and in synthetic type Ib diamonds after HPHT treatment at temperatures above 2700 °C [70]. The platelets size ranges from nm to a few μm [71]. These platelets were first resolved by x-ray diffraction measurements in the year 1940 [72]. However, an accurate determination of the atomic structure of the platelet defect and the role of the nitrogen is still unknown [73]. Later simulations of the structure and properties of the planar platelet using *ab initio* theory suggests that the carbon self-interstitials and the interstitial carbon atom, positioned between atomic sites, plays the important role in formation of these defects [69]. The grain boundaries between crystalline regions act as trapping centres and reduce carrier mobility. These various defects, including the point defects, the extended defects, and the surface defects, determine centres of carrier scattering, trapping and recombination, those affect the device performance.

2.2. Wide band-gap semiconductor device applications

WBG semiconductors are applied in many areas of industry of the opto-electronics, high frequency and high power devices industry. Devices, manufactured using WBG semiconductors, have demonstrated numerous benefits as compared to the conventional Si based devices, e.g. exhibiting the

better performance at the higher operating temperatures, the faster switching speed, and the higher breakdown voltage [41]. Very low leakage current, the enhanced radiation hardness, and an ability to operate at room temperature make GaN and diamond the most promising materials for detectors of various radiations [74]. Nevertheless, further studies of the radiation-induced defects are essential for the development of WBG semiconductor based detectors.

The intensive investigations of the GaN-based devices began in 1969, where the deposition of polycrystalline-GaN on a foreign substrate was demonstrated by using a vapour-phase technique, [75]. Fabrication of the field-effect transistors and power devices, based on GaN only recently became available commercially [76]. The GaN-based devices are also widely employed for opto-electronic applications (light emitting diodes and laser diodes) with remarkable advantages. Various other applications of the devices as full colour displays, the high density optical storage elements, and light communication, photovoltaic, and biotechnology components are permanently being developed from an early stage of mass production [77]. However, despite of successful applications of GaN-based devices in wide areas, there are still several issues, namely, effects of the high density of defects and strain-induced polarization [78,79]. GaN and its alloys (AlGaN) become the preferential materials for ultraviolet (UV) radiation detectors owing to the capability of the band gap tuning in the range from 3.4 eV to 6.2 eV. Studies of advanced GaN materials also were performed to reveal their potential applications as sensing materials for deep UV photodetectors, by using Schottky barrier, metal-semiconductor-metal junctions, and pin photodiode structures [80]. Beneficial properties of GaN, e.g. the large bandgap (3.39 eV), the high thermal stability (with melting point at 2500 ˚C), and large displacement energy (for N atoms 109 eV and for Ga: 45 eV) in GaN lattice, make GaN material to be attractive for high energy particle detectors and dosimeters. Work in this research area is still within an early development stage. However, the sandwich GaN-based devices, the GaN of mesa, pin structures, metal-semiconductor-metal and Schottky junctions,

have already shown abilities to detect UV light, x-rays, alpha particles, electrons, and neutrons [12].

For device applications, synthetic diamond is drawing an attention owing its superior physical features. Diamond based devices would be far better than devices based either on Si or other WBG materials. A significant progress in diamond based electronics has been made since 2002, and the key components of diamond industry, as manufacturing of the electronic-grade materials, fabrication of the tentative devices, and development of the contact deposition techniques, were considerably evaluated [1]. The GaN epilayers are promising in many applications. However, the layer growth on the substrates with lattice mismatch leads to structural defects, which significantly affect the performance of devices. Formation of structural defects minimized by manufacturing the devices using homoepitaxy on native material [81,82]. The difficulties related to the n-type diamond formation result in commercial applications of diamond electronic devices are addressed exceptionally on production of the unipolar (p-type) and the metal semiconductor FET structures [1]. Reliable operation of such the devices has been successfully demonstrated [83,84]. The exceptional properties of the diamond material, featuring the high mechanical and dielectric strength together with parameters of elevated carrier mobility and thermal conductivity, the diamonds can be an ideal semiconductor for industry of the high power transducers. The latter applications requires switching of currents and voltages in the range of several tens of kA and kV with current rise-times of a few ns duration [74]. It has been shown that detectors, based on polycrystalline diamond, can be exploited to detect ultraviolet radiation at wavelengths shorter than 225 nm. The relevant response in the visible region can also be achieved [74]. However, the problems related with carrier trapping/detrapping give rise both in polycrystalline and single-crystal material, which are not properly understood [74]. Applications of diamond based dosimeters in radiotherapy fields are shown feasible dynamic range of the linear response and long-term stability of such the devices. This is an important advantage, when comparing with Si dosimeters. The diamond dosimeters are almost quanta independent for

a very wide energy range of photons and of the dose accumulated during previous exposures [74]. The large values of the displacement energy (42 eV/atom) as well as the large saturation velocity (220 μm/ns) of carrier, combined with a large breakdown field (10^7 V/cm) make the diamond a promising material for the high energy particle detection, with very fast response [74]. Significant improvements in growth of electronic-grade CVD diamond have been made during recent years in growing high electrical quality CVD material [74]. However, the synthetic diamond is expensive and available in rather smaller pieces when comparing with Si or other WBG semiconductors (GaN or SiC). Nevertheless, an opinion exists, that diamond is a future generation semiconductor. Although, the synthetic diamond industry is at lower stage of evolution when comparing with that of GaN or SiC semiconductors, which are far more developed [85].

Silicon carbide (SiC), an another WBG material gains acceleration during the latest years in application of power device and radio-frequency field-effect transistor (RF FET) fabrication. SiC has also exhibit the ability to detect ionizing radiations of various types, such as alphas and betas, x-rays, gamma radiations, irradiations with radionuclide and monoenergetic neutrons. SiC-based detectors are operational in a wide range of temperatures [86]. However, a significant amount of the intrinsic structural defects and impurities are introduced during growth of SiC crystales. Also, there appear difficulties in doping of SiC material [87].

3. Experimental methods and techniques

3.1. Evaluation of structural characteristics

The structure characteristics of the samples have been investigated by x-ray diffraction (XRD) analysis and by imaging obtained using atomic force microscopy (AFM) as well as confocal microscopy. In this work, these techniques were mostly applied for investigation of GaN epilayers grown by MOCVD technology on Si substrates (GaN-on-Si). For GaN-on-Si technology, the usage of the MOCVD growth technique leads to a high density of screw and edge dislocations, threading the GaN layer. Introduction of high dislocation densities happens due to the large lattice and thermal mismatch between Si and GaN [88,89]. Performed analysis of structural defects was the initial step in methodology of comprehensive characterisation of the recombination properties in the MOCVD grown GaN epilayers on Si.

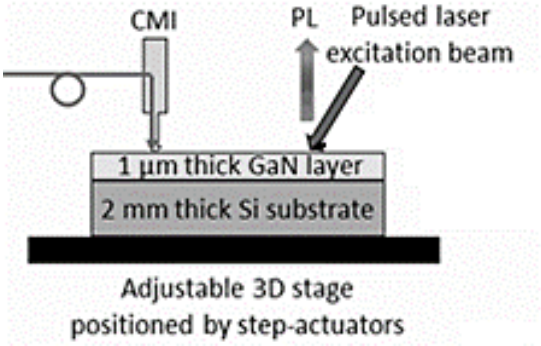

Fig. 3.1 A sketch of the sample positioning for confocal microscopy imaging [A5].

The confocal microscopy imaging (Fig. 3.1) was implemented by using an UV continuous-wave (CW) laser and a microscope *Alpha*300-*WITec*. The spatial distribution of the PL intensity was studied with a sub-micrometer spatial resolution. For the enhanced spectral resolution, the microscope was coupled with an UHTS 300 spectrometer an optical fibre. The excitation beam of a CW He-Cd laser was focused onto the sample using a high numerical aperture (NA = 0.9) objective. This ensured that the in-plane spatial resolution is approximately of 220 nm.

The composition of the nucleation and stress management layers was controlled by an x-ray diffractometer (HRXRD, Rigaku, SmartLab). The $\omega/2\Theta$ configuration [5,90] was employed in the x-ray diffraction measurements.

The atomic force microscopy (AFM) was used to examine surface morphology for GaN-on-Si samples. The surface properties were characterized using tapping mode AFM coupled with a Bruker Dimension Icon system. TappingMode AFM is a Bruker-patented technique which enables imaging at atomic level, when contact mode with noise floor less than 30 pm is implemented [91].

3.2. Measurement regimes and techniques for electro-optical characterization

3.2.1. Transient current technique

Measurements of current transients were performed at room temperature using a strip-line PCB by employing a common circuit for the TCT system (Fig. 3.2). The strip-line PCB is commonly employed for the reliable measurements of short current pulses in materials with large carrier mobility and in order to reduce the electrical noises [92–94].

The scheme for the TCT measurements (Fig. 3.2) consists of the r_{lm}=47 kΩ resistance used for limitation of the C_S=50 nF capacitor charging current. For biasing of the capacitor C_d under test device (CUD), CUD is connected in series with a direct current (DC) voltage U source and r_{lm}. A circuit for pulsed signal is then comprised of the charging source capacitor C_S, of the sample capacitor C_d and the load resistor R_{L1}=50 Ω connected in series. The 50 Ω coaxial cable is loaded by R_{L2}=50 Ω on its output and at the input of a TDS-5104 1 GHz band oscilloscope. The time parameters, evaluated for the electrical and excitation pulse rise, lead then to the overall time-resolution $\Delta t \cong$500 ps, in these experiments.

The parallel (Fig. 3.2a) and perpendicular (Fig. 3.2b) measurement geometries were implemented, when the directions of excitation beam and the applied electric field are parallel and perpendicular, respectively. The injected charge drift current (ICDC) transients were profiled by the applied DC voltage for the parallel measurement geometry. Excitation of the excess carriers was

performed through the transparent electrode or a hole an opening within a metal electrode of about 1 mm diameter.

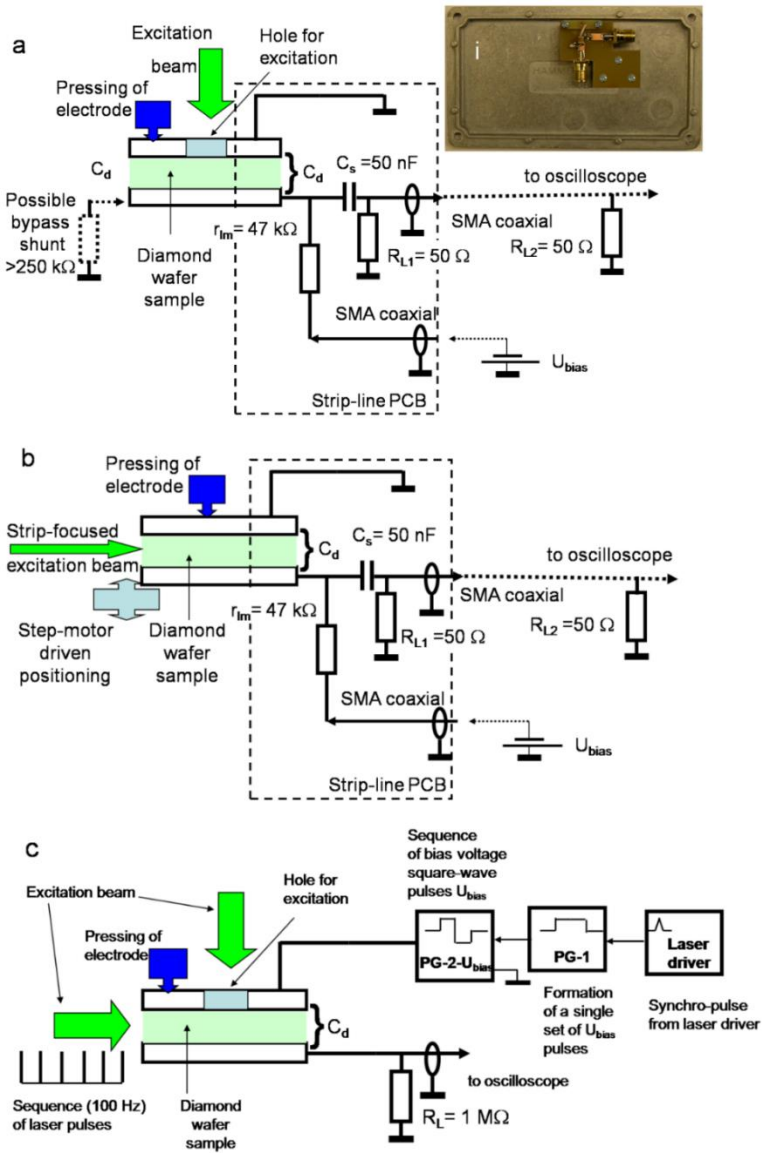

Fig. 3.2 Schemes exploited for the recording of current transients using the parallel (a, the inset shows a picture of PCB) and the perpendicular (b) profiling regimes. The DC bias voltage, varying bypass shunt has been applied within the circuit (a) for the investigation of relaxation features of the polarization effect. A scheme for examination of the polarization effect by using pulsed applied voltage synchronized with a sequence of laser excitation pulses is shown in (c). [A1].

The non-focused laser beam (Fig. 3.2a and c) was also used for the bias voltage profiling of currents by injection of bulk excess carrier domain if a diameter of the perpendicularly impinging beam either covers or is close to a dimension of the inter-electrode gap. For the localized (surface plane) charge

domain injection, sharply focused laser beam was used for the perpendicular measurement geometry.

For the investigation of the polarization effect, a shunt of rather large resistance (Fig. 3.2a) or pulsed biasing voltage (Fig. 3.2c) were employed. The pulse bias voltage of various durations (these significantly exceed a laser pulse repetition rate (100 Hz)) was applied (Fig. 3.2c), in order to monitor CUD charging currents and relaxation characteristics of their amplitudes. To govern synchronization, delays and formation of a long chain of square-wave pulses, triggered by a single laser pulse, two pulse generators (PG, Fig. 3.2c) were exploited. The first one (PG-1) synchronized from a single laser pulse has been used to form a long pulse, which governs the generator (PG-2) of square-wave pulses of voltage. The latter PG-2 generates a chain of square-waves of either unipolar or bipolar voltage pulses. The CUD charging currents are recorded by an oscilloscope using 1 MΩ load resistance.

The dominant carrier generation processes were identified by measurements of the pulsed optical transmission as a function of excitation power density and the dependence of electrical response signals on excitation. One ns temporal resolution DET-10A Si detectors and calibrated optical PM-100D power-meter were used in these measurements. The geometrical parameters of the focused laser beams were evaluated by using the knife-edge and the CCD camera-based beam-shape profilers. The single side outspread at a $0.1I_0$ level of light intensity within a focused beam is about of 20 μm relative to the peak intensity I_0. In the case of the perpendicular measurement geometry, profiling of the drift current transients was performed by changing the position of the injected domain within the inter-electrode space by using 3D micrometric positioning stage.

3.2.2. Barrier evaluation by linearly increasing voltage

The technique of barrier evaluation by linearly increasing voltage (BELIV) was employed for temperature-dependent BELIV measurements and *in situ* measurements during LED irradiation by protons (Fig. 3.4). BELIV technique

is based on analysis of the transients of barrier and diffusion capacitance changes. This technique allows the separation of the components of barrier capacitance (C_b) charging and generation/recombination currents. The impact of deep defect centres on barrier and diffusion capacitance can be estimated by analysis of BELIV kinetics.

The BELIV technique for a reverse biased diode is based on analysis of the changes of C_b with linearly increasing voltage $U_p(t)=At$ pulse, where $A=U_P/\tau_{PL}$ is a ramp of the linearly increasing voltage pulse with U_P peak amplitude and τ_{PL} duration. The barrier capacitance for a non-biased diode of an area S is expressed as:

$$C_{b0} = \left(\frac{e\varepsilon\varepsilon_0 S^2 N_{Deff}}{2U_{bi}} \right)^{1/2}, \tag{3.1}$$

where, ε_0 is the vacuum permittivity, ε – material dielectric permittivity, e – elementary charge, N_{Deff} – the effective doping density, U_{bi} – built-in potential barrier, $w_0=(2\varepsilon\varepsilon_0 U_{bi}/eN_D)^{1/2}$ – the width of depletion for the non-biased junction. The barrier capacitance for a junction diode can be written as:

$$C_b = C_{b0}(1+U/U_{bi})^{-1/2}. \tag{3.2}$$

Fig. 3.3 illustrates the simulated BELIV transients.

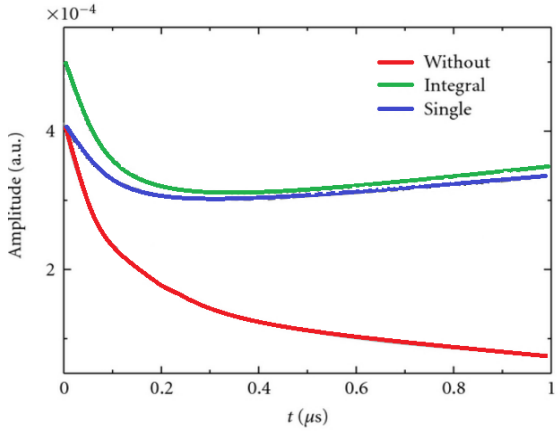

Fig. 3.3 Comparison of charge extraction BELIV current transients simulated for single-type traps (blue line) and for simultaneously acting several-type generation centres (green line) with that simulated without contribution of thermal emission from traps (red line) [95].

The current transient $i_C(t)$ in the external circuit is then determined by the time-dependent changes of charge $q = C_bU$ within junction:

$$i_C(t) = \frac{dq}{dt} = \frac{\partial U}{\partial t}(C_b + U\frac{\partial C_b}{\partial U}) = AC_{b0}\frac{1+\frac{At}{2U_{bi}}}{(1+\frac{At}{U_{bi}})^{3/2}}. \qquad (3.3)$$

The proton-induced luminescence (PI-L) spectra and the BELIV transients have simultaneously been recorded during 1.6 MeV proton irradiation emitted by a linear particle accelerator Tandetron 4110A. The coaxial and fibre-optics probes were used for simultaneous recording of the electrical (BELIV) and optical (PI-L) signals [96]. The BELIV circuitry contains an adjusted output of a generator of the linearly increasing voltage, a sensor under test and a load resistor (R_L), connected in series. The BELIV signal were recorded by a DSO6102A oscilloscope using a 50 Ω load input. The PI-L spectra were recorded using an Avantes AvaSpec 2048 TEC spectrometer.

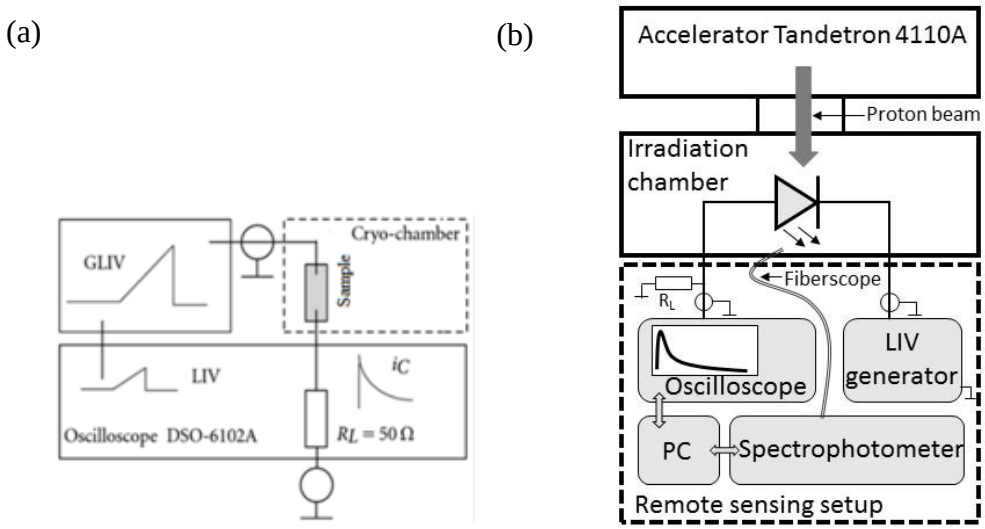

Fig. 3.4 Sketch of the experimental setup for temperature-dependent BELIV measurements (a) and *in situ* control of PI-L and BELIV characteristics during irradiation by protons (b) [A7].

3.2.3. The technique of the microwave probed photoconductivity transients

Carrier lifetime is the most sensitive parameter to characterize defects in material, i.e. the long carrier lifetime is an indication of the low impurity/defect concentration [97]. By investigating the carrier decay characteristics, the MW-PC transients under excess carrier excitation are recorded. There, MW signal variations in time (t) is proportional to the free carrier concentration $n(t)$. Carrier lifetime, ascribed to the non-radiative carrier recombination, is evaluated from the slope of the MW signal relaxation rate using a definition of the

instantaneous lifetime $\tau_{inst}=n(t)/(-dn(t)/dt)$ [97]. For simple situations, when the single-type deep centres are acting, the transients of the carrier concentration decay are single-exponential. In the cases of either competition of several centres or carrier trapping effects, the carrier decay transients have a multi-exponential decay slope. The parameters of the excess carrier (n_{ex}) recombination and trapping centres have been obtained by analysing carrier decay transients recorded by MW-PC technique at relatively low excitation level (with $n_{ex} \leq 10^{15}$ cm^{-3}) [97]. MW-PC transients were recorded using pulses of 400 ps duration at 354 nm excitation wavelength. The MW-PC response signals were detected by using a coaxial needle-tip MW (of ~ 21 GHz) probe. The signal recording scheme contains a balanced microwave bridge circuit. A digital 1 GHz oscilloscope of Tektronix TDS-5104 model was employed to register the photo-response signals. The MW-PC transients by using tuneable wavelength excitation pulses of 4 ns and 40 fs duration have been recorded for the PPIS measurements.

3.3. Spectroscopic methods

All the techniques for the measurement of the parameters of defect levels have specific limitations. Therefore, combining of several spectral methods is the most successful methodology for characterization of the deep levels.

Deep level transient spectroscopy (DLTS) is a powerful and widely employed method used for observing the electrically active defects in semiconductors. The values of thermal activation energy E, of capture cross section σ, and of traps concentration N_T are mainly evaluated by DLTS [22]. The DLTS technique requires forming of either the Schottky or the p-n junction. The rather large trap concentration relative to that of dopants in materials is a well-known limitation for using a routine, capacitance based DLTS (C-DLTS). For the C-DLTS method, a signal is proportional to the ratio of trap concentration (N_T) to that of the effective doping (N_{Def}). In most cases, the characterized samples contain more than one trap level. Hence, the measured transients are not the single-time constant, i.e. exponential, functions. Usually the superposition of different decay processes in the form of $C(t) = \sum_{i=1}^{n} C_i(0) e^{e_i t}$ appears, where n

is the number of different deep levels and e_i is the emission rate. The e_i parameter contains the most important physical characteristics of the defect. It is well known, care should be taken in using Arrhenius emission rate plots, for extracting of the capture cross section values, particularly for deep, non-hydrogenic levels and for levels, where the emission rate is affected by electric fields (Poole-Frenkel effect).

The temperature dependent carrier-trapping lifetime (TDTL) spectroscopy, based on the measurements of the MW-PC transients [97], was employed for the identification of the radiation defects. The contactless TDTL technique allows to identify the energy levels of the defects and their concentrations. This technique is preferential when the trap density approaches or exceeds the dopant concentration and when it is necessary to avoid modification of a detector structure due to annealing processes at elevated temperatures.

Optical spectroscopy methods, such as PL and photoionization spectroscopy, are widely used techniques for characterization of a variety of material parameters, e.g. in estimation of the inherent energy levels of defects and their concentrations, of the strength of the electron-phonon coupling. The mentioned techniques are contactless. The fundamental limitation of the PL method is a necessary of radiative recombination events. Materials with a weak radiation efficiency, e.g. low-quality indirect bandgap semiconductors, are difficult to investigate by PL methods. Also, a sensitivity of identification of the impurity and defect states depends on their PL activity. Nevertheless, PL is a very sensitive probe of radiative transitions [98]. Values of the photoionization energy of the prevailing defects have been determined by the PPIS technique. Due to the large leakage current, and the difficulties in the fabrication of appropriate contacts, extraction of values of the photoionization energy is complicated when using the standard contact deep-level optical spectroscopy (DLOS) and photo-induced current transient spectroscopy (PICTS) techniques, despite the enhanced sensitivity in signal recording of these methods. To overcome these difficulties, the PPIS method has been implemented in contactless mode using excitation by a tuneable wavelength laser and

measurements of the photo-response, recorded by the microwave probed photoconductivity transient (MW-PC) technique.

The electron spin resonance (ESR) technique enables identification of the spin active defects and their complexes. The impurities with an ionic character lead to the strong infrared (IR) absorption, while the bonds with a covalent character lead to strong Raman absorption. Thus FTIR spectral methods are used for detecting of the rotational and vibrational modes of molecules, whereas Raman active modes depends on the changes in polarizability of a molecule. FTIR active modes depends on variation of the dipole moment of a point defect [99]. Combining of the Raman and FTIR spectroscopy provides a comprehensive tool for the identification of structural defects and impurities. Usually, defects and impurities those cannot be detected with one of the mentioned method can be easily revealed by the other one.

3.3.1. Deep level transient spectroscopy

The DLTS technique is used for the evaluation of parameters of the thermal activation energy, of capture cross-sections for electrons and holes, and for estimation of the concentration of carrier traps as well as the trap distribution within depth of Schottky and pin diode structures. The capacitance deep level transient spectroscopy (C-DLTS) and current-DLTS (I-DLTS) regimes can be implemented using either electrical or optical carrier injection. In contrast to PL, the DLTS is capable of detecting thermal emission parameters of trap levels.

The capacitance mode DLTS is based on measuring the temperature-dependent capacitance transients [22]. An occupancy of the state is determined by the emission and capture processes (Fig. 3.5).

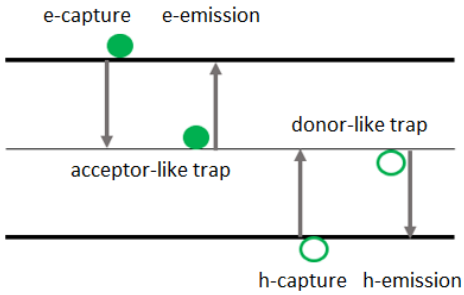

Fig. 3.5 Electron and hole capture and emission processes that involve a localized state.

The capture rates for an electron c_n and hole c_p, are defined as:

$$c_n = \frac{(\Delta n_t/\Delta t)}{(N_t - n_t)} = \sigma_n \langle v_n \rangle n, \qquad c_p = \frac{(\Delta(N_t - n_t)/\Delta t)}{(n_t)} = \sigma_p \langle v_p \rangle p\,, \quad (3.4)$$

where N_t - n_t is the total concentration of deep traps, n_t is the density of the trap occupied by electrons, σ_n, σ_p are the electron and hole capture cross sections, $<v_n>$, $<v_p>$ are the thermal velocity of electrons and holes, n, p is the concentration of free electrons and holes, respectively. The net rate of change of electron occupancy in the material can be expressed as follows:

$$\frac{dn_t}{dt} = (c_n + e_p)(N_t - n_t) - (e_n + c_p)n_t\,, \quad (3.5)$$

where e_n, e_p are the emission rates for an electron and hole, respectively. After a filling of trap levels by a voltage pulse or by light injection, the traps start to emit carriers through the thermal emission process ($e_n > c_n$). This emission leads to a change of the barrier capacitance transients:

$$C(t) = C\left\{1 - \frac{n_t(t)}{N_d + N_t}\right\}^{\frac{1}{2}}, \quad (3.6)$$

where N_d is the effective donor concentration, C is the steady-state capacitance, which is expressed as:

$$C(\infty) = A\left\{\frac{\varepsilon\varepsilon_0(N_d + N_t)}{2}\right\}^{\frac{1}{2}} V^{-\frac{1}{2}}, \quad (3.7)$$

where A is an area, ε, ε_0 are the permittivities of material and vacuum, respectively, V is the bias voltage. When $N_t, n_t << N_d$, the time varied barrier capacitance change, determined by the majority carrier emission, can be expressed as:

$$\frac{\Delta C(t)}{C} = \begin{cases} -\frac{1}{2}\frac{N_T}{N_{Def}} e^{-e_n t}, & e_n >> e_p \\ 0, & e_n << e_p \end{cases}. \quad (3.8)$$

C-DLTS method is acceptable when the N_T is less than 10% of the shallow dopant (N_{Def}) concentration. The current-DLTS (I-DLTS) method is preferable for spectroscopy of the defects-rich irradiated samples [100,101]. The I-DLTS signal does not depend directly on N_{Def} value, and there is no limitation for the ratio of the N_T/N_{Def}. Thus, I-DLTS method can be applied to study of both high

resistivity and very defective materials. The total current density is then expressed by the relation:

$$J(t) = -\frac{1}{2} q x_d N_T \frac{e_n}{e_n + e_p} \left[2e_p + \left(e_n - e_p \right) e^{-(e_n + e_p)t} \right] = J_L + \delta J \,, \qquad (3.9)$$

where x_d denotes the depletion width, q is the elementary charge. The first term in Eq. 3.9 is the leakage current density J_L, which is independent of time. The second term in Eq. 3.9 is the transient signal of the current density, which is expressed as

$$\delta J(t) = -\frac{1}{2} q x_d N_T \frac{e_n}{e_n + e_p} \left(e_n - e_p \right) e^{-(e_n + e_p)t} = \begin{cases} -\frac{1}{2} q x_d N_T e_n e^{-e_n t} (e_n >> e_p) \\ \frac{1}{2} q x_d N_T e_n e^{-e_p t} \cong 0, (e_n << e_p) \end{cases} . \qquad (3.10)$$

The amplitude of the transient current δJ depends on the depletion width x_d, on the concentration N_T of deep traps and on the emission rate e_n. The current transient in fully-depleted junction, when re-trapping of the emitted carriers can be neglected, is roughly approximated by the expression

$$I(t) \propto F \mu e_n \exp(-e_n t) \,. \qquad (3.11)$$

Here, F is the electric field module, μ is the mobility of carriers, e_n is the carrier emission rate. In case of the discrete energy states E_{tr}, the emission rate e_n, at fixed temperature T, is related to the interaction cross-section σ_n as:

$$e_n(T) \propto \sigma_n T^2 \exp\left(\frac{-E_{tr}}{kT} \right) . \qquad (3.12)$$

The principle of operation of the typical DLTS spectrometer is illustrated in Fig. 3.6. The deep levels are filled with free carriers by electrical pulse (a). After the voltage pulse ends, thermal emission of carriers from the traps produces the capacitance transient while the temperature is slowly varied at a constant rate (b). The capacitance transient is analysed by signal processing and Arrhenius plots for all the investigated defects levels are fitted on the experimental points (c). The peak positions in temperature within the pre-established rate window for two deep levels are illustrated in Fig. 3.6 (d). There it is worth to note that the C-DLTS peak height is proportional to the deep level

concentration. The digital DLTS systems commonly contain the correlation function algorithm for analysis of the transients.

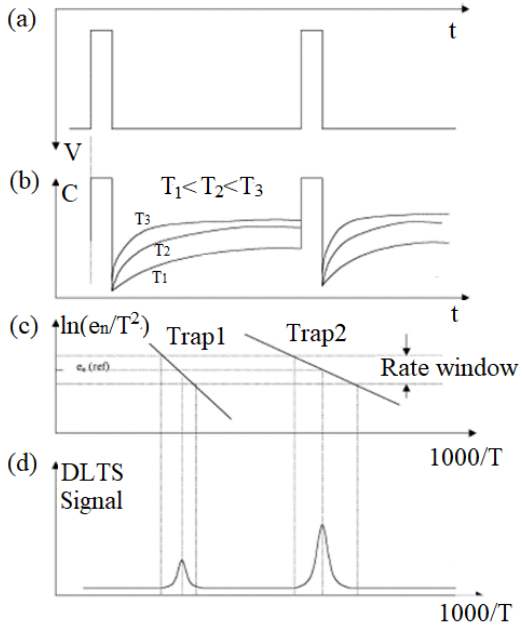

Fig. 3.6 a - Voltage pulses applied to the device under study to produce transients of capacitance, b - transients occurring at different temperatures, c - Arrhenius plots illustrating the meaning of the rate window, which is the user pre-defined to establish a known emission rate at the DLTS signal peaks, d - DLTS signal showing some peaks occurring within the rate window [102].

The DLTS measurement setup employed in this study for the defect spectroscopy is based on a commercially available HERA-DLTS system FT 1030 [103] (Fig. 3.7). In the HERA-DLTS, the standard DLTS i.e. the double boxcar correlator with gates set at t_1 and t_2, is installed. The capacitance values are there measured at the two time instants t_1 and t_2. The difference $C(t_1) - C(t_2) = \Delta C$ is then calculated. In the digital DLTS mode, the complete capacitance transient is recorded. Laplace-DLTS (L-DLTS) can be also realised. Then, the capacitance transient is measured with great precision at fixed temperature, when implementing L-DLTS mode. The latter transients are analysed using Fast-Fourier-Transform-based algorithms to convert analysis of the defect relaxation process from the time domain into a spectrum of the frequency domain. Moreover, in L-DLTS mode, the higher signal-noise ratio and an a-priori knowledge of the temperature interval are needed. The capacitance recording is based on the isothermal measurements mode. Therefore, the analysis of L-DLTS spectra is difficult on the defects-rich

materials. Nevertheless, owing to the combination of the special analysis instruments, the HERA-DLTS system is flexible and reliable for the separation of the overlapping peaks.

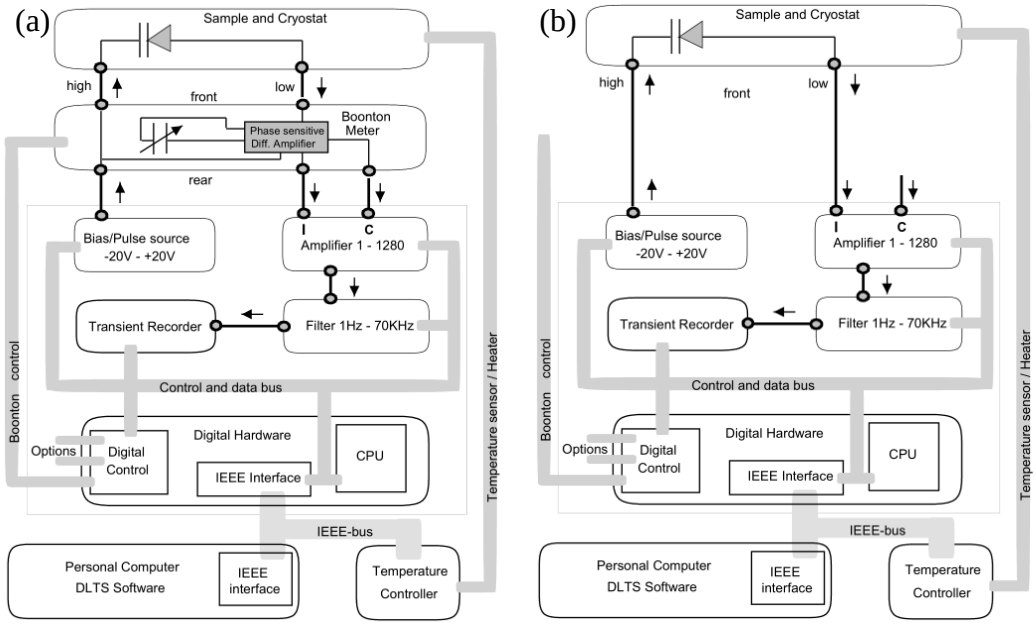

Fig. 3.7 The setup for Capacitance-DLTS (a) and Current-DLTS (b) measurements.

3.3.2. Technique based on temperature dependent trapping lifetime

Contactless TDTL spectroscopy, based on research of the temperature dependent trapping lifetime (TDTL) [97,104], was employed for defect identification. The measurements were carried out using pulsed (400 ps) excitation at 1062 nm wavelength and a coaxial needle-tip microwave (22 GHz) probe within a near-field probing regime. Measurements were performed by a proprietary device VUTEG-6, fabricated at Vilnius University. The TDTL technique is preferential when radiation trap density approaches or exceeds the dopant concentration. The trapping and de-trapping is related to the thermal release lifetimes, which is expressed as [97]

$$\tau_{inst,tr} \approx \tau_R \times [1+(N_{tr}/N_{C,V}) \times \exp(E_{tr}/kT)], \quad (3.13)$$

where τ_R is the carrier recombination lifetime, N_{tr} is is the concentration of shallow trapping centres, $N_{C,V}$ is the density of states in conduction (C) and valence (V) bands, respectively, E_{tr} is the trap activation energy (relative to thermal emission). Due to a difference between the carrier recombination (τ_R)

and thermal release lifetimes ($\tau_{inst,tr} \approx \tau_R \times [1+(N_{tr}/N_{C,V}) \times \exp(E_{tr}/kT)]$), carriers captured to the trapping centres delay the recombination process. The two-componential transient approach enables description of the temperature dependent trapping effect at large concentrations of the trapping centres N_{tr}. Then, the instantaneous decay lifetime is expressed through the τ_R and the trapping coefficient K_{tr} [97], which includes parameters of N_{tr}, the effective density of band states for trapped carriers $N_{CM}=N_{C,V,e,h,Ntr}= N_{C,V} \times exp(-E_{tr}/kT)$ and the scan temperature (T). These parameters are linked as:

$$\tau_{inst,tr} = \tau_R K_{tr}(\Delta n(t,T)); \qquad (A)$$

$$K_{tr}(t,T,T_{an}) = 1 + \frac{N_{tr}(T_{an}) N_{C,V,e,h,Ntr}(T,E_{tr})}{(N_{C,V,e,h,Ntr}(T,E_{tr}) + \Delta n(t,T))^2}; \qquad (B)$$

$$K_{tr}(t,T,T_{an})|_{K_{tr}>>1} = \begin{cases} \dfrac{N_{tr}(T_{an}) N_{C,Ntr}(T,E_{tr})}{(n(t,T))^2}\Big|_{N_{C,Ntr}(T,E_{tr}) < \Delta n(t,T)} \propto T^{3/2} \exp(-E_{tr}/kT), T < T_{peak} \\ \dfrac{N_{tr}(T_{an})}{N_{C,Ntr}(T,E_{tr})}\Big|_{N_{C,Ntr}(T,E_{tr}) > \Delta n(t,T)} \propto T^{-3/2} \exp(E_{tr}/kT), \quad T > T_{peak}, \end{cases} \qquad (C)$$

. (3.14)

Here, T is the scan temperature, while T_{an} is the anneal temperature which may cause changes of trap density due to defect transformations. The simulated dependencies of carrier-trapping lifetime (using Eq. 3.14) can be applied for the spectroscopy of trapping levels, as illustrated in Fig. 3.8. A peak temperature (T_{peak}), for which the largest trapping coefficient (ascribed to a single type trapping centre) is obtained, can be found using condition of extremal trapping coefficient

$$\frac{\partial K_{tr}(T)}{\partial T} = 0 \quad . \qquad (3.15)$$

For fixed excess carrier density Δn_c, the peak temperature (T_{peak}) can be estimated by solving the transcendental equation:

$$T_{peak} = A^{2/3} \exp\left(\frac{2}{3}\frac{E_{tr}}{kT_{peak}}\right) \times 300K, \quad \Delta n_C = const \quad . \qquad (3.16)$$

Here, $A=\Delta n_C/N_{C,V,T=300K}$, and $N_{C,V,T=300K}$ denotes the expression for the density of states $N_{C,V}$ at T=300 K temperature. The variation of absorption coefficient with temperature ($\alpha(T)=\alpha_{300} \times (T/300(K))^{4.25}$) needs to be taken into account. Then, the concentration of the excess carriers becomes a function of temperature $\Delta n(T)= \alpha(T) \times F$, where α_{300}=10 cm^{-1} [105] is the absorption coefficient at

T=300 K (for light wavelength 1064 nm in Si), and F is the surface density of incident photons. The peak temperature is then obtained as a real root of the more intricate transcendental equation (relative to Eq. 3.15) obtained using a condition of the extremal trapping coefficient.

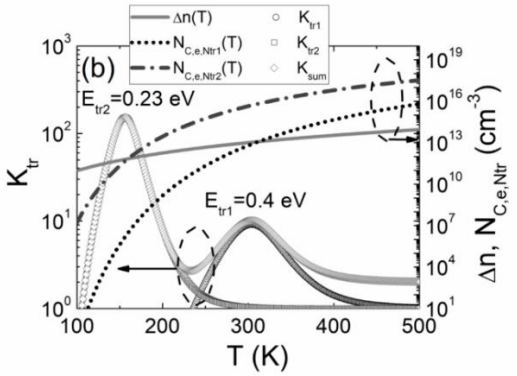

Fig. 3.8 Simulated trapping coefficient as a function of scan temperature for the trapping levels with activation energies of 0.23 eV and 0.4 eV and the same trap density N_{tr} (2×10^{14} cm^{-3}) in Si. Temperature dependent variations of the $\Delta n_0(T)$ and $N_{C,e,Ntr1,2}(T)$ are also depicted. [106].

A spectrum of TDTL represents the instantaneous trapping lifetime values as a function of scan temperature T (or $1/kT$). Activation energy E_{tr} and trap concentration N_{tr} is calculated with assumption of fixed capture cross section of a single-species defect (Fig. 3.8). There pulsed excitation intensity is kept constant, therefore, density of excess carriers is simulated to be temperature dependent $\Delta n_0(T)$, due to absorption coefficient dependence on temperature (Fig. 3.8). The effective density of band states $N_{C,V,Ntr}(T,E_{tr})$ should also be incorporated within simulations, while the latter parameter varies only with scan temperature T for a definite E_{tr} value and free carrier band, as shown in Fig. 3.8. In many cases, particularly for irradiated materials, the TDTL spectral peaks, ascribed to different trapping centres, overlap (Fig. 3.8). This leads to difficult interpretation of experimentally obtained spectra.

A limitation of the TDTL technique appears due to the high concentration of recombination centres. The trapping decay component might be hidden when concentrations and capture cross-sections of the recombination centres significantly exceed concentrations and capture cross-sections of the trapping centres.

3.3.3. Photoluminescence spectroscopy

Photoluminescence (PL) spectroscopy is widely used for the determination of band gap, the detection of defects levels, and the investigation of the recombination mechanisms. PL is a quantum mechanical process in which a photon is absorbed within material by transferring its energy to an electron in the ground state and exciting it to an excited state within fs timescale [107]. In semiconductors, where impurities are intentionally incorporated as donors or acceptors, extrinsic PL occurs. There, transitions electron trapped on donors (i.e. on a neutral donor state D^0) and a hole state of the top of the valance band (b in Fig. 3.9) and between the electron states at the bottom of the conduction band and a hole state of the neutral acceptor state A^0 (Fig. 3.9c) occur. Besides the PL from free excitons (FE), various other excitonic recombination processes also occur. These are the radiative recombination of bound excitons (BE), excitonic polarons, self-trapped excitons, and excitonic molecules, which can exist at low temperatures. Bound excitons are formed by the capture of a free exciton by a neutral impurity state (neutral acceptor A^0 or donor D^0), ionized impurity state (ionized donor D^+ or acceptor A^-), or by a defect. Fig. 3.9e illustrates a bound exciton captured by D^0 or D+. Donor to acceptor pair (DAP) recombination (Fig. 3.9f) occurs in material, when both types of impurities are present. Fig. 3.9g shows the recombination process for the deep-level PL, which involves a Shockley-Read-Hall type transition, also called trap-assisted recombination, with a single deep level within the bandgap [107].

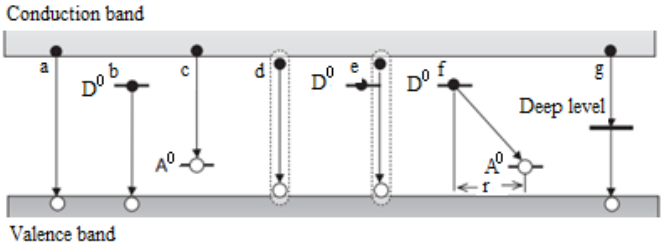

Fig. 3.9 Scheme of radiative recombination processes in semiconductors. a - Band-to-band recombination, b - neutral donor (D^0) to VB transition, c - CB to neutral acceptor (A^0) transition, d - radiative recombination of FE, e - radiative recombination of BE, which is bound to D^0 (recombination of BE bound to ionized donor D^+ is also possible), f - DAP recombination with separation *r*, g - deep-level defect luminescence [107].

The methods of PL spectroscopy are classified into three categories, namely, steady-state PL (SS-PL), time-resolved PL (TR-PL), and time-integrated PL (TI-PL) spectroscopy. The emission from the sample after excitation is dispersed by the monochromator in order to obtain the PL spectrum by performing SS-PL measurements. TR-PL and TI-PL measurements can be performed by using streak camera detection system. A streak camera is a unique method that can provide simultaneous measurements of both spectral and transient characteristics with a high resolution. A streak tube, which can resolve photons spatially and temporally by converting them to photoelectrons, is essential in this device [107].

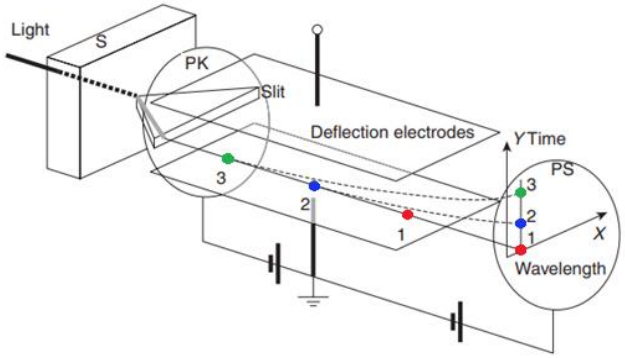

Fig. 3.10 Schematic view of streak tube with a spectrograph (S) to disperse the incident light pulse along a horizontal slit. [107].

The basic structure of steak tube (Fig. 3.10) is composed of a horizontal slit, a photocathode (PK), a pair of vertically deflecting electrodes, and a phosphor screen (PS). High-speed microchannel plate image intensifier is placed in front of the screen (PS), and a CCD image sensor behind PS. When an incident light is dispersed by a spectrograph (S), its spectral image is projected on to the photocathode (PK) along a horizontal axis of slit, and photoelectrons corresponding to the slit image, are emitted. Light pulses are diffracted on a spot of K, which emits three photoelectrons 1, 2, and 3. These photoelectrons are accelerated by the electric field between the photocathode and the screen going through the deflecting electrodes. If the deflecting electrodes are voltage ramped after a trigger synchronizing with an incident pulse of light, the photoelectron that arrives at PS later, like the electron 3, is more deflected vertically. Temporal profile from a streak image of the incident light is presented on the vertical time

axis on PS, and its spectrum on the horizontal wavelength axis appears. Brightness of the spot on PS corresponds to the light intensity, that is, to the incident photon density. 3D image of the incident photon density (z-direction) axis in time (y-direction) and wavelength (x-direction) axes is obtained by CCD camera [107].

The SS-PL measurements at low excitation level (with excess carrier concentrations $n_{ex} \leq 10^{15}$ cm^{-3}) were performed by using an arrangement composed of the 325 nm He-Cd laser for SS-PL excitation, a Jobin-Yvon monochromator and an UV-enhanced Hamamatsu photomultiplier.

TR-PL measurements at high excitation level (with excess carrier concentrations $n_{ex} \geq 10^{18}$ cm^{-3}) were performed using the PHAROS laser pulses at 315 nm wavelength (generated by optical parametric oscillator ORPHEUS). A Hamamatsu C10627 streak-camera along with an Acton 2300 spectrometer were used for the measurements of PL spectra and transients.

3.3.4. Pulsed photo-ionization spectroscopy technique

The PPIS is beneficial spectroscopic technique relative to photocurrent spectroscopy. The latter technique is based on the direct (dc) photo-current measurements. The dark leakage current does not play a role in PPIS measurements, therefore the recorded signal is clearly resolved and synchronized with a photo-excitation pulse [108]. The PPIS technique allows simultaneous control of the changes of definite photo-ionization spectral steps and the recombination lifetimes of the photo-excited carriers. Furthermore, using contact-less MW-PC technique for the photo-response measuring, contact related effects are eliminated.

Photo-ionization or photo-neutralization of deep levels is characterized by optical cross-section, and spectroscopy of these cross-sections provides the direct information concerning matrix elements coupling wave functions of deep levels to those wave functions of band free carriers. Assumption of a δ-type potential of deep centre leads to the Lucovsky's model [109]. This model has a single parameter E_d (photo-activation energy) within a fitting procedure of

spectra analysis. The cross-section $\sigma_{p\text{-}e}$ in Lucovsky's model [109], is described by expression

$$\sigma_{p-e}(h\upsilon) = \frac{C_{p-e}E_d^{1/2}(h\upsilon - E_d)^{3/2}}{(h\upsilon)^3}, \quad (3.17)$$

where $C_{p\text{-}e}$ is a multiplicative factor. Changes of absorption coefficient $\alpha(h\nu)$ for $h\nu$ energy photons due to photo-ionization of n_{d0} trapped carriers can then be described by $\alpha(h\nu)=\sigma_{p\text{-}e}(h\nu)n_{d0}$. Illumination by a light pulse of surface density $F(h\nu)$ of the incident photons leads to the density of photo-emitted carriers $n^*_d=\sigma_{p\text{-}e}(h\nu)n_{d0}F(h\nu)$ registered by MW probe. Then, the density of N_d traps can be evaluated from an absorption coefficient $\alpha(h\nu)$ spectrum. The filling factor n_d/N_d can be controlled by combined measurements of MW-PC signal peak value or $\alpha(h\nu)$ as a function of $F|_{h\nu}$, and the saturation of these characteristics indicates a complete photo-ionization of N_d traps.

The electron-phonon coupling can play an important role in formation of PPIS steps. Different models, which include the electron-phonon coupling, have been developed [103–107] to fit the spectral peaks. The phonon-assisted changes of the cross-section $\sigma(h\nu)$ for a definite defect can be approximated by the Kopylov-Pikhtin [114] approach

$$\sigma(h\nu) \propto \int_0^\infty \frac{e^{-(E+E_d-h\nu)^2/\Gamma^2}\sqrt{E}dE}{h\nu(E+E_d)^2}, \quad (3.18)$$

where the electron-phonon coupling is determined by the broadening parameter Γ. The broadening parameter is related to the Huang-Rhys factor $S = d_{FC}/h\nu_0$, which is a ratio between the Franck-Condon shift (d_{FC}) and the energy of the vibrational mode ($h\nu_0$). The Huang-Rhys factor quantifies the number of phonons emitted during an optical transition [115]. The Γ at absolute zero temperature can be determined by the equation [116]:

$$\Gamma_0 = \frac{\nu_g}{\nu_e}\sqrt{2d_{FC}\nu_g}. \quad (3.19)$$

Here, ν_g and ν_e are the frequencies of the ground and the excited state, respectively. Using $\nu_e = \nu_g = \nu_0$, the Eq. 3.19 becomes:

$$\Gamma_0 = \sqrt{2d_{FC}\nu_0} \approx 1.414\nu_0 S^{1/2}. \quad (3.20)$$

The temperature-dependent broadening is then expressed as:

$$\Gamma = \Gamma_0 \sqrt{2coth(h\nu_0/k_B T)}. \quad (3.21)$$

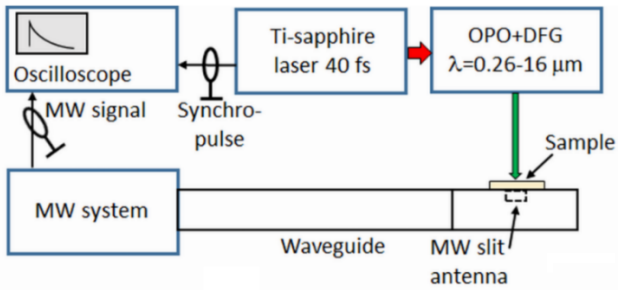

Fig. 3.11 Setup of instrumentation for the PPIS measurements.

The PPIS measurements were performed using excitation by fs and ns lasers equipped with optical parametric oscillators (OPO). The MW-PC and spectrum resolved PL transients were recorded simultaneously by using the system illustrated in Fig. 3.11. The femtosecond and nanosecond pulsed excitation were combined in order to clarify the role of electron-phonon coupling in photo-ionization processes.

An OPO instrument Ekspla NT342B with pulse duration of 4 ns and wavelength tuning range from 210 to 2300 nm, and a Ti:sapphire laser based OPO system with pulse duration of ~40 fs and wavelength tuning range of 350–2500 nm were employed. The sample was placed on a slit-antenna of the 21–22 GHz MW system and excited by OPO laser beam, starting from long wavelength wing to avoid simultaneous filling of several traps.

3.3.5. Electron spin resonance spectroscopy technique

Electron spin resonance (ESR) [117], also called electron paramagnetic resonance (EPR), spectroscopy technique is similar to other techniques that depends on the absorption of electromagnetic radiation. ESR spectroscopy is based on quantifying the energy differences between the magnetically induced splitting of electronic spin states. ESR is a common method for determining the *g*-value, the hyperfine coupling constant (hfcc) and the concentration of spin active defects.

The electron possesses on orbital angular momentum as it moves around the nucleus. The electron also possesses spin angular momentum $\vec{S}$. The magnitude of $\vec{S}$ is expressed as [118,119]:

$$\vec{S} = (h/2\pi)[S(S+1)]^{1/2}, \quad (3.22)$$

where h is Planck's constant and S is the spin quantum number. By restricting the dimension to the z direction, the component of the spin angular momentum has two values:

$$\vec{S}_z = M_S h/2\pi. \quad (3.23)$$

The term M_S can have only two possible values for a single unpaired electron, that are referred to as α ($M_S = 1/2$) or β ($M_S = -1/2$).

Due to a spinning electron behaves like a bar magnet, the most important physical aspect of the electron spin is the associated magnetic moment μ_e, which is directly proportional to the spin angular momentum. The μ_e is expressed as:

$$\mu_e = -g_e \mu_B \vec{S}, \quad (3.24)$$

where μ_B is the Bohr magneton and g_e is the free electron g-factor. An expression that represents multiplication of these factors ($g_e\mu_B$) is called the magnetogyric ratio. Bohr magneton is the atomic unit of magnetic moment, defined as:

$$\mu_B = e\hbar/2m_e, \quad (3.25)$$

where e is the electron charge, $\hbar = h/2\pi$ and m_e is the electron mass. ESR spectroscopy is based on magnetic moment interactions with the applied magnetic field. The energy E of the interaction between the magnetic moment (μ) and the field (B) is described as:

$$E = -\mu \cdot B. \quad (3.26)$$

If the field is defined along the z direction, the energy E can be determined by taking account of the term M_S:

$$E = g_e \mu_B B M_s, \quad (3.27)$$

M_S can have only values ±1/2, and these states are degenerate in the absence of a magnetic field. As magnetic field increases, this degeneracy is lifted linearly (Fig. 3.12) [119], where the absorption and first-derivative spectra are also shown. The energy separation of the two levels matches to a quantum of radiation through the Bohr frequency condition:

$$\Delta E = h\nu = g\mu_B B. \quad (3.28)$$

The splitting between the two states is referred to as the electron Zeeman interaction. The induced transitions from the lower energy level to the higher energy level by applying magnetic field is the basis of ESR spectroscopy.

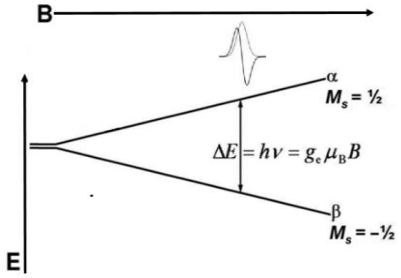

Fig. 3.12 Energy levels for an electron with spin $S = \pm 1/2$ in an applied magnetic field $\vec{B}$ [119].

The nuclei of the atoms in a molecule or any atomic complex usually have their own magnetic moments. Therefore, the energy of an unpaired electron also depends on the interaction between the unpaired electron and the nuclei produced local magnetic field. Due to this interaction, the additional splitting of ESR transitions occurs between the electron's magnetic moment and the magnetic moment of neighbouring nuclei. In the high field approximation where the electron Zeeman interaction dominates over all other interactions, the energy level for the two-spin system (S = 1/2, I = 1/2) can be expressed as:

$$E(M_s, M_l) = g\mu_B B M_s - g_N \mu_N B M_I + ahM_s M_I, \qquad (3.29)$$

where M_s and M_I are the nuclear spin quantum number, g_n is the nuclear g-factor and a is the isotropic hyperfine coupling factor. Energy level diagram for a two spin system (S = 1/2 and I = 1/2) in high magnetic field is shown in Fig. 3.13, where the electron Zeeman, nuclear Zeeman and hyperfine splittings with the isotropic hyperfine coupling $a > 0$ (a) and for an unpaired electron (S = 1/2) interacting with two inequivalent I = 1/2 spin nuclei such that $a_1 > a_2$ (b) are illustrated. The number of lines from the hyperfine interaction can be determined by the relation: $2N_I + 1$. Here, N is the number of equivalent nuclei. The number of the ESR spectral lines from the interaction of an unpaired electron with an equivalent nuclei of spin I can be determined as $2nI + 1$. For the most common hydrogen nuclei (I = 1/2), the relative intensities of the ESR absorptions are given by the binomial expansion of $(1+x)^n$. The successive sets of coefficients for increasing n are given by the Pascal's triangle [119].

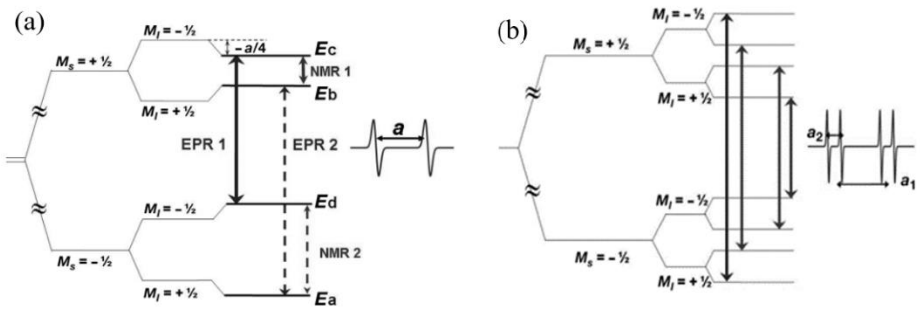

Fig. 3.13 Energy level diagram for a two spin system in high magnetic field illustrating the electron Zeeman and nuclear Zeeman and hyperfine splittings, with the isotropic hyperfine coupling $a > 0$ (a) and for an unpaired electron ($S = 1/2$) interacting with two inequivalent $I = 1/2$ spin nuclei such that $a_1 > a_2$ (b) [119].

For the case illustrated in Fig. 3.13a, due the ESR selection rules, when $\Delta M_I = 0$ and $\Delta M_S = \pm 1$, only two possible resonance transitions can occur, namely ΔE_{cd} (labelled EPR 1) and ΔE_{ab} (labelled EPR 2):

$$\Delta E_{cd} = E_c - E_d = g\mu_B B + \frac{1}{2}ah,$$
$$\Delta E_{ab} = E_b - E_a = g\mu_B B + \frac{1}{2}ah. \qquad (3.30)$$

These two transitions give rise to two absorption peaks at different magnetic field positions (Fig. 3.13a). The nuclear magnetic resonance transitions, for which it is possible to extract the same value of a, are labelled as NMR1 and NMR 2.

The resonance experiment can be conducted in two ways: either the magnetic field is kept constant and the applied frequency varied, or the applied frequency is held constant and the magnetic field is varied. In ESR spectroscopy the magnetic field variation is usually used, since it is far easier to vary the magnetic field over a wide range than to change frequency [119].

ESR measurements were performed by using the X-band Bruker Elexsys E580 spectrometer operating in the 8−10 GHz frequency range. Temperature was varied in the range of 90−300 K using a continuous N gas flow Bruker cryostat. In order to find the optimal MW power for the sample under investigation and to avoid signal distortions, the microwave (MW) power was varied in the range of 0.15−150 mW. Ranges of saturation of the ESR signal were determined by examination of the ESR signal changes dependent on the applied MW power.

3.3.6. FTIR and Raman spectroscopy techniques

The Raman and FTIR are vibrational spectroscopy methods, based on detection of rotational and vibrational modes of molecules. The incident light interacts with the molecular vibrations or phonons within the material. This creates a change in frequency due to the absorbed light is re-emitted by the material. Raman and FTIR spectroscopy differ on some fundamental aspects: Raman spectroscopy depends on a change in polarizability of a molecule, while FTIR spectroscopy depends on a change in the dipole moment. Raman spectroscopy measures relative frequencies at which a sample scatters radiation and an inelastic scattering phenomenon probes molecular vibrations to provide a molecular fingerprint of materials. FTIR spectroscopy measures absolute frequencies at which a sample absorbs, reflects or transmits radiation. In Raman spectra, the observed values are relative to the excitation source and are considered as Raman shift values. In infrared absorption or transmission spectra, wavenumbers (cm^{-1}) are related to the absolute energy values.

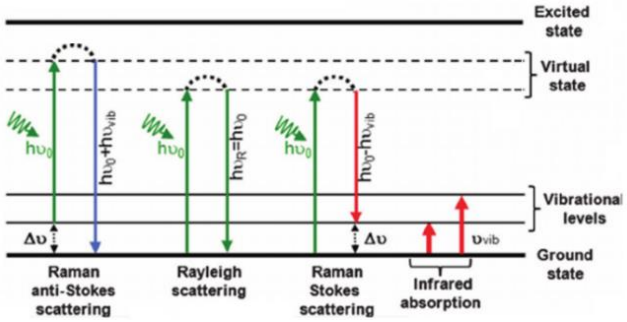

Fig. 3.14 Energy-level diagram of the states involved in Raman and IR absorption spectra [120].

Energy-level diagram of transitions between vibrational energy levels of molecules is shown in Fig. 3.14. If the photon is scattered elastically, the absorbed photon has the same wavelength with the emitted one (Rayleigh scattering). If the photon is scattered inelastically, the energy of a photon can decrease or increase by amount of the energy related to the vibrational energy spacing in the molecule. This amount corresponds to the wavelength of the Stokes (wavelength is greater than that of the incident light) and anti-Stokes lines (wavelength is lower than that of the incident light) which are equally displaced from the Rayleigh line in the Raman spectrum. FTIR spectroscopy measures the

vibrational energies of molecules. The absorption, transmission or reflectance of light in the IR region gives a spectrum that corresponds to the vibrational modes of the chemical bonds in a molecule, and this is specific to each molecular structure. In the case of Raman scattering, the scattering efficiency is higher in covalent crystals than that in ionic crystals, because the valence electrons are less localized and the larger fluctuations of the polarizability can be induced by lattice vibration [121]. Therefore, the Raman analysis is preferential for GaN, since the chemical bonding is a mixture of ionic and covalent bonding in GaN.

The Raman spectroscopy was performed by using the spectrometer MultiRAM (Bruker Optik GmbH, Germany) equipped with Nd:YAG laser (1064 nm) and the proprietary high sensitivity liquid nitrogen cooled Ge detector. FTIR transmission measurements were performed by using the Bruker Vertex 70 spectrometer combined with Bruker Hyperion 3000 microscope. The Raman and IR transmittance spectra were examined in the spectral range of 650−4000 cm^{-1} wave numbers ν with the spectral resolution of 4 cm^{-1} obtained by averaging 256 interferograms. The UV-VIS-NIR range transmission spectra were recorded by using a Perkin-Elmer LAMBDA 1050 spectrophotometer.

4. Investigation of defects in GaN structures

4.1. Spectroscopy of native and radiation-induced defects in AT GaN

The AT GaN exhibits significantly reduced densities of the native defects relative to other technology GaN (HVPE, MOCVD) materials and can be grown in large scale [122]. The AT GaN materials doped with Mn (GaN:Mn) and Mg (GaN:Mg) were studied in order to estimate the possibilities in fabrication of particle detectors. The Mn impurities in GaN may act as compensating centres for unintentionally introduced donor-type defects. It is noteworthy that, the Mg impurities act as the dopants in formation of the p-type conductivity GaN.

4.1.1. Ammonothermally grown bulk GaN samples

The high quality bulk ammonothermal GaN (AT-GaN) samples were fabricated at AMMONO company [122]. These samples were made as 400−450 μm thick wafers of the GaN doped with Mg and Mn. The AT GaN samples were irradiated by nuclear reactor neutrons using wide range of fluences ($10^{12} - 5\times10^{16}$ cm^{-2}) at TRIGA reactor of Jožef Stefan Institute in Ljubljana [123]. A fluence has been evaluated by using the equivalent to NIEL damage of the 1 MeV neutron irradiation, widely used for estimation of the effective fluence within sensor characteristics [124]. Moreover, reactor neutron irradiations are suitable for emulation of the evolution of the particle detector functionality during LHC experiments, as homogeneous damage is created.

4.1.2. ESR spectra

Electron spin resonance (ESR) spectroscopy was employed to detect the spin active defects in AT GaN crystals doped with Mn and Mg impurities. The fine structure of Mn^{2+} ion with spin S=5/2 in GaN provides a characteristic ESR spectrum (Fig. 4.1a). Each of the fine structure line is split into six lines by hyperfine interaction of Mn^{2+} nuclei with spin I=5/2. The observed absorption transitions are allowed according to the selection rules of $\Delta m_S=\pm1$ and $\Delta m_I=0$, where m_S and m_I denote the magnetic quantum numbers of electron system and Mn nuclei, respectively. The angular variations of ESR spectra (Fig. 4.1b) have been simulated using EasySpin simulation platform [125] and the spin

hamiltonian parameters taken for Mn^{2+} impurity [126]. The simulated results confirm the presence of the Mn^{2+} impurities.

Concentration of the Mn^{2+} impurities has been estimated from the measured ESR spectrum (Fig. 4.1a) using the double integration method [127] and by applying the software installed on Bruker Elexsys E-580 spectrometer. The concentration of Mn^{2+} impurities has been found to be 1.3×10^{18} cm^{-3} for the pristine GaN:Mn crystal. ESR signal for the pristine GaN:Mg crystal (Fig. 4.2) was below detection limit. This implies that AT GaN crystals were heat treated after Mg impurity introduction [128].

In the ESR spectra measured on the irradiated GaN:Mg crystals, the Mn^{2+} related lines also appear at irradiation fluences of $\geq10^{16}$ cm^{-2} (Fig. 4.2). Seems, Mn impurities are also present in the Mg-doped AT GaN samples. The intensity of these lines increases with enhancement of fluence. Radiation modifies the configuration of Mn impurity within crystal lattice and results the Mn ascribed ESR resonances in GaN:Mg ESR spectra. In ESR spectra, recorded on the highest fluence $\Phi=5\times10^{16}$ cm^{-2} irradiated GaN:Mg, a trace of the additional lines can be observed for the 320–380 mT magnetic field range. In order to resolve the origin of these lines, ESR spectra were measured at low temperature T=100 K and the higher microwave power (150 mW). This regime allowed for saturating the Mn^{2+} related lines and highlighting of the additional lines in the 320–380 mT magnetic field range (Fig. 4.3a).

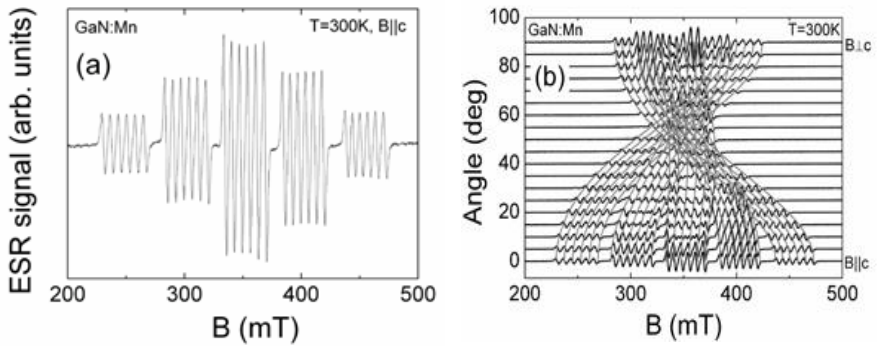

Fig. 4.1 ESR spectrum measured at room temperature on the pristine GaN:Mn crystal (a) and comparison of the simulated (grey lines) and experimental (black lines) angular variations of this ESR spectra (b). [A4].

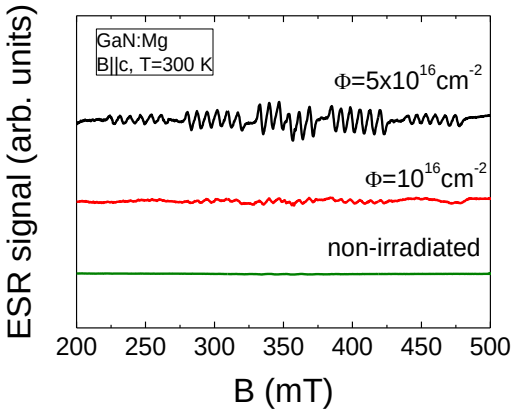

Fig. 4.2 ESR spectra recorded at room temperature on pristine and neutron irradiated AT GaN:Mg crystals [A4].

The simulated spectrum, using spin Hamiltonian parameters taken from [129,130], is in a good agreement with the experimental one (Fig. 4.3a), implying that the observed spectrum might be related to the complexes of gallium vacancy and substitutional oxygen $V_{Ga}O_N$ (as observed by the authors [129,130] in 2 MeV electron irradiated hydride vapour phase epitaxy (HVPE) GaN). Alternatively, other authors [131,132] associated the similar ESR spectra (observed in high-energy electron, proton and swift heavy Si ion irradiated HVPE GaN) with nitrogen split interstitial defect $(N–N)_N$.

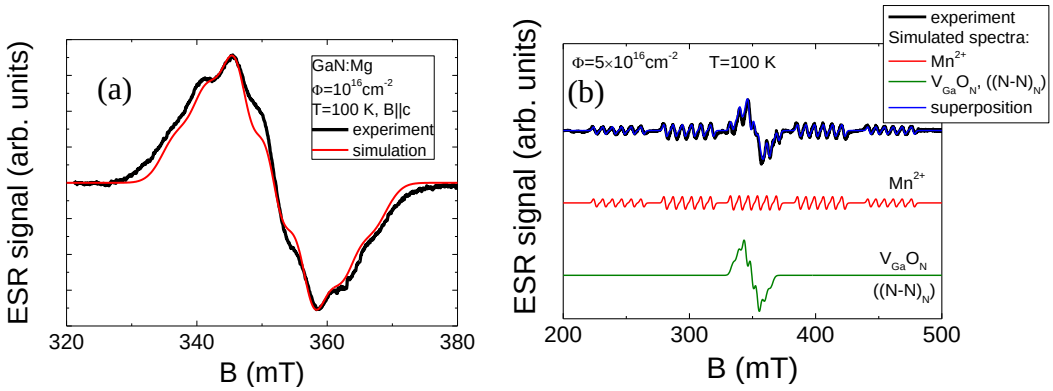

Fig. 4.3 The experimental and simulated ESR spectra, in GaN:Mg (a) and GaN:Mn (b) crystal irradiated with neutrons of fluence Φ=10^{16} cm^{-2}, measured at 100 K [A4].

The ESR spectrum, recorded at T=100 K on GaN:Mn crystal, irradiated with neutrons of fluence Φ=5×10^{16} cm^{-2}, was simulated at assumption of the superposition of Mn^{2+} impurity and $V_{Ga}O_N$ defect related resonances (Fig. 4.3b). The simulated ESR spectra are in good agreement with the experimental spectra.

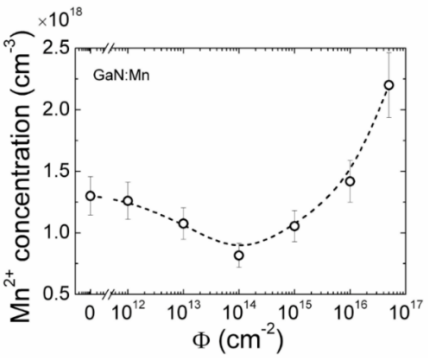

Fig. 4.4 Variations of Mn^{2+} concentration in GaN:Mn crystals as a function of neutron irradiation fluence [A4].

The values of spin-active Mn^{2+} concentration in GaN:Mn samples were obtained using the double integration method [127]. These values varies non-monotonically with enhancement of irradiation fluence (Fig. 4.4). This implies that neutron irradiation determines the transforms of Mn impurities by changing their spin-activity.

4.1.3. Spectra of Raman scattering, FTIR and optical transmission

The Raman spectra, recorded on the pristine and irradiated GaN:Mg and GaN:Mn samples in backscattering configuration, are shown in Fig. 4.5. There are no apparent shifts in the positions of the spectral peaks between the GaN:Mg and GaN:Mn materials. Also, no spectral changes were observed when comparing Raman spectra recorded on pristine and irradiated AT GaN samples. These observations are in agreement with Raman spectroscopy results obtained in recent study on MOCVD GaN materials irradiated with high fluences up to 3.7×10^{16} n/cm^2 [133], in which no significant changes were observed in the Raman spectra, when comparing the pristine and neutron irradiated samples.

Raman spectral peaks observable at 144, 568 and 734 cm^{-1} are interpreted [134] as the E2 (low and high frequency) and A1 (high frequency) phonon modes, respectively. The most intensive Raman spectral peak at 568 cm^{-1} is ascribed to the optical phonon (E2, high frequency), which indicates a relaxed (strain-free) crystal [135]. The peak at 520 cm^{-1} is associated with the LPP (LO phonon-plasmon). This is also a function of free electron concentration [136]. This LPP peak is overlapped with the peak at 531 cm^{-1} ascribed to the A1 (TO) phonon mode [137]. The origin of the broad peak, observed at around 400 cm^{-1},

is still not clear. The discussed structure of Raman spectra, recorded in the pristine and irradiated AT GaN samples, implies no radiation-induced deformations of GaN crystal lattice.

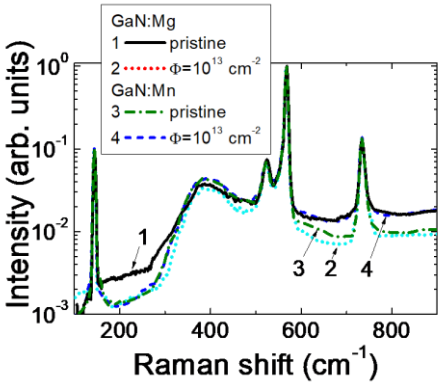

Fig. 4.5 Raman spectrum recorded on pristine and neutron irradiated (Φ=10^{13} cm^{-2}) AT GaN:Mg as well as GaN:Mn materials [A4]. The intensity of the Raman spectral peaks is normalized to the most intensive spectral peak at 568 cm^{-1} [A4].

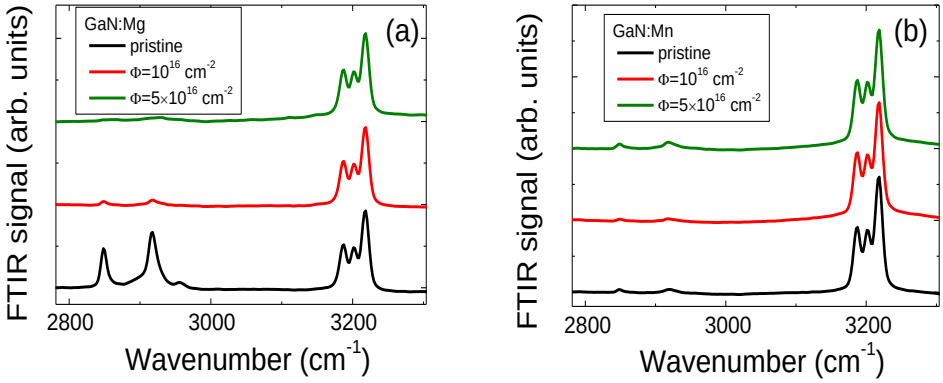

Fig. 4.6 FTIR spectra recorded on Mg (a) and Mn (b) doped AT GaN samples of pristine and neutron irradiated materials. The curves are shifted along the y-axis by arbitrary units [A4].

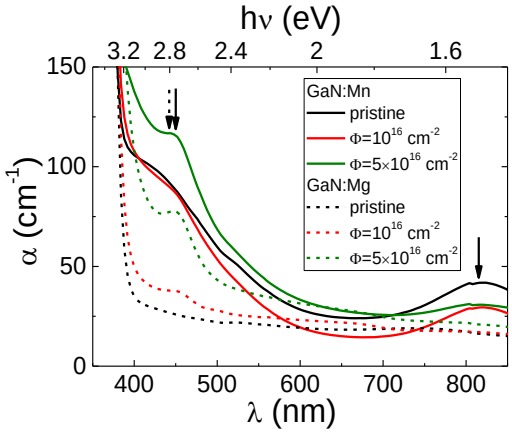

Fig. 4.7 Absorption spectra recorded in pristine Mn- and Mg-doped AT GaN and in the neutron irradiated samples [A4].

FTIR spectra, obtained for the pristine and heavily irradiated samples of Mg- and Mn-doped AT GaN materials, are shown in Fig. 4.6. Vibrational modes observed at 3186, 3202 and 3217 cm^{-1} have been ascribed to the Ga vacancy-multihydrogen complexes [78,138,139]. The amplitudes of these peaks are almost independent of irradiation fluence. Peaks at 2848, 2917 and 2955 cm^{-1} are most commonly associated with the CH localized vibrational modes [140]. Other authors also showed [141] that the CH ascribed wave numbers could vary between 2847 and 2853 cm^{-1}, while the CH_2 mode varies between 2910 and 2924 cm^{-1}, and the CH_3 mode varies between 2955 and 2963 cm^{-1} [141]. These variations of the frequency of the CH modes appear due to local strains generated from the dislocations [141]. The appearance of CH vibrational modes indicates that the H atom is directly bonded to the C atom. Also, it has been infered that C atoms are likely to occupy the N site in GaN lattice [142]. Intensity of these CH vibrational modes is obtained to be higher in GaN:Mg than that in GaN:Mn. This indicates that the concentration of carbon in GaN:Mg is larger than that in GaN:Mn. With increasing neutron irradiation fluence, the intensity of FTIR spectral peaks ascribed to the CH modes, decreases significantly for GaN:Mg material.

The absorption spectra, in the UV-NIR range, obtained for the pristine and neutron irradiated (Φ=10^{16} cm^{-2} and Φ=5×10^{16} cm^{-2}) AT GaN samples, are illustrated in Fig. 4.7. The enhanced absorption in the spectral range of 2.8−3.3 eV might be related to the hydrogenated gallium vacancies [143]. Other authors [144] proposed that the broad band in the spectral region above 2 eV can be attributed to the photo-ionization involving transitions $A^{-/0}$ from GaN valence band to a partially filled level, where A^- is the ionized Mn^{2+} (d^5) active acceptor (also observed in ESR spectra). These authors [144] proposed that the absorption peak at 1.5 eV, observed only for GaN:Mn material, should be ascribed to the electronic transitions related to the A^0 configuration.

Neutron irradiations lead to formation of Ga vacancies those change a configuration of the ESR active centres Mn^{2+}, causing the enhancement of absorption at 2.75 eV. In the GaN:Mn material, the electrically neutral

configuration of Mn impurities is also activated by radiation defects. The formation of Ga vacancies in AT GaN:Mn changes the configurational of the ESR active centres Mn^{2+}. This may be a reason for the appearance of a minimum in the Mn^{2+} concentration variations dependent on neutron irradiation fluence (Fig. 4.4).

4.1.4. Photoluminescence characteristics

The time-integrated PL (TI-PL) and the time-resolved (TR-PL) PL measurements were implemented at high excitation level ($n_{ex}\approx10^{18}$ cm^{-3}). The TI-PL spectra, obtained for the pristine and neutron irradiated AT GaN:Mg using different integration windows (Fig. 4.8), show that the intensity of the UV-PL band varies non-monotonically with enhancement of the irradiation fluence. Absolute values of UV-PL intensity are larger for 50 ns time-domain than those for 500 ns one, indicating that the rate of the UV-PL is the fastest in comparison with B-PL and YG-PL. This might imply that a coefficient (B) of the radiative band-to-band type recombination varies with imperfections in a GaN crystal lattice. The UV-PL intensity values are obtained to be significantly lower for the pristine GaN material than those for the neutron irradiated. This might also imply that the coefficient B is larger for the pristine material leading to faster reduction of excess carrier density through UV-PL channel. In this case, an integration time-domain of 50 ns is too long, and the temporal resolution in scanning-steps is insufficient to collect UV light emitted within a relatively short time-scale (50 ns). This explanation is confirmed by the reduction of UV-PL with increase of integration time-domain (to 500 ns) for the irradiated samples. By comparing intensity of the B-PL and YG-PL bands, recorded using 50 ns and 500 ns time-domains, the faster B-PL process can be infered. The decrease of the B-PL intensity has been observed with enhancement of neutron fluence Φ. The YG-PL band dominates in spectra integrated over 500 ns time-domain, implying that excess carrier decay through an YG-PL channel appears to be the slowest radiative recombination process. Moreover, intensity of YG-PL decreases with enhancement of Φ, in agreement with B-PL intensity changes as a function of

Φ. The B-PL and YG-PL bands are commonly ascribed to the transitions of carriers within DAP [145].

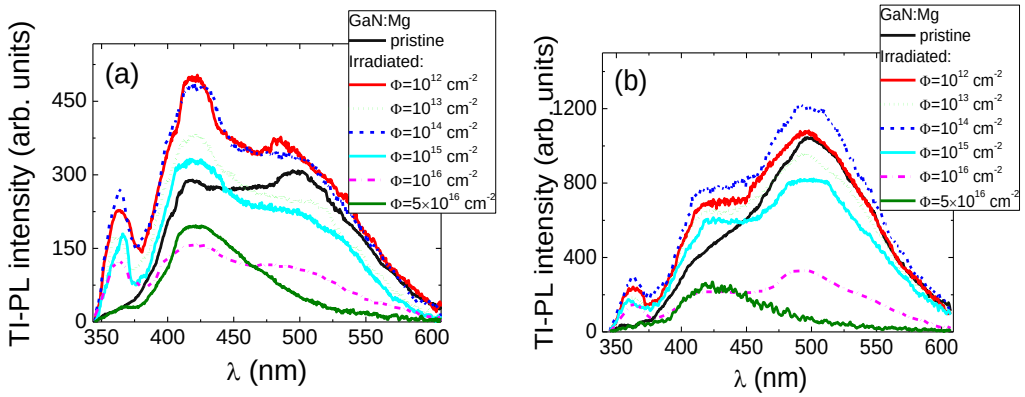

Fig. 4.8 TI-PL spectra of pristine and irradiated AT GaN:Mg. The time-integration windows were 50 ns (a) and 500 ns (b) [A4].

Fluence-dependent TI-PL spectra, registered in GaN:Mg, are shown in Fig. 4.9 for different integration time values. Using an integration window of 5000 ns, the intensity of the YG-PL peak decreases faster than the intensity of the B-PL peak in heavily irradiated sample. For the shortest integration window (5 ns), the UV-PL peak prevails in TI-PL spectra.

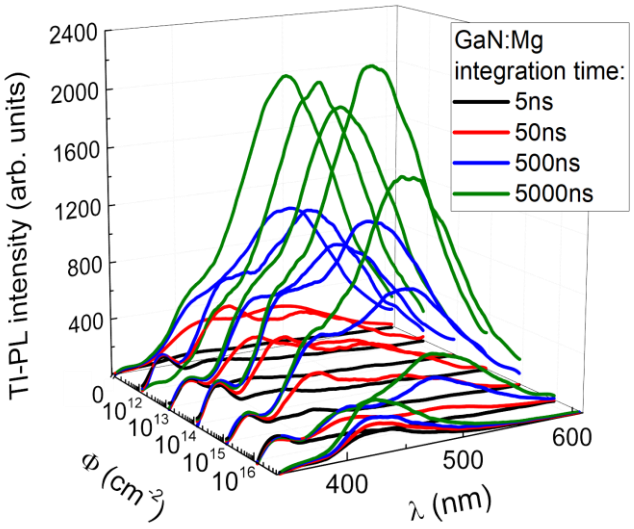

Fig. 4.9 Evolution of the TI-PL spectra with neutron fluence in AT GaN:Mg varying integration time-domains [A4].

The B-PL band is commonly attributed to the V_{Ga} complex as $V_{Ga}O_N$ and $V_{Ga}H_N$ in un-doped GaN [145]. The fluence-dependent changes of the B-PL intensity might be related to the increase of concentration of the V_{Ga} related defects. The decrease of the B-PL intensity after irradiation with fluences

$\Phi \geq 10^{16}$ cm^{-2} might be related to the increased density of non-radiative recombination defects. The YG-PL bands are likely to be attributed to the two charge states of the complex $V_{Ga}O_N$ [146,147]. Nevertheless, recent studies, based on the PL measurements and the hybrid density functional theory, suggest that the YG-PL bands with maximums at 2.1 eV and 2.4 eV [148] are the most likely to be associated with the C related defects (C_N [149] and C_NO_N [150]).

The TR-PL decay characteristics were recorded by integrating PL signals over narrow spectral domains (UV range (350−370 nm), B-PL range (400−450 nm), YG-PL (490−570 nm)) range. Variations of the TR-PL transients, recorded for the pristine and irradiated material samples (Fig. 4.10), indicate the non-exponential PL relaxation. The non-exponential PL transients might be related to the radiative carrier recombination processes through DAP [151,152].

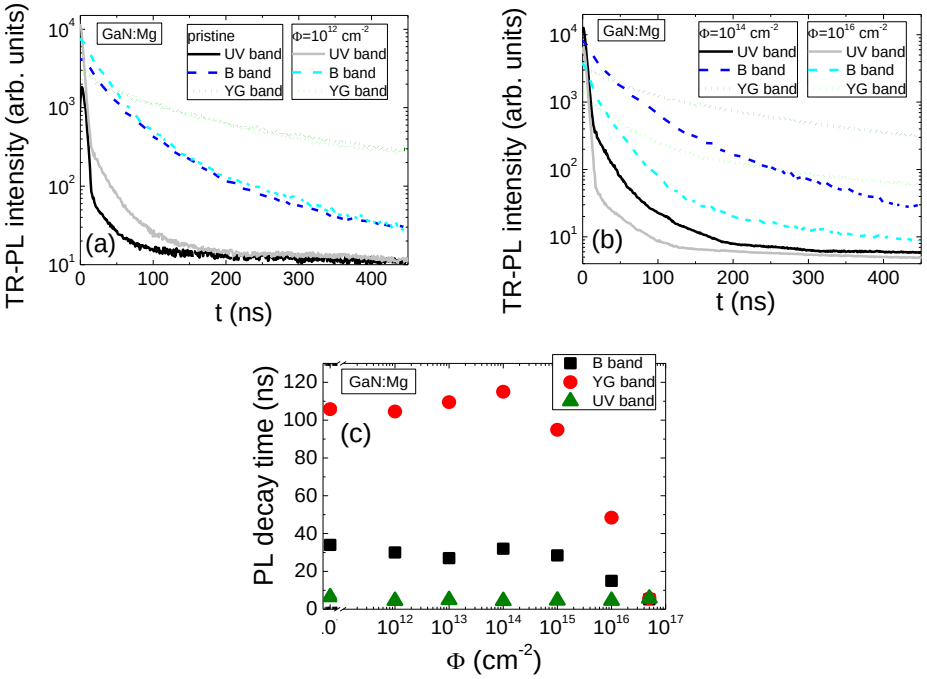

Fig. 4.10 The TR-PL decay transients registered for the UV, B and YG spectral intervals in the GaN:Mg samples of pristine and irradiated with low (a) and high (b) fluences material. Instantaneous lifetimes of the PL decay for the UV-PL, B-PL, and YG-PL band emission in GaN:Mg samples as a function of neutron irradiation fluence (c) [A4].

Fig. 4.10c also shows that values of the instantaneous PL decay times are close for the pristine material and small fluence irradiated samples. The shortest PL decay times are obtained for UV-PL while the longest ones are inherent for

YG-PL spectral range. The significant shortening of the instantaneous PL decay times is clearly observed for samples irradiated with the largest fluence (Fig. 4.10), especially for B-PL and YG-PL bands. The similar PL decay times, estimated for B-PL, YG-PL and UV-PL bands recorded on samples irradiated with the Φ=5×10^{16} cm^{-2}, might be an indication that the PL processes over all the mentioned PL bands are governed by the rate of the non-radiative decay of excess carriers.

The comparison of SS-PL spectra for GaN:Mg (Fig. 11a) and GaN:Mn (Fig. 11b) indicates, that UV-PL intensity considerably decreases with enhancement of Φ for GaN:Mg, while this UV-PL intensity is nearly independent of Φ for GaN:Mn.

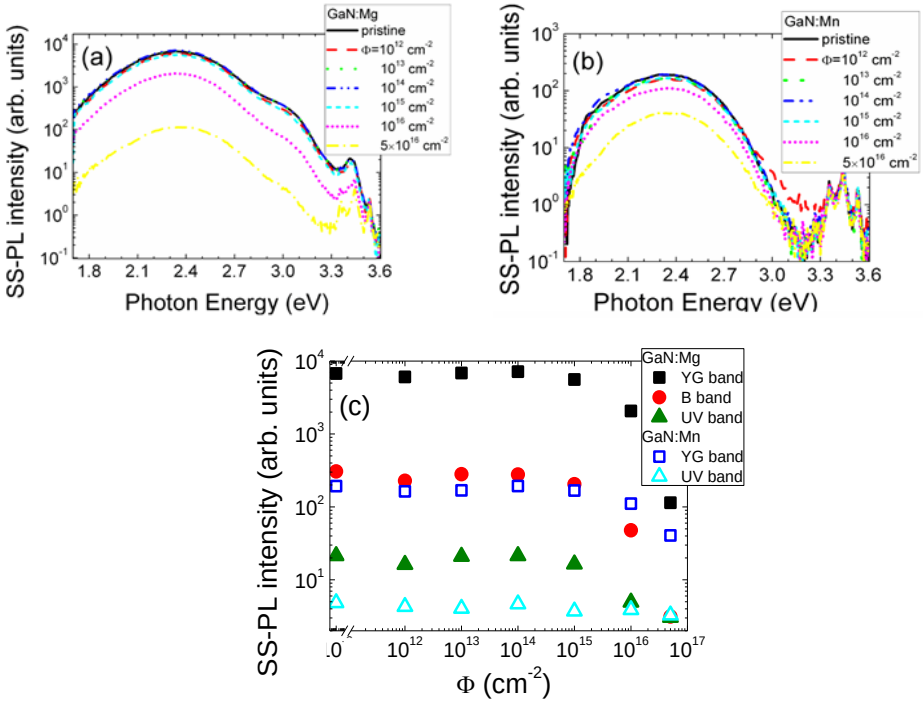

Fig. 4.11 SS-PL spectra of AT GaN:Mg (a) and GaN:Mn (b) materials. The fluence-dependent peak intensities for the PL bands in GaN:Mg and GaN:Mn samples (c) [A4].

The YG-PL is the dominant peak within SS-PL spectra recorded for both GaN:Mg and GaN:Mn samples. The broad YG-PL band is commonly attributed to the deep level defects with strong electron-phonon coupling [145]. The red-PL (R-PL) peaked at 1.9 eV appears as a shoulder to the YG-PL band. The R-PL is usually related to the $Mn^{3+/2+}$ dopants, those act as the acceptor centres forming a level located at 1.8 eV above the valence band [153]. Recent studies,

performed on the unintentionally doped n-type AT GaN [154], also showed the Mn concentration dependent degradation of the luminescence. For B-PL, YG-PL and R-PL bands (Fig. 4.11), the PL intensity decreases with enhancement of irradiation fluence in GaN:Mg samples faster than that in GaN:Mn. The faster decrease of PL intensity may therefore indicate the higher introduction rate of the radiation defects for the GaN:Mg, acting as the non-radiative recombination centres.

Fluence-dependent variations of the peak intensity of YG-PL, B-PL and UV-PL bands for GaN:Mg and GaN:Mn as a function of neutron fluence are almost invariable in the range of the moderate irradiation fluences ($\leq 10^{15}$ cm^{-2}), demonstrating the high radiation hardness of AT GaN materials.

4.1.5. Pulsed photo-ionization spectra

The PPIS measurements were performed by combining excitation pulses t_{ex}=40 fs and t_{ex}=4 ns laser pulses to clarify the role of electron-phonon coupling. The measured MW-PC signal amplitude is proportional to the excess carrier density, generated by photo-ionization. Thus, the photo-ionization spectrum is obtained as the MW-PC signal amplitude dependence on photon energy. The MW-PC transients recorded on the pristine AT-grown GaN:Mn by using t_{ex}=4 ns and t_{ex}=40 fs duration pulses and excitation photon energies $h\upsilon$=1.5 eV and $h\upsilon$=2.5 eV are shown in Fig. 4.12. The decay appears to be at least an order of magnitude faster when the t_{ex}=40 fs pulses are employed compared to that at nanosecond excitation pulses.

Variations of carrier recombination lifetime (τ_R) as a function of photon energy, when using t_{ex}=4 ns pulses, and the PPIS spectra recorded on pristine and neutron irradiated (Φ=10^{16} n/cm^2) GaN:Mg samples are illustrated in Fig. 4.13a. The Kopylov-Pikhtin [114] approach (Eq. 3.18) has been applied for fitting the $U_{MW\text{-}PC,0}((h\nu)$ in the experimental spectra. The carrier lifetime τ_R variations with excitation wavelength changes, observed for the pristine GaN:Mg (Fig. 4.13a), indicated that nearly constant τ_R is associated with the shallow PPIS spectral step. Carrier lifetime decreases, leading the shortened τ_R

values, in the range of moderate excitation photon energies used, with further τ_R increase and non-monotonous variation in the range of the largest photon energies applied (Fig. 4.13a). The τ_R variations can be explained by the processes of the photo-neutralization and photo-ionization of charged traps.

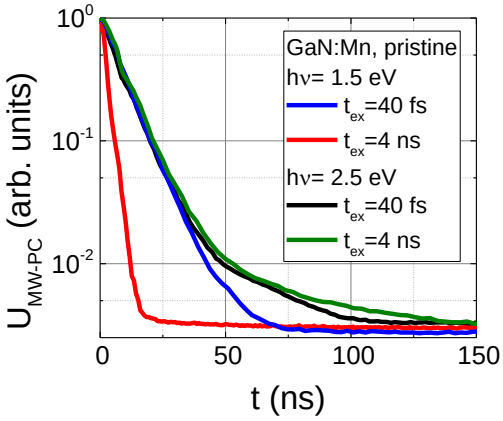

Fig. 4.12 The MW-PC transients recorded by using tuneable wavelength excitation pulses of t_{ex}=4 ns and t_{ex}=40 fs duration and excitation photon energies $h\upsilon$=1.5 eV and $h\upsilon$=2.5 eV.

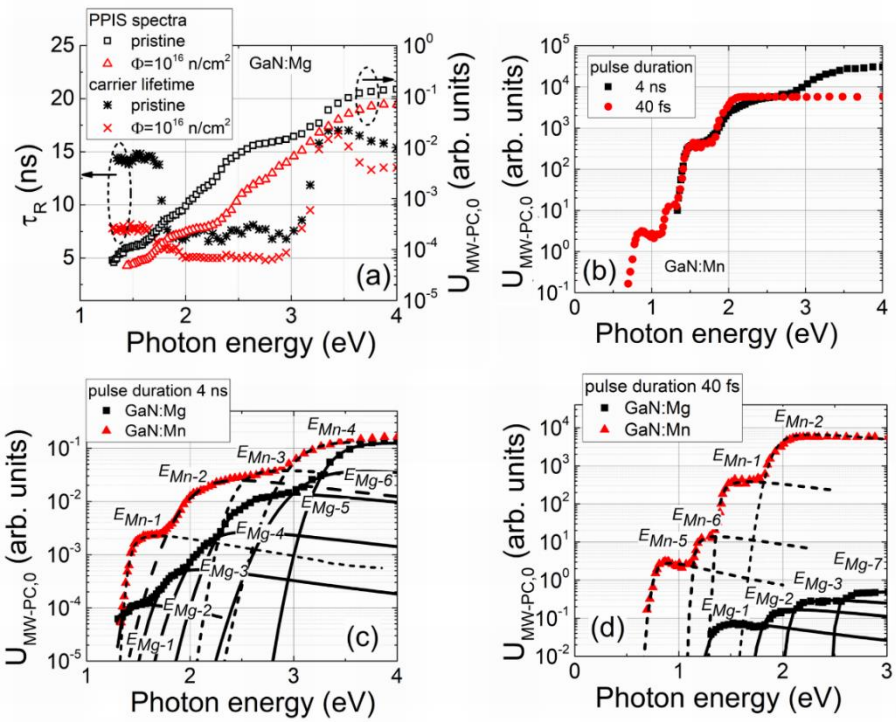

Fig. 4.13 (a) Variations of the τ_R and the PPIS spectra recorded on pristine and irradiated (Φ=10^{16} n/cm^2) GaN:Mg samples (t_{ex}=4 ns). (b) Comparison of the PPIS spectra recorded on a pristine AT-grown GaN:Mn sample by using t_{ex}=4 ns and t_{ex}=40 fs duration. Fitting of the PPIS spectra recorded on pristine materials using either 4 ns (c) or 40 fs (d) excitation pulses.

The excitation pulses of t_{ex}=40 fs seem to be shorter than the energy relaxation time, and photo-ionization process runs within nearly adiabatic

regime, while for the t_{ex}=4 ns pulses, it leads to a process integrated over energy. A shift of the position of the step peak and a steepness of the spectral-step slope can be expected relative to the pronounced electron-phonon coupling, in the case of short excitation pulses. The PPIS spectra, obtained for GaN:Mn by using different excitation pulses, are compared in Fig. 4.13b. The same dominant spectral steps have been observed in PPIS spectra recorded for pristine GaN:Mn sample (Fig. 4.13b). The spectral steps, obtained for different t_{ex}, qualitatively correlated. The most significant difference in abruptness of spectral step slope has been observed for the spectral peak at ~2 eV. This implies the strongest electron-phonon coupling ascribed to this defect where the lower abruptness of spectral step for 4 ns pulses is observed. For quantitative characterization of the electron-phonon coupling, the Γ factors have been evaluated by fitting (using Eq. 3.18) the shape and spectral position of a peak of each spectral step within measured spectrum.

Four trap levels have been revealed for the GaN:Mn samples and six traps for the GaN:Mg samples by fitting the experimental spectra recorded by using an excitation pulses of t_{ex}=4 ns duration (Fig. 4.13c). The photo-activation energies E_{ph} (with fitting uncertainties of about 5 %) and Γ parameters of the predominant centres have been identified, as listed in Table 4.1.

Table 4.1 Values of the photo-activation energy and of broadening parameter Γ extracted from fitting of the PPIS peaks recorded by using the 4 ns excitation pulses.

GaN:Mn				
Pristine		**Irradiated with Φ=10^{16} cm^{-2}**		
E_{ph} (eV)	Γ	E_{ph} (eV)	Γ	Defect type
$E_{Mn\text{-}1}$=1.40	0.05	$E_{Mn\text{-}1}^{irr}$=1.42	0.08	Mn related [155]
$E_{Mn\text{-}2}$=1.98	0.25	$E_{Mn\text{-}2}^{irr}$=1.98	0.22	Mn related [144]
$E_{Mn\text{-}3}$=2.40	0.15	$E_{Mn\text{-}3}^{irr}$=2.39	0.25	Ga_I interstitial [156]
$E_{Mn\text{-}4}$=2.97	0.25	$E_{Mn\text{-}4}^{irr}$=2.96	0.28	Unidentified [156]
GaN:Mg				
$E_{Mg\text{-}1}$=1.30	0.02	–	–	C_I acceptor [157,158]
$E_{Mg\text{-}2}$=1.75	0.18	$E_{Mg\text{-}2}^{irr}$=1.75	0.23	Mg [159]
$E_{Mg\text{-}3}$=2.07	0.23	$E_{Mg\text{-}3}^{irr}$=2.05	0.27	V_{Ga} vacancy [160]
$E_{Mg\text{-}4}$=2.39	0.15	$E_{Mg\text{-}4}^{irr}$=2.38	0.25	Ga_I interstitial [156]
–	–	$E_{Mg\text{-}7}^{irr}$=2.45	0.16	V_{Ga} vacancy [158]
$E_{Mg\text{-}5}$=3.10	0.32	$E_{Mg\text{-}5}^{irr}$=3.10	0.35	Mg [159]
$E_{Mg\text{-}6}$=3.30	0.2	$E_{Mg\text{-}6}^{irr}$=3.30	0.27	V_N vacancy [156]

Table 4.2 Values of the photo-activation energy E_{ph} and of broadening parameter Γ extracted from fitting of the PPIS peaks recorded by using the 40 fs excitation pulses.

GaN:Mn					GaN:Mg		
Pristine		Irradiated with Φ=10^{16} cm^{-2}			Pristine		
E_{ph} (eV)	Γ	E_{ph} (eV)	Γ	Defect type	E_{ph} (eV)	Γ	Defect type
$E_{Mn\text{-}5}$=0.75	0.05	–	–	Uniden-tified	$E_{Mg\text{-}1}$=1.27	0.08	C_I acceptor [157]
$E_{Mn\text{-}6}$=1.14	0.03	$E_{Mn\text{-}6}^{irr}$=1.09	0.11	Uniden-tified	$E_{Mg\text{-}2}$=1.78	0.07	Mg [159]
$E_{Mn\text{-}1}$=1.39	0.04	$E_{Mn\text{-}1}^{irr}$=1.41	0.03	Mn related [155]	$E_{Mg\text{-}3}$=2.06	0.05	V_{Ga} vacancy [160]
$E_{Mn\text{-}2}$=1.90	0.08	$E_{Mn\text{-}2}^{irr}$=1.91	0.08	Mn related [144]	$E_{Mg\text{-}7}$=2.50	0.03	V_{Ga} vacancy [158]

For 40 fs excitation pulses (Fig. 4.13d), the PPIS recorded on GaN:Mn exhibit the additional peaks $E_{Mn\text{-}5}$ and $E_{Mn\text{–}6}$ together with Mn impurities ascribed levels $E_{Mn\text{-}1}$ and $E_{Mn\text{-}2}$, observed in PPIS recorded using 4 ns excitation pulses. The origin of these deep levels with energies of $E_{Mn\text{–}5}$=0.75 eV and of $E_{Mn\text{-}6}$=1.14 eV had not been found in literature. In Mg-doped pristine GaN samples, an additional peak $E_{Mg\text{-}7}$=2.50 eV has been deduced by fitting spectra recorded by using 40 fs pulses together with those traps $E_{Mg\text{-}1}$, $E_{Mg\text{-}2}$ and $E_{Mg\text{-}3}$ revealed by measuring PPIS using 4 ns pulses. The parameters extracted from fittings of PPIS, recorded using t_{ex}=40 fs pulses, are listed in Table 4.2.

Introduction of defects by neutron irradiations does not change considerably a structure of the photo-ionization spectra (Fig. 4.13a), where the same PPIS peaks, inherent for pristine and irradiated materials have been be resolved. Values of fitting parameters are listed in Table 4.1 and Table 4.2. As an exception, the deep centre with energy of $E_{Mg\text{-}7}^{irr}$=2.45 eV can additionally be separated in the PPIS spectrum, recorded for the irradiated GaN:Mg samples. The main difference appears in density of photo-active centres, which can be deduced from variations of the $U_{MW\text{–}PC,0}$, when comparing PPIS obtained for the pristine and 10^{16} n/cm^2 neutron fluence irradiated samples. Such the observations can be explained by a rather small concentration ($\leq 10^{16}$ cm^{-3}) of the introduced radiation defects in comparison with intrinsic defect and dopant densities ($>10^{18}$ cm^{-3}). The type of the resolved traps (relative to a charge-state) seems to be not changed under neutron irradiations, as profile of carrier lifetime variations

retains (Fig. 4.13a). Nevertheless, carrier lifetime values, significantly reduced for the irradiated samples, indicating that the radiation defects act mostly as carrier recombination centres.

The Γ parameter, which characterizes the strength of electron-phonon coupling, is obtained to be significantly different when comparing fitting parameters for PPIS recorded under 4 ns and 40 fs excitation pulses. The Γ parameter values, extracted from fitting of the PPIS peaks recorded by using the 4 ns excitation pulses, are significantly higher than those deduced by using the 40 fs excitation pulses. This indicates the stronger electron-phonon coupling for 4 ns excitation regimes.

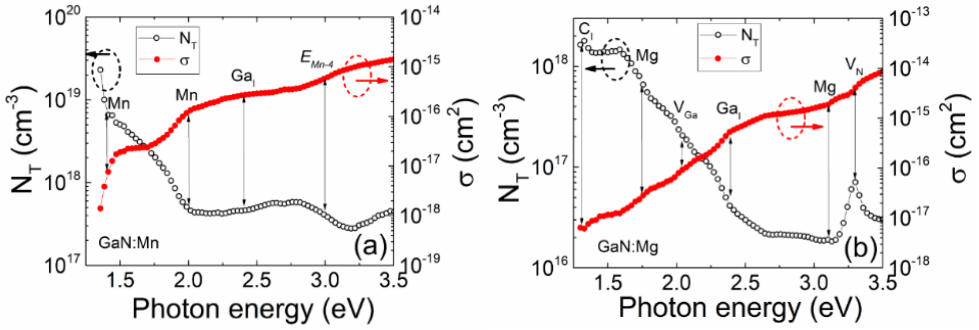

Fig. 4.14 Variations of cross-sections and of trap concentration as a function of excitation photon energy in the pristine GaN:Mg (a) and GaN:Mn (b), respectively. Vertical arrows indicate the peak positions of the PPIS steps, ascribed to different centres.

The cross-sections of the electron-photon coupling and the concentrations of defects have been estimated by combining values of the absorption coefficient, measured on each sample by using UV-VIS transmission [161], by calibrating the quantity of absorbed photons, using the transmitted beam energy measurements, by calibrating values of concentration of the main dopants, using the SIMS and ESR data [161], and relating them to the MW-PC peak values. The spectral variations of the cross-sections (σ) ascribed to several species of traps and trap densities (N_T) are depicted in Fig. 4.14 for GaN:Mg (a) and GaN:Mn (b) pristine materials, respectively. An increase of concentration of the neutron introduced radiation defects is also deduced from UV-VIS transmission spectra [161], while these radiation defects act mostly as the carrier recombination centres.

4.1.6. Variations of carrier recombination and charge collection characteristics

The time scale for MW-PC transients, registered for GaN:Mg is significantly longer than that for GaN:Mn (Fig. 4.15a). A fixed time-scale for the excess carrier density decrease (to a background level), indicates the small impact of the disorder effects associated with dislocations. In this case, the non-linear decay processes with simultaneous action of the radiative (as UV PL) and non-radiative recombination should be ascribed to deep levels. Such a process of the excess carrier variation in time ($n_{ex}(t)$) can be described [108] as follows:

$$n_{ex}(t) = \frac{n_{ex,0}\exp(-\frac{t}{\tau_R})}{1 + Bn_{ex,0}\tau_R[1-\exp(-\frac{t}{\tau_R})]} \quad (4.1)$$

Here, B is the coefficient of radiative recombination, τ_R is the carrier lifetime ascribed to the non-radiative recombination, and $n_{ex,0}$ is the excess carrier concentration at the peak of excitation. The parameter $n_{ex,0}$ is directly estimated using a transient taken from the experiment implemented at fixed excitation density. The excitation density is evaluated using the laser beam parameters and material absorption coefficient at fixed wavelength. The value of τ_R ascribed to each transient can also be estimated from the slope of the asymptotic (close to an exponential: $n_{ex,0}\exp(-t/\tau_R)/[1+B\tau_R n_{ex,0}]$) component within a recorded transient. Thus, values of B and τ_R are the only adjustable parameter involved into fitting of the experimental transients (Fig. 4.15b). The B coefficient of an estimated value of $(1–3)\times10^{-8}$ cm^3/s should be attributed to the UV recombination process.

The variations of MW-PC transients, as-recorded for the pristine and irradiated AT GaN, are caused by τ_R reduction with enhancement of neutron irradiation fluence (Fig. 4.15b).

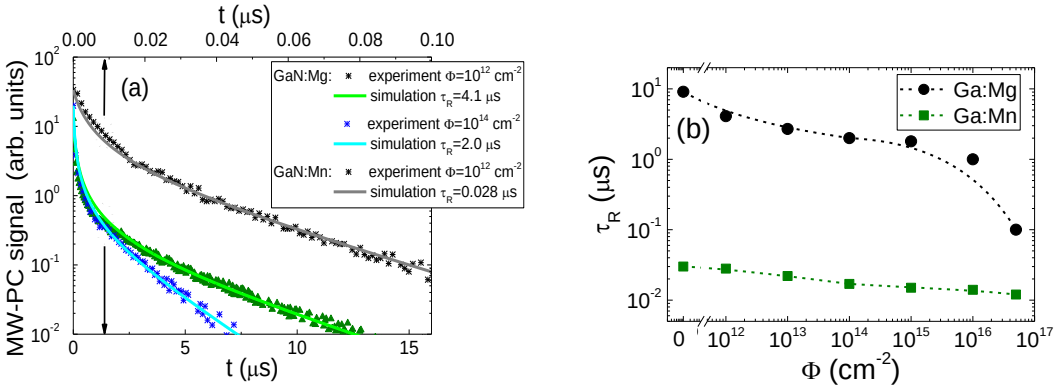

Fig. 4.15 The as-recorded MW-PC transients (symbols) and simulated (lines) carrier decay transients for the irradiated AT GaN:Mg and GaN:Mn samples (a) at fixed excitation intensity. Variation of values of the non-radiative recombination lifetimes (extracted form fits) as a function of neutron fluence, obtained for GaN:Mg and GaN:Mn samples (b).

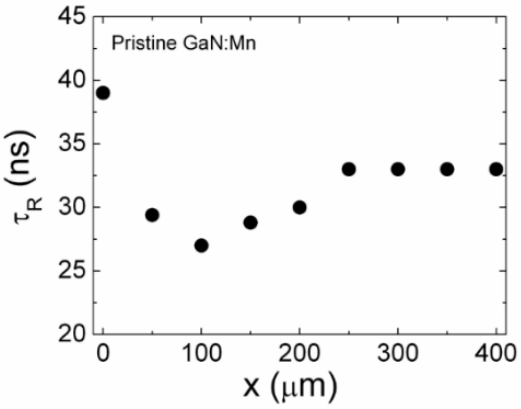

Fig. 4.16 Depth distribution of carrier recombination lifetime scanned within cross-sectional boundary of the 400 μm thick GaN:Mn wafer [A4].

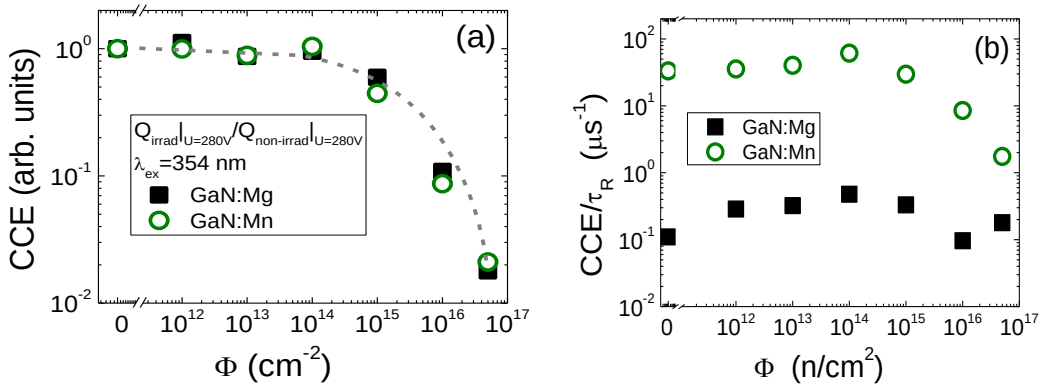

Fig. 4.17 The CCE normalized to a CCE value obtained for the non-irradiated sample (a) and the ratio of CCE and recombination lifetime (CCE/τ_R) (b) as a function of neutron irradiation fluence for Mg- and Mn-doped AT GaN samples.

Carrier recombination lifetime (τ_R) decreases by a factor of 100 in GaN:Mg obtained for neutron irradiated (with the largest Φ) samples, when comparing

with τ_R values, measured in pristine sample of the same material (Fig. 4.15b). While in GaN:Mn material, reduction of τ_R was obtained by factor of 3 over a wide range (10^{12} – 5×10^{16} n/cm^2) of neutron fluences. This indicates that radiation defects are the most efficient in reduction of carrier recombination lifetime on GaN:Mg material (where relatively long carrier lifetime is inherent). These results also indicate, that AT GaN is rather tolerant to neutron irradiations, relative to other MOCVD and HVPE GaN samples, irradiated by hadrons and examined by MW-PC technique [162,163].

The longer lifetimes obtained for the pristine GaN:Mg, relative to those in GaN:Mn, indicate that Mn impurities act as the fast recombination centres. Slight inhomogeneity of the lateral and depth distribution of dopants in the pristine Mg- and Mn-doped AT GaN samples has been deduced. There, τ_R variations have been obtained within MW-PC transient scans, performed on wafer boundary by depth profiling (Fig. 4.16). This τ_R profile over wafer thickness was scanned using boundary cross-sectional excitation by a sharply focused 351 nm laser beam and by probing by a MW antenna (in near-field mode) [108].

Carrier lifetime is one of the most important parameter of particle sensors, which determines the efficiency of charge collection (CCE) and a possibility to detect electrical signals on the background of electrical noises. The CCE has been evaluated by measuring the pulsed current responses of the capacitor-like sensor structures made of irradiated AT GaN samples and using a bias voltage of 280 V. The CCE has been evaluated by current integration in time over a TCT pulse. To calibrate the fluence-dependent CCE, the time integrated TCT signals for the irradiated material sensors were normalized to the TCT signals of the pristine material, separately for GaN:Mg and GaN:Mn. At low fluences ($\Phi\leq10^{14}$ n/cm^2), this CCE is almost constant and equal to the CCE of a sensor made of the non-irradiated material (Fig. 4.17). For the moderate fluences ($\Phi\geq10^{15}$ n/cm^2), the radiation defects lead to the decrease of CCE. At the highest irradiation fluences ($\Phi=5\times10^{16}$ n/cm^2), the CCE decreases to ~2.1 % and to

~7.5 % in Mg- and Mn-doped samples, respectively. To estimate the fluence-dependent variations of CCE due to changes of carrier transport parameters, the fluence-dependent characteristic CCE/τ_R has been analysed. A reduction of this CCE/τ_R parameter appeared to be faster in Mg-doped AT GaN material relative to that in Mn-doped samples. In agreement with this CCE/τ_R-Φ characteristic for GaN:Mg, the PL intensity decreases with enhancement of irradiation fluence faster than that in Mn irradiated AT GaN samples. This indicates the higher introduction rate of the non-radiative defects in GaN:Mg than that in GaN:Mn. The rather small variation of values of the CCE/τ_R parameter for a wide (Φ=10^{12}–10^{15} n/cm^2) range of fluences hints on the relatively high radiation hardness of AT GaN material.

The exceptionally long carrier lifetimes (up to several μs) in AT GaN:Mg make this material applicable in formation of thick particle sensors for detection of particles with small interaction cross-section. AT GaN material is also suitable for fabrication of the double-response particle sensors with properly low leakage currents. The nearly invariable values of charge collection efficiency and carrier lifetimes in AT GaN over wide range of moderate neutron fluences $\Phi \leqslant 10^{15}$ cm^{-2} confirmed the high radiation hardness of this material. These AT GaN features are essentially important for designing of scintillators and particle tracking detectors.

4.2. Analysis of defects and recombination characteristics in MOCVD grown GaN epi-layers

In many applications epitaxial layers with different doping levels or types of material are required. For GaN-on-Si technology, the usage of the MOCVD growth technique leads to a high density of screw and edge dislocations, threading the GaN layers. It has been observed [164] that the breakdown voltage of power devices can be limited by the buffer leakage current, which was determined by electrically active defects. Doping of GaN epitaxial layers with carbon offers new perspectives for reducing of this leakage current and for improving the breakdown voltages [148,165]. At the same time, trapping effects

in the AlGaN/GaN HEMTs are enhanced by the presence of C-related deep levels [148]. Different research studies had showed [148–150,166] that several deep centres were associated with carbon impurities. Therefore, the control of deep-level defects in III-nitride epitaxial layers is important in order to optimize the device performance.

4.2.1. MOCVD grown GaN epi-layers

GaN layers, unintentionally highly doped with C (reached concentrations of 5×10^{16} cm^{-3}), were grown on 200 mm Si substrates by MOCVD technology. A set of samples were prepared by varying the growth pressure and temperature in formation of the 1 μm thick GaN epilayers on top of an identical buffer structures consisting of AlGaN stress management layers and an AlN nucleation layer. Structure of the samples and their growth regimes are described in Fig. 4.18 and Table 4.3.

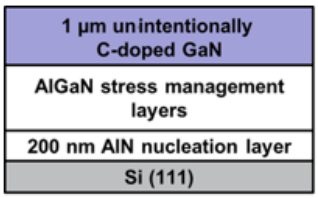

Fig. 4.18 Schematics of the sample structure.

Table 4.3 Description of growth conditions of GaN epi-layers.

	1040 ˚C	1060 ˚C	1080 ˚C
75 Torr	Sample 1A	Sample 1B	Sample 1C
200 Torr	Sample 2A	Sample 2B	Sample 2C

4.2.2. XRD investigation

The threading dislocation density (TDD) has been evaluated from the XRD measurements, assuming a random distribution of dislocations and using expression [167]:

$$\mathrm{TDD} = \beta^2/9b^2, \tag{4.2}$$

where β is the full width at half of maximum of XRD reflexes (ω-FWHM), and b is the length of Burgers' vector. The densities of the screw and edge type dislocations were determined using the XRD rocking curve measurements (ω-scans) at (0002) and (30-32) reflexes. The broadening (FWHM) of the (0002) peak within ω-scan is mainly determined by the screw dislocations [5]. On the

other hand, the broadening of the (30-32) reflection peaks is almost purely determined by edge type dislocations in GaN [5].

The estimated values of density of the edge (DED) and screw (DSD) dislocations [90] are plotted in Fig. 4.19 as a function of the sample growth parameters. The decrease of DED with enhancement of the growth temperature for layers grown at 75 Torr can be observed, while the DED increases with growth temperature for layers grown at 200 Torr. The DSD is nearly constant for 200 Torr grown epilayers, while these DSD have been found to be slightly lower for 75 Torr grown layers.

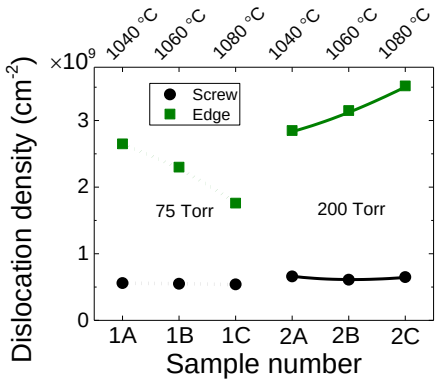

Fig. 4.19 Screw and edge dislocation densities in GaN layers grown by different regimes [A5].

The obtained dependences of dislocation density (DD) on growth parameters can be considered based on generally established variations of the growth rate with changes of temperature and pressure [88,168–170]. It can be roughly implied that the growth rate decreases with enhancement of the temperature and pressure for definite range of these parameters, while propagation, reactions and annihilation of dislocations lead to a decrease of the DD. This tendency is observed for investigated samples grown at 75 Torr pressure (Fig. 4.19). Under lower growth temperature, the higher density of structural defect, nitrogen vacancy and enhanced incorporation of impurities are typically observed due to a reduced surface diffusion of ad-atoms [170]. The higher pressure should affect the GaN growth by increasing the grain size and decreasing the tilt and twist boundaries. However, at elevated pressures, the parasitic reactions [7,8,171] in the gas phase between TMGa and NH_3 can be

more efficient. Thus, the opposite dependence between TDD and temperature, is observed for samples grown at 200 Torr pressure (Fig. 4.19). This indicates the lower crystal quality obtained at higher pressure (relative to 75 Torr) and the enhancement of structural defects with increasing of temperature. The rate of parasitic reactions might increase with temperature, especially for Ga related reactions [7].

4.2.3. Carrier recombination lifetimes extracted using MW-PC transients

The MW-PC transients exhibit a two-componential decay, inherent to GaN with rather high density (>10^8 cm^{-2}) of threading dislocations (Fig. 4.20).

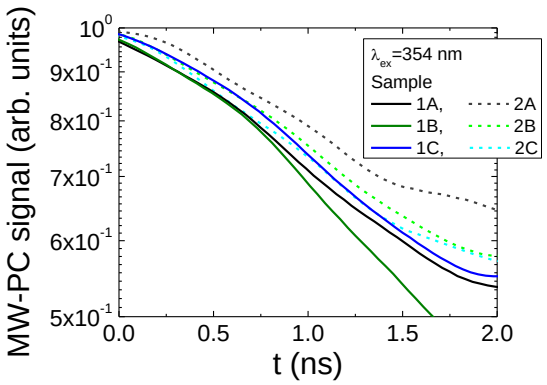

Fig. 4.20 MW-PC transients measured in GaN structures at the initial decay stage and with assumption that the decay starts from the peak of a transient.

According to the classical models of dislocations, a dislocation core is surrounded by a space charge region (SCR) and contains a barrier for one type of carriers [172]. For GaN, a screw dislocation can give rise to the deep gap states, ranging from 0.9 to 1.6 eV above the valence band, and shallow gap states at about 0.2 eV, below the conduction-band minimum [173,174]. The time scale for the initial MW-PC transient component covers a few ns range (Fig. 4.20). This decay component is ascribed to carrier recombination within a crystallite of the GaN single-crystal. The asymptotic decay constituent in the MW-PC transient of a few μs (Fig. 4.22) has been observed, which can be commonly attributed to the carrier trapping and anomalous diffusion through random-walk processes within dislocation clusters, surrounding the single-crystal regions. This process is commonly described by the stretch-exponent decay model. The carrier density relaxation process is complicated in the non-homogeneous

system. Trivial subtraction of the trapping component would formally reduce the de-convoluted τ_R value (Table 4.4), ascribed to the initial decay stage. The de-convoluted τ_R value is here obtained by correcting for delays due to the MW detector circuit. The procedure of a trivial subtraction of the trapping component is doubtful if the ratio (relative to the $A_{exc\ spot}$ excitation spot) of areas (volumes) of perfect (A_{cryst}) single-crystal GaN and dislocation clusters is not well defined. At TDD≥2×10^9 cm^{-2}, the linear distances L_{TD} between the adjacent dislocation cores might be estimated as L_{TD} ~200 nm, at assumption of a homogeneous distribution of dislocations. The space charge regions, surrounding the dislocations, lead to outspread of the disordered material within the inter-dislocation areas (A_{TD}). In this case the decay obeys a SER law [175], the carrier decay can be approximated as

$$n(t) \cong n_0 \left\{ \frac{A_{cryst}}{A_{exc\ spot}} \exp\left(-\frac{t}{\tau_R}\right) + \frac{A_{TD}}{A_{exc\ spot}} \exp\left(-\left(\frac{t}{\tau_{SER}}\right)^{\beta_{SER}}\right) \right\}, \qquad (4.3)$$

at assumptions of prevailing of the linear recombination of the same generation efficiency for excess carriers in the single crystal (τ_R) and defective material (τ_{SER}).

Table 4.4 Summary of the initial and the de-convolution procedure extracted values of carrier recombination lifetimes.

Sample No.	**Pressure/temperature**	**$\tau_{in,\ MW\text{-}PC}$ (ns)**	**τ_R (ns)**
2A	200 Torr/1040 C	3.6	2.5
2B	200 Torr/1060 C	3.1	2.2
2C	200 Torr/1080 C	3.0	2.1
1A	75Torr/1040 C	2.8	2.0
1B	75 Torr/1060 C	2.3	1.5
1C	75 Torr/1080 C	2.7	2.1

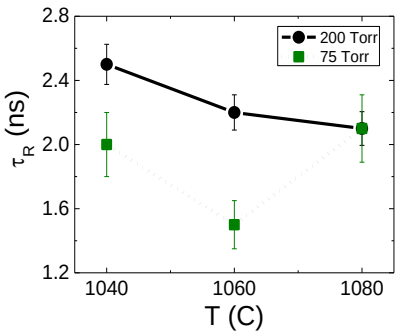

Fig. 4.21 τ_R in GaN crystallites within layers as a function of growth temperature when using different pressures [A5].

The effective decay lifetime ($\tau_{in,\ MW\text{-}PC}$) attributed to the recombination in crystallites (described by the first term in Eq. 4.3) can be estimated as a slope of the MW-PC signal relaxation on a semi-log scale, measured as a time interval at the exp(-1) level. Values of τ_R have been extracted using the de-convolution procedures and the parameters of the delays in the recording circuit. These $\tau_{in,MW\text{-}PC}$ and τ_R values are listed in Table 4.4.

Variations of τ_R as a function of the growth temperature are illustrated in Fig. 4.21. A reduction of carrier lifetime with enhancement of temperature can be deduced from Fig. 4.21, for layers grown using 200 Torr pressure. While, carrier lifetime was obtained to vary non-monotonically with enhancement of the growth temperature for GaN layers grown under 75 Torr pressure. Nevertheless, values of τ_R are close for both 75 Torr and 200 Torr grown at 1040 °C layers, where difference in the dislocation density (DD) is rather small. However, the opposite tendency of DD variations with growth temperature (Fig. 4.19) has been obtained for 75 and 200 Torr grown samples. The non-monotonous variation of the τ_R dependent on temperature for the 75 Torr grown samples can be explained by the enhanced role of the trapping component in the GaN material containing the largest density of dislocations. Unfortunately, the precision of the τ_R extraction is determined by the asymptotic carrier-trapping component.

The quality of the GaN crystallites might be also determined by the dislocation boundaries. Dislocations can be a sink for native point defects and impurities like carbon. So, this can be an additional factor, besides trapping, which can explain the non-monotonous characteristic of τ_R versus DD (Fig. 4.21). This for example, could be derived from the YG-TR-PL trend for 75 Torr, showing a maximum for the intermediate growth temperature, complementary to the non-radiative lifetime (Table 4.7).

The MW-PC transients, displayed by representing $\ln(-\ln(U_{MW\text{-}PC}(t)/U_{MW\text{-}PC\ peak})$ values as a function of $\ln(t)$, are illustrated for sample 2A in Fig. 4.22. Such a SER plot ($\ln[-\ln(U_{MW\text{-}PC}(t)/U_{MW\text{-}PC\ peak})]$ vs. $\ln[t]$) (where t is

normalized to a μs values inherent for the asymptotic display scale) is conventional [108,175] in estimation of the power index β_{SER} for a SER curve. This asymptotic component obeys stretched-exponential decay ($n(t) \sim n_{0SER} \times \exp[-(t/\tau_{SER}{}^{\beta_{SER}}]$) (Eq. 4.3).

The $\ln[-\ln(U_{MW\text{-}PC}(t)/U_{MW\text{-}PC\ peak})]$ values indicate good fit, as the linear dependence has been obtained. The initial decay, characterized by τ_R, has been ascribed to the recombination through point defects within crystallites. Values of the β_{SER} have been evaluated using ($\ln[-\ln(U_{MW\text{-}PC}(t)/ U_{MW\text{-}PC\ peak})]$ vs. $\ln[t/1\ \mu s]$) slopes obtained in SER plots for asymptotic decays (Table 4.5). The partial amplitude $A_{TD}/A_{exc\ spot}$, ascribed to the asymptotic decay component in GaN slightly depends on excitation intensity. The averages of these partial amplitudes ($A_{TD}/A_{exc\ spot}$) can serve for estimation of the carrier density fraction, attributed to the dislocation clusters. The partial amplitudes of $A_{cryst}/A_{exc\ spot}$ and $A_{TD}/A_{exc\ spot}$ have been also estimated from the semi-log plots (similar to that illustrated for the 2A sample in the inset for Fig. 4.22a) and are listed in Table 4.5. The effective SER lifetimes τ_{SER}, appeared in the term (Eq. 4.3) of the asymptotic decay, can be estimated using a log-log scale and intersection of tangents to curve's bend (Fig. 4.22b).

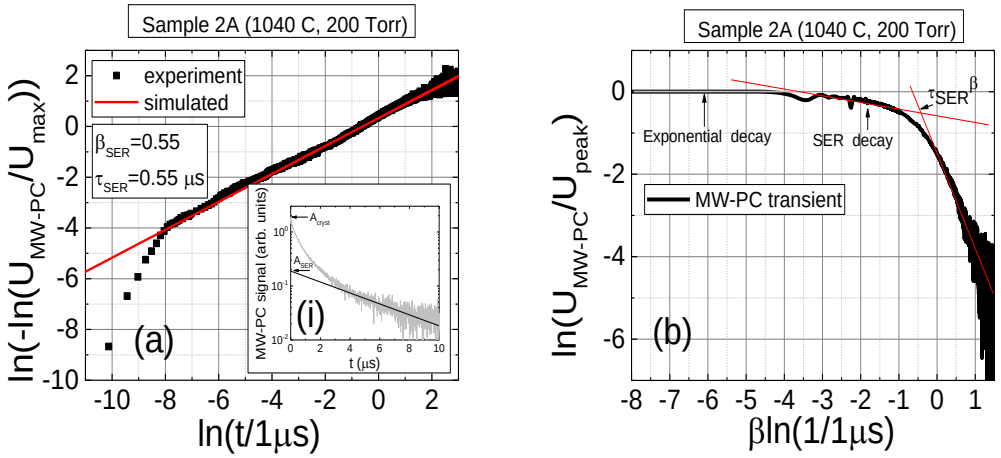

Fig. 4.22 Stretched-exponential recombination scale plots of the MW-PC transients measured on 2A (a) sample. In the inset, a plot for estimation of partial decay amplitudes is sketched. Either the approach of the intersection of tangents to curve's bend, as illustrated for the sample 2A in b, or simulated SER curves (red lines) have been employed for estimation of τ_{SER} values.

Alternatively, SER lifetimes τ_{SER} can be extracted by fitting the transient within a SER plot (red lines in Fig. 4.22a). Values of τ_{SER} and β_{SER} (Table 4.5) have showed the dependence on sample growth regimes and, consequently, on DD. The closer a β_{SER} value to unity appears, the more perfect-crystal material is. It has been obtained that β_{SER} value decreases with enhancement of the DD for both sets of samples (Fig. 4.19 and Table 4.5). Also values of SER lifetimes τ_{SER} decrease with increase of dislocation density. For rather small excitation levels, the impact of radiative recombination within MW-PC decay transients can be ignored within the first order approximation. In latter case, the entire concentration of the excess carriers n_{ex0} determines the rate and decay shape of the non-radiative recombination, while only a few tens percentage of the n_{ex0} disappear through luminescence channels. The partial amplitude, attributed to recombination within crystallites, composes about 90% of the MW-PC signal (Fig. 4.22a and Table 4.5). This indicates nearly monocrystalline GaN layer.

Table 4.5 Parameters of stretched exponential decay.

Sample No.	**Pressure/temperature**	$A_{cryst}/A_{exc\ spot}$	$A_{TD}/A_{exc\ spot}$	τ_{SER} (μs)	β_{SER}
2A	200 Torr/1040 C	0.91	0.09	0.55	0.55
2B	200 Torr/1060 C	0.89	0.11	0.50	0.49
2C	200 Torr/1080 C	0.91	0.09	0.40	0.45
1A	75 Torr/1040 C	0.89	0.11	0.20	0.47
1B	75 Torr/1060 C	0.92	0.08	0.30	0.50
1C	75 Torr/1080 C	0.89	0.11	0.60	0.64

4.2.4. Pulsed photo-ionization spectra

In order to identify the predominant point defects, PPIS measurements [108] were performed. The typical for MOCVD GaN PPI spectrum, recorded on the sample 1B, is illustrated in Fig. 4.23. The threshold photo-ionization energy values, extracted using the Lucovsky model [109], are listed in Table 4.6.

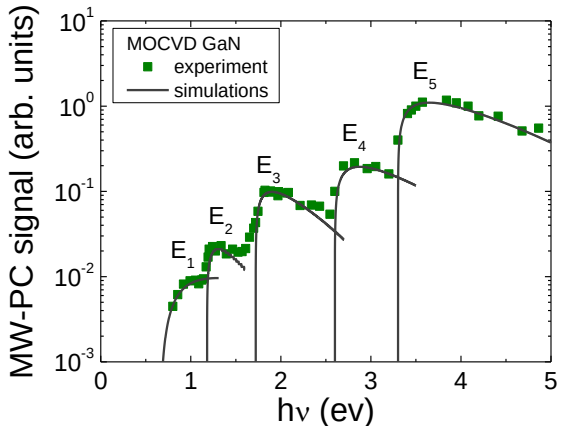

Fig. 4.23 The as-recorded (symbols) and simulated (solid lines), using Lucovsky model, PPI spectrum recorded in MOCVD GaN sample 1B.

Table 4.6 The threshold activation energy values, estimated by using Lucovsky model, and assignment of defects.

	MOCVD GaN	
	Photo-activation energy (eV)	Defect type
E_1	0.7	V_{Ga}^- [176]
E_2	1.2	N_{Ga} [177]
E_3	1.7	$V_{Ga}O_N$ [148]
E_4	2.6	C_N [148]
E_5	3.3	C_NO_N [148]

The dominant PPIS peaks have been attributed to the photo-active centres, caused by the technological defects (Table 4.6). The crystalline structure defects as anti-site (N_{Ga}), vacancy- (V_{Ga} and $V_{Ga}O_N$) and carbon-related (C_N and C_NO_N) defects have been identified.

4.2.5. SS-PL spectra and TR-PL characteristics

The SS-PL spectra (Fig. 4.24) were recorded using cw laser excitation. There, the low excitation levels, close to that employed within MW-PC experiments, were used. The intensive blue B-PL band is clearly observed in SS-PL spectra (Fig. 4.24). The intensities of UV-PL and short wavelength wing of B-PL (Fig. 4.24a) have been obtained to be nearly the same in samples grown using the same temperature but different pressures. The absolute intensities for SS-PL bands of B-PL and YG-PL are similar for different samples. More variations can be deduced for the UV peak intensity, as a clearly non-linear process relative to the excess carrier concentration. The close values of Y-G-PL

intensity obtained for different samples would indicate nearly the same concentration of DAP in these samples. The normalized SS-PL spectra (Fig. 4.24b) show the redistribution of radiative recombination flows among UV, B and YG-PL channels. There, the clearer reduction of the normalized B and YG PL intensity with increase of growth temperature can be deduced for both 75 Torr and 200 Torr regimes.

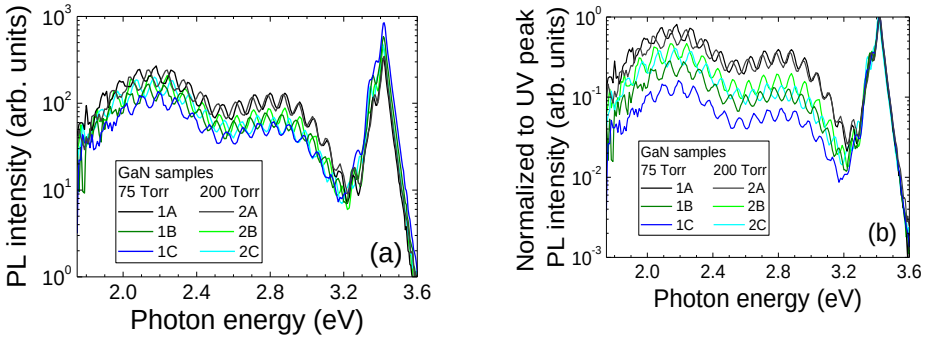

Fig. 4.24 (a) As recorded the SS-PL spectra for GaN-on-Si samples. (b) SSPL spectra with PL intensity normalized to an UV peak intensity. PL light interference determines small modulations of spectral signal [A5].

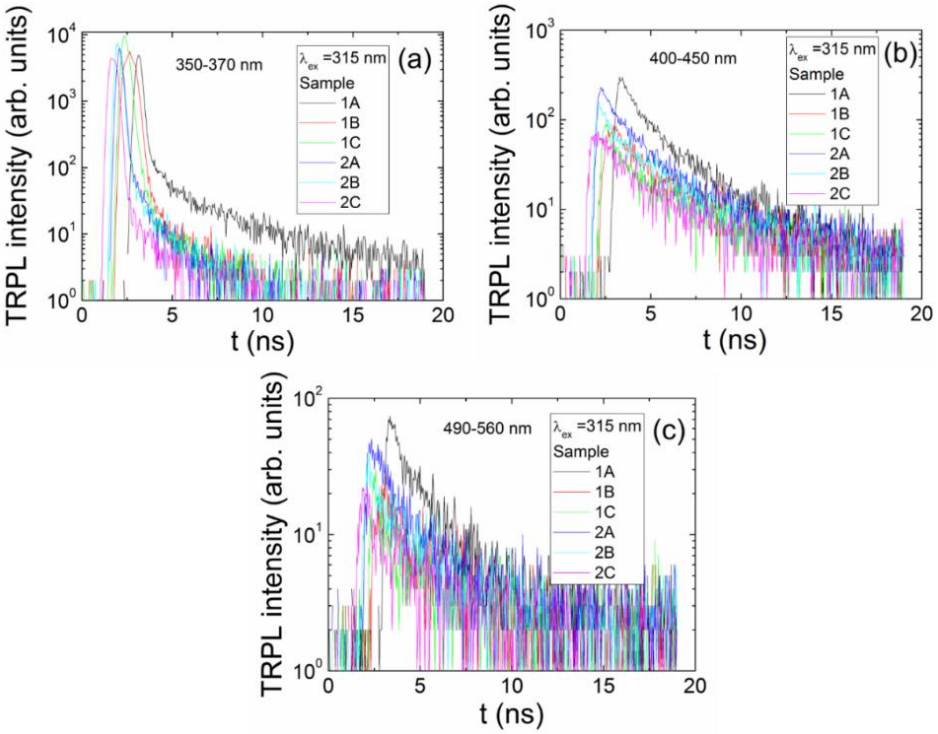

Fig. 4.25 TR-PL transients recorded for UV (a), B (b) and YG (c) PL segments in GaN/Si samples [A5].

The TR-PL transients (Fig. 4.25) have been recorded using 100 fs laser pulses, where excess carrier densities of n_{ex}~10^{18} cm^{-3} are initially generated. TR-PL transients were integrated over different PL spectral segments, denoted in plots within Fig. 4.25. The instantaneous PL decay lifetimes (Table 4.7) have been evaluated from the decay slopes by measuring the reduction of PL intensity by exp(-1). UV TR-PL transients show a two-componential decay. The characteristic time values for the UV PL initial decay ($\tau_{in,\,PL}$) have been found to be about 140−180 ps. The shorter values are estimated for 200 Torr grown layers. However, due to the high excitation level, there the non-linear PL decay character occurs and a rather small part of the excess carrier density decaying through radiative channels. Therefore, it is difficult to associate the measured instantaneous values to the excess carrier decay lifetime, within the first order approach. However, the asymptotic component ($\tau_{as,PL}$) shows rather low PL intensity. Values of $\tau_{as,PL}$ in UV TR-PL transients agree with simply evaluated τ_R parameters (Table 4.4), when using the MW-PC data.

For B-TR-PL and YG-TR-PL transients, the PL decay shapes are close to the single-exponential decays. The lower intensity of the B-PL and YG-PL bands determines to the less dynamic range and the necessity to enhance the spectral segment (50 nm for B-PL and 70 nm for YG-PL) for integration in recording of the transients by streak camera technique. Values of instantaneous PL decay lifetime for different samples, extracted from B-PL and YG-PL transients (using a slope of the PL intensity decrease by exp(-1) for the single-exponential decay) are represented in Table 4.7.

Table 4.7 Instantaneous PL decay lifetimes (ns), evaluated from the decay slopes at exp(-1) level and simulated values.

	Sample No.	UV-TR-PL τ_{inst} values		Simulated $\tau_{R,\,D\text{-}A\,PL}$ using UV-TR-PL	B-TR-PL τ_{inst} values	YG-TR-PL τ_{inst} values
		$\tau_{in,PL}$	$\tau_{as,PL}$	with B=2×10^{-8} cm^3/s	$\tau_{eff\text{-}PL}$	$\tau_{eff\text{-}PL}$
75 Torr	1A, 1040 °C	0.18	2.74-5.20	12.0	1.45	1.40
	1B, 1060 °C	0.18		4.0	1.55	2.00
	1C, 1080 °C	0.18		4.0	1.68	1.45
200 Torr	2A, 1040 °C	0.15		2.5	1.55	1.80
	2B, 1060 °C	0.15		3.0	1.68	2.00
	2C, 1080 °C	0.14		3.5	2.67	2.20

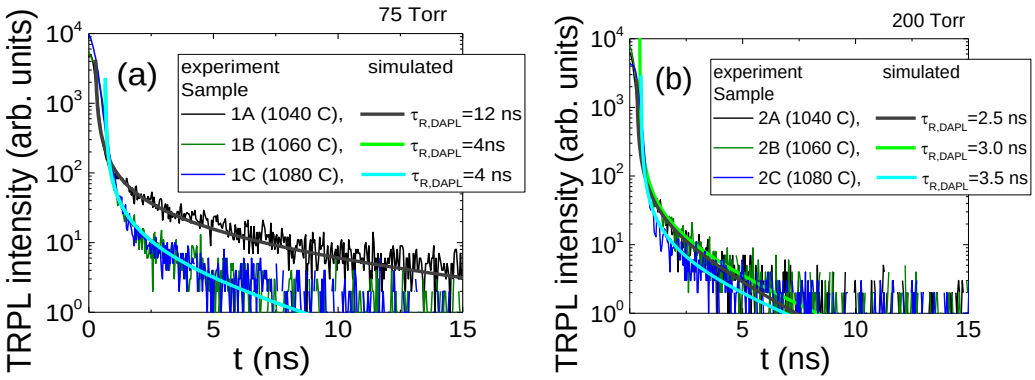

Fig. 4.26 TR-PL transients recorded for an UV segment obtained in samples grown at 75 Torr (a) and 200 Torr (b) pressure and fitted using an approach of the simultaneous non-linear and linear radiative recombination processes. The $\tau_{R,\,D\text{-}A\,PL}$ values extracted by fitting procedure are denoted in the legends.

The clearer tendency of $\tau_{eff\text{-}PL}$ increase with growth temperature can be deduced for 200 Torr grown samples. For the latter samples, the $\tau_{eff\text{-}PL}$ lifetimes are obtained to be longer than those measured for 75 Torr grown layers.

The UV-TR-PL transients have also been fitted (Fig. 4.26) using a model, designed for the non-exponential PL decay process, in which the excess carrier variation in time, $n_{ex,PL}(t)$ can be represented [108] as follows:

$$n_{ex,PL}(t) = \frac{n_{ex,0}\exp(-\dfrac{t}{\tau_{R,D-A\,PL}})}{1+Bn_{ex,0}\tau_{R,D-A\,PL}\left[1-\exp(-\dfrac{t}{\tau_{R,D-A\,PL}})\right]}. \qquad (4.4)$$

Here, B is the coefficient of radiative recombination, $\tau_{R,\,D\text{-}A\,PL}$ is the carrier lifetime ascribed to the D-A PL recombination, and $n_{ex,0}$ is the excess carrier concentration at the peak of excitation. The MW-PC signal is there proportional to the concentration of free carriers. Thereby, the parameter $n_{ex,0}$ is directly estimated using a transient taken from the experiment at fixed excitation density. The excitation density is evaluated using the laser beam parameters and the material absorption coefficient at fixed wavelength. For simulations, the value of carrier lifetime ($\tau_{R,\,D\text{-}A\,PL}$), ascribed to each transient, can also be estimated from the slope of the asymptotic ($n_{ex,0}\exp(-t/\tau_{R,\,D\text{-}A\,PL})/[1+B\tau_{R,\,D\text{-}A\,PL}\,n_{ex,0}]$) component within a recorded transient. Thereby, the value of either B or a pair of values (B, $\tau_{R,\,D\text{-}A\,PL}$) is the only adjustable parameter involved into simulation of the experimental transients (Fig. 4.26).

The most important parameter in these correlations is the $\tau_{R,\,D\text{-}A\,PL}$ which is a measure for estimation of the D-A defects within the lattice. The *B* coefficient of an estimated value of 2×10^{-8} cm^3/s has been obtained, which can be ascribed to the UV (band-to-band) recombination process. Values of $\tau_{R,\,D\text{-}A\,PL}$ have been extracted from the fitting (Eq. 4.4) of the non-exponential PL decay transients over the whole time scale, where PL signal falls down to the background level. The later phase of the PL decay is there ascribed to the quasi-linear radiative recombination through DAP. Then, the model of Eq. 4.4 can be applicable. Thus, a pair of parameters *B* and $\tau_{R,\,D\text{-}A\,PL}$ can be exploited for more precise description of the UV-TR-PL transients.

4.2.6. Lateral distribution of PL characteristics

Rather smooth surfaces of the as-grown GaN epilayers were revealed by AFM (Fig. 4.27). These pictures show the crack-free material layers. The similar peak-to-valley (PV) and RMS (root mean square) roughness values for all the samples seem to be independent of growth pressure and temperature.

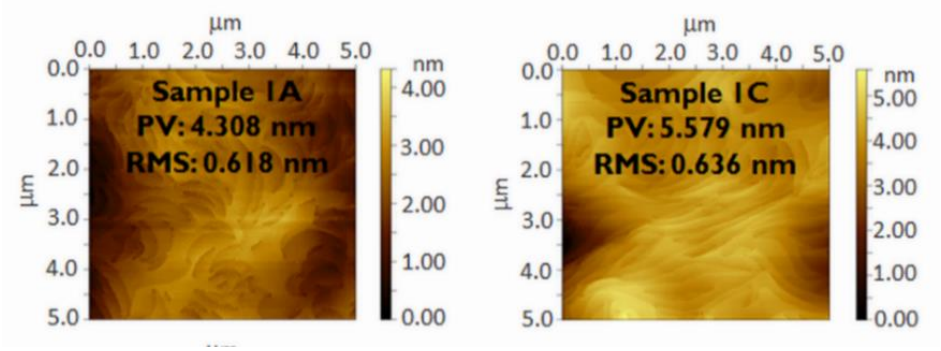

Fig. 4.27 AFM imaging indicates the crack-free epilayers with comparable PV and RMS roughness values.

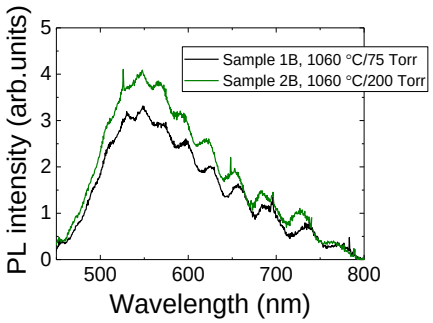

Fig. 4.28 Confocal microscopy PL spectra for scan area of 10×10 μm^2 in samples grown using the same temperature (1060 C) and different pressure.

The PL spectra integrated over small area within confocal microscope field have been also recorded under excitation by laser diode. The PL spectra for the only Y-PL band were observed at 405 nm excitation wavelength for samples grown using different pressure (Fig. 4.28). It can be observed, that YG-PL intensity is larger for the sample grown using 200 Torr pressure relatively to that obtained using 75 Torr. It is well-known [145] that YG-PL is related to D-A transitions within crystalline GaN. Thus, the larger YG-PL intensity, for 200 Torr sample relative to that for 75 Torr sample, might imply the longer carrier D-A recombination lifetime $\tau_{R,\ D\text{-}A\ PL}$ and τ_R in agreement with results shown in Fig. 4.21.

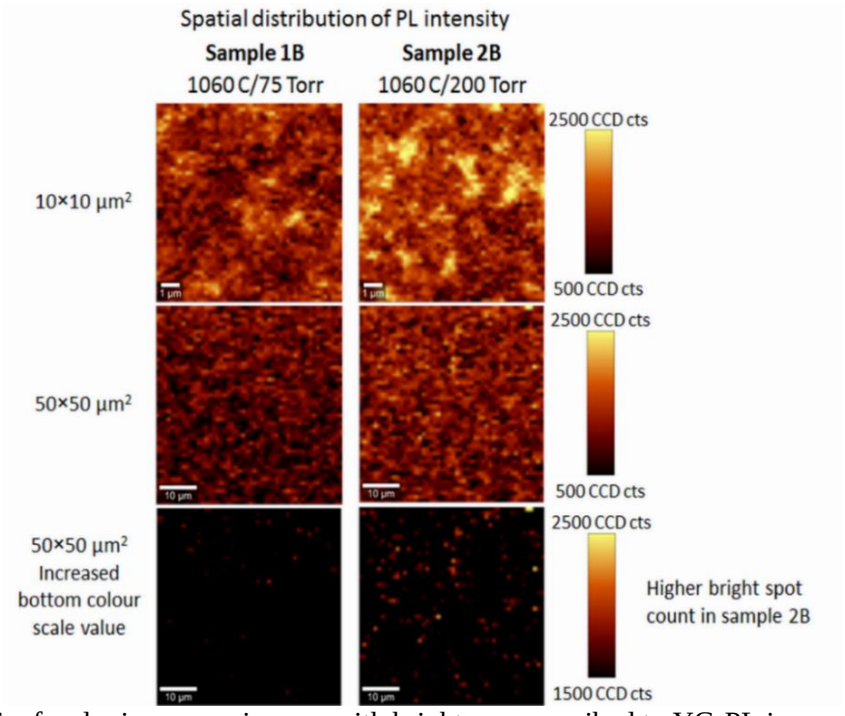

Fig. 4.29 Confocal microscopy images with bright areas ascribed to YG-PL in samples [A5].

This result can be understood assuming that small fraction of carriers decays through PL channel. The entire excess carrier density is controlled by the non-radiative recombination processes, therefore, filling of D-A PL centres competes with that for the non-radiative recombination ones. The crystallites in 200 Torr grown layers seem to be larger, as obtained from confocal microscopy images (Fig. 4.29).

4.2.7. Dislocation density dependent carrier lifetime variations

The summarized parameters (extracted simply by using the decay slope (τ_R), obtained for the initial component of the MW-PC transient, and simulated (τ_{SER}), assuming crystallite as well as random-walk carrier decay processes) are illustrated in Fig. 4.30 as a function of the density of edge dislocations (DED).

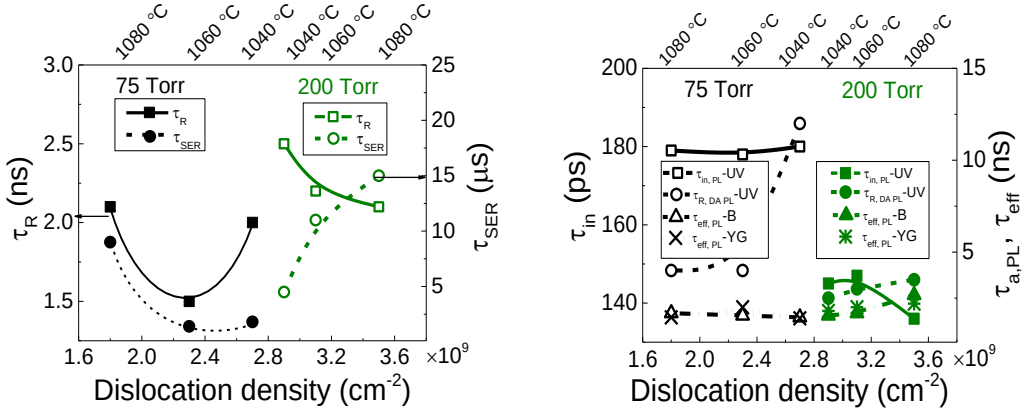

Fig. 4.30 Values of the τ_R extracted from an initial MW-PC decay slope, associated with crystallites, and the asymptotic SER decay lifetime (τ_{SER}) as a function of DED in GaN epilayers and instantaneous $\tau_{in,PL}$ of UV, B and G-Y PL decay as a function of DED.

For the lowest excitation densities, the initial stage decay component (τ_R) seems to be ascribed to recombination within crystallites, and these τ_R values decrease with enhancement of the DED. The τ_{SER} values, estimated for GaN layers grown at 75 Torr pressure, and τ_R, τ_{SER} lifetimes, for layers grown at 200 Torr pressure, clearly decrease with enhancement of the DED. For low excitation levels, fitting values for the τ_{SER} are obtained in the range of hundreds of ns. This implies that τ_{SER} values represent the carrier trapping through random-walk within dislocation nets, surrounding GaN crystallites, according to the model described by Eq. 4.3. Despite of the impact of disorder, the examined GaN layers are mainly composed of crystallites where values of the $A_{cryst}/A_{exc\ spot}$ coefficient reach 90 % (Table 4.7) for all the samples. However, values of the stretched-exponent index β_{SER} and of the stretched-exponential decay lifetime τ_{SER} clearly decrease with enhancement of TDD. The parameter β_{SER} indicates the increase of disorder degree with TDD. Reduction of τ_{SER} with increase of

TDD implies prevailing of carrier decay through dislocation cores, when TDD enhances.

For low excitation level, the asymptotic component within the MW-PC transients can be attributed to carrier trapping and anomalous diffusion through random-walk processes within inter-crystallite regions, where dislocation densities of TDD>10^8 cm^{-2} has been estimated by XRD measurements. The τ_{SER} values decrease with enhancement of edge dislocation density. The initial MW-PC decay component (τ_R) seems to be ascribed to recombination within single-crystal regions of the epilayers, and these τ_R values decrease with enhancement of DED. These τ_R lifetimes seem to be sensitive to the structure of point defects within GaN epilayers.

Variations of the phenomenological ($\tau_{in,PL}$, $\tau_{eff\text{-}PL}$) and fitting ($\tau_{R,D\text{-}A\ PL}$) parameters, extracted from TR-PL transients, as a function of DD are illustrated in Fig. 4.31. Values for the evaluated characteristic PL-decay times are nearly independent of DED, and their values vary not more than 20% when changing the growth regimes. The TR-PL transients, integrated over the UV-PL band at high excitation levels, show a two-componential decay process, which can be approximated by a non-linear recombination model. In this model. band-to-band (excitonic) annihilation ($\tau_{in,PL}$) determines the non-linearity of the process while the asymptotic component ($\tau_{R,D\text{-}A\ PL}$) can be ascribed to the DAP PL. The DAP-related PL processes exhibit effective relaxation times of tens of ns, which are close to the τ_R values within the initial stage of the MW-PC transients. The UV-PL is nearly independent of the DD. At the same time, the DAP PL intensity seems to be related to the point defects and impurities, identified by the PPIS measurements within the GaN crystallites.

Lateral variations of the τ_R and $\tau_{as,PL,UV} \approx \tau_{R,D\text{-}A}$ PL values are in qualitative agreement with confocal microscopy images, obtained for the same samples. There, the YG-PL lateral distribution is manifested within the area of the confocal microscopy image.

It should be concluded that the role of carrier radiative and non-radiative recombination as well as of trapping effects in MOCVD GaN layers containing a rather high density of different types of dislocations significantly depends on the excitation level. This is important in designing of devices based on GaN-on-Si materials and in the choice of the characterization techniques as well as the interpretation of measurement results. Also, high densities of dislocations and their clusters lead to manifestation of disorder effects at rather small excess carrier concentrations.

4.3. Evolution of spectral characteristics in GaN-based sensors during irradiations

The multi-quantum-well-(MQW)-based GaN structures grown by MOCVD technology were investigated in order to trace the evolution of radiation damage. The proton-induced luminescence (PI-L) and the BELIV (barrier evaluation by linearly increasing voltage) transients were simultaneously recorded during exposure to the 1.6 MeV proton beam (Sketch of the experimental setup for these measurements is shown in Fig. 3.4 b). The dominant radiation defects have been *ex situ* examined by the deep-level transient spectroscopy (DLTS). This method is described in section 3.3.1.

4.3.1. LED-based particle sensor

The 1 μm thick InGaN/GaN metal-heterostructure-metal sensors, with multi-quantum–well (MQW) layer, made of commercial light emitting diodes (LEDs, Optosupply OSB4XNE1E1E [178]) were investigated. The multilayer heterostructures of 0.25 μm thickness and 1×10^{-2} cm^2 area were fabricated on sapphire substrates by MOCVD technology.

4.3.2. BELIV characteristics of pristine sensors

The BELIV measurements were applied for the characterization of the barrier capacitance and for the estimation of carrier traps within a device material. The BELIV transients were examined varying temperature from 25 to 70 °C and using reverse (U_R) polarity linearly increasing voltage (LIV) pulses

(Fig. 4.). There, BELIV transients were recorded using fixed reverse voltage (U_R) pulses with a peak value of U_P=8 V and pulse duration of τ_P=50 μs.

The initial current peak within a BELIV transient corresponds to the barrier capacitance value C_{b0}, which is dependent on the effective doping concentration ~$N_{eff}^{1/2}$ [179]. As shown in the inset of Fig. 4.31, the amplitude of this peak increases linearly with enhancement of temperature. This implies the increase of the effective doping $N_{eff}=N_D \pm N_T$ due to trap ionization, where N_D is the donor concentration and N_T is the concentration of the net space charge, produced by ionized traps [180]. The N_{eff}, as determined from BELIV measurements at room temperature, is $N_{eff}=3.5\times10^{17}$ cm^{-3}.

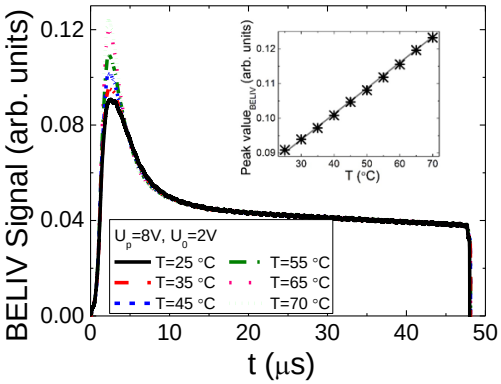

Fig. 4.31 Temperature-dependent variations of BELIV current transients. In the inset: Peak value of BELIV transient as a function of temperature.

4.3.3. Variations of characteristics during proton irradiation

Owing to the GaN sensor availability to record both the electrical and optical signals, the impact of the radiation defects introduced by a proton beam was studied at room temperature by combining the *in situ* measurements of the BELIV (Fig. 4.32) and proton-induced luminescence (PI-L) (Fig. 4.32) characteristics.

The fluence-dependent peak values of the BELIV current (Fig. 4.32) indicate the decrease of the barrier capacitance C_{b0} with enhancement of irradiation fluence. This result indicates that radiation-induced defects partially compensate the dopants introduced by LED fabrication. At the highest irradiation fluence (Φ=6×10^{15} cm^{-2}), the BELIV signal decreases by a factor of 3, compared to its value in the pristine sensor. The BELIV signal in sensor

irradiated with the highest fluence acquires a square-wave shape, which is typical for the fully-depleted sensor. In that case, the geometrical capacitance determines the BELIV transient. This result implies that the heterojunction sensor under heavy irradiation approaches to the capacitor-like device. The observed decrease of the peak values of BELIV current indicates the changes of the effective doping concentration from $N_{eff}=3.5\times10^{17}$ cm^{-3}, for a pristine sensor, to $N_{eff}=2.4\times10^{17}$ cm^{-3}, for the sensor irradiated with the highest fluence.

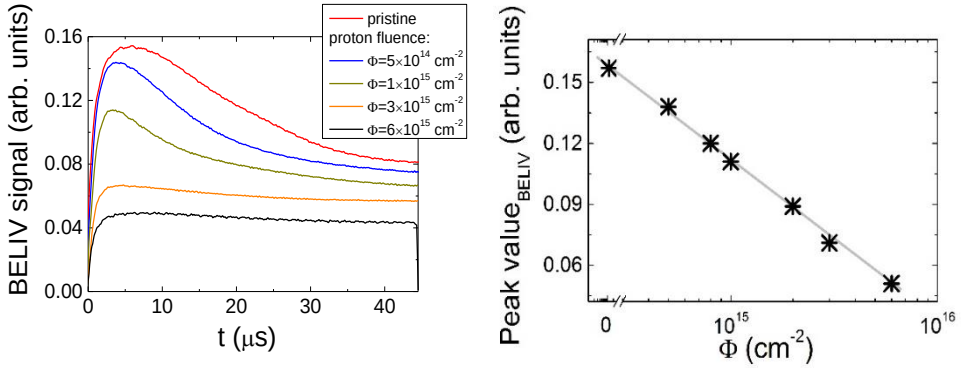

Fig. 4.32 Fluence-dependent barrier charging current (a) and its peak value (b) measured during irradiation at room temperature.

The PI-L spectra (Fig. 4.33) consist of four bands: (i) UV spectral band (UV-L) of rather small intensity; (ii) violet (V-PI-L) with maximum at 420 nm (2.9 eV); (iii) B-PI-L with maximum at around 465 nm (2.7 eV); (iv) YG-PI-L) luminescence band with a peak at 550 nm (2.3 eV). Variations of the peak intensity for two the most intensive PI-L bands are shown in Fig. 4.33.

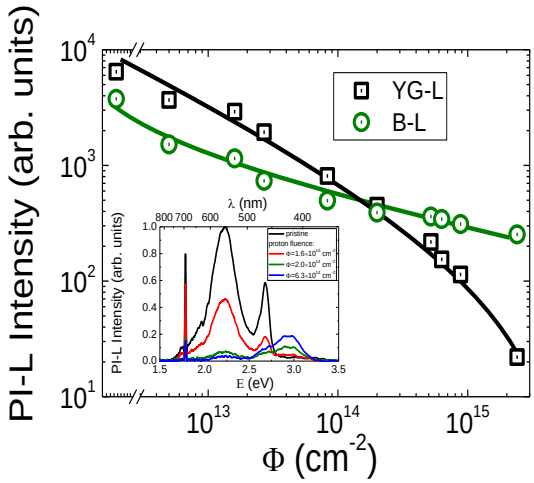

Fig. 4.33 Variations of the PI-L peak-intensities for B and YG spectral bands as a function of proton irradiation fluence. The evolution of the PI-L spectra is illustrated in the inset.

The broad YG-PI-L emission band suffers a fast luminescence quenching during irradiation. The YG-PI-L band is likely to be attributed to either the $V_{Ga}O_N$ complex [146,147] or to the carbon-related defects C_N and C_NO_N [147,148]. The intensity of the B-PL band with maximum at 465 nm decreases with fluence increase. This B-PI-L band might be ascribed to the transitions of carriers within DAP [145]. The intensity of the V-PI-L band increases with irradiation fluence and becomes dominant at the fluences of $\Phi > 5\times10^{14}$ cm^{-2}. This band can emerge due to the formation of vacancies ascribed to radiation defects in the electron-blocking AlGaN layer of GaN LEDs [181]. The additional R-PI-L peak at 700 nm appears in the highly irradiated sensor, which is related to the proton beam excited luminescence in the sapphire substrate, due to Cr-ascribed centres [182].

4.3.4. CV characteristics and DLTS spectra

CV measurements allow for the estimation of the shallow dopant concentration N_s and their distribution in the space charge region. Two slopes, typical for the heterostucture-based LED's, can be deduced from the C^{-2}-V characteristics (Fig. 4.34). The turning-point within CV's indicates a full-depletion voltage for the less doped layer. The effective doping concentration evaluated from CV characteristics are estimated to be $N_{eff}=4\times10^{17}$ cm^{-3} for the pristine sensor and $N_{eff}=2.2\times10^{17}$ cm^{-3} for the sensor irradiated with the highest fluence. These values are in rather good agreement with N_{eff} values extracted from the BELIV measurement. The dopant removal is the main radiation-damage effect in semiconductor radiation-detectors. Variations of capacitance for the heavily irradiated sensor do not exceed 10 % of the average value being of the same magnitude with measurement errors. This result implies a weak dependence of capacitance on reverse voltage in heavily irradiated sensor. It has also been deduced from CV's (Fig. 4.34) that values of barrier capacitance in a sensor, irradiated with a proton fluence of 6×10^{15} cm^{-2}, is decreased by a factor of 3.6 compared to its value in the pristine sensor, due to the decrease of the effective dopant concentration ($N_{eff}=N_D-N_A$).

The C-DLTS spectra recorded for the pristine and the irradiated sensor are illustrated in Fig. 4.35. These DLTS measurements were performed over a temperature range of 10−400 K using filling pulse of 1.5 V voltage and of 500 ms duration. The reverse bias voltage was varied in the range of 1–10 V, which corresponds to the scan depths in the range of 80–140 nm.

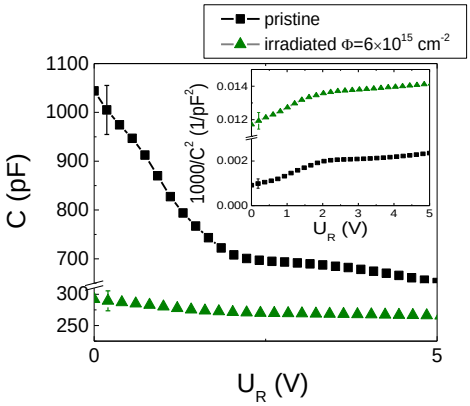

Fig. 4.34 CV characteristics obtained for the pristine GaN sensor and for that irradiated with the proton fluence of 6×10^{15} cm^{-2}. C^{-2}-V plots are shown in the inset [A7].

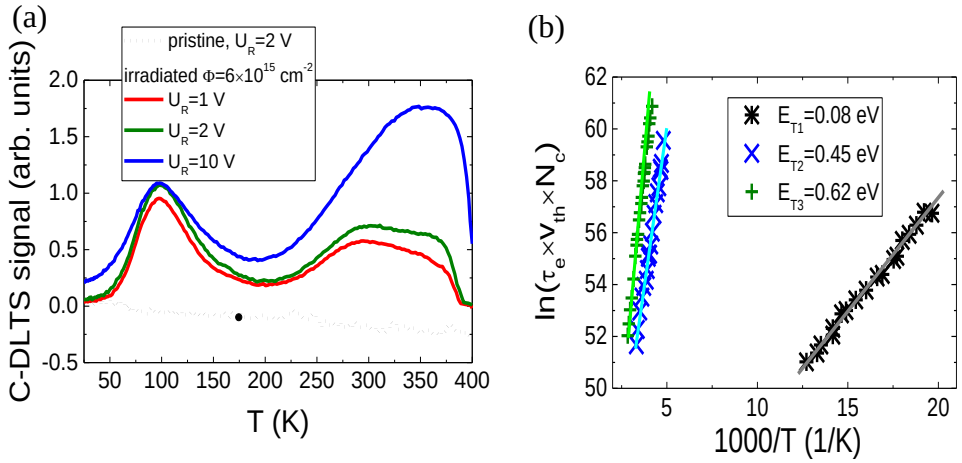

Fig. 4.35 C-DLTS spectra recorded on the pristine sensor and sensor irradiated with proton fluence of 6×10^{15} cm^{-2} (a) and the Arrhenius plots obtained for spectral peaks recorded on the sensor irradiated with proton fluence of 6×10^{15} cm^{-2} (b) [A7].

The post-irradiation DLTS measurements on sensors was performed by comparing these spectra with that obtained before irradiations. The DLTS signals on the noise level have only been detected for the pristine sensor (Fig. 4.35). While, a spectral structure containing broad peaks has been observed for the irradiated sensors. The radiation defect concentration varied near-linearly with irradiation fluence for the examined Φ range. It has been obtained that the amplitude of a spectral peak E_{T1} at 100 K is independent of the reverse-bias

voltage U_R. This result implies a nearly-homogeneous distribution of the radiation-defects within the depletion region. The broad DLTS spectral band, covering the temperature range of 250−350 K, clearly indicates the overlapping of two spectral peaks, at least.

The amplitude of the E_{T2} and E_{T3} peaks increases with enhancement of the reverse-bias voltage. This points to a non-uniform distribution of concentration of the radiation-defects (E_{T2}, E_{T3}) within the deeper regions of heterostructure materials, far from the interface layer. The Arrhenius plots have been displayed by using PhysTech software [103]. The Arrhenius plots (Fig. 4.35) have been determined using the relevant shifts of the peak positions over the temperature scale, dependent on the rate-window and on the correlation function.

Values of the thermal-activation energy E_T, of trap concentration N_T and of their capture cross-section σ, extracted from analysis of the Arrhenius plots, are listed in Table 4.8.

Table 4.8 Parameters of traps for sensor irradiated with a proton fluence of 6×10^{15} cm^{-2}, evaluated using Arrhenius plots.

Level	E_C-E_T (eV)	N_T (cm^{-3})	σ (cm^2)
E_{T1}	0.08	2.6×10^{15}	2×10^{-18}
E_{T2}	0.45	2×10^{15}	6×10^{-16}
E_{T3}	0.62	1.8×10^{15}	2×10^{-13}

The traps, characterized by sets of the (E_T, N_T, σ) parameters have been attributed to the radiation-induced defects, as follows: i) the traps with activation energy of E_{T1}=0.08 eV are ascribed to the nitrogen vacancy V_N [183]; ii) the deep levels with E_{T2}=0.45 eV are associated with radiation-defect complexes of rather shallow donors [181,182]; iii) the centres characterized by the E_{T3}=0.62 eV are attributed to the still unidentified defect, which has also been observed by other authors [183,184].

The potential for the application of GaN-based sensors by detecting both the electrical and optical signals in a harsh radiation environment has also been demonstrated. Detection of both the electrical and optical signals also may be applicable for characterization of high electron mobility transistors (HEMT) [185–187].

5. Investigation of diamond structures

5.1. Native defects in HPHT and CVD diamond materials

The electron spin resonance (ESR), Fourier transform-infrared spectroscopy (FTIR) and pulsed photo-ionization spectroscopy (PPIS) measurements have been combined to identify the dominant defects in diamond samples, grown by chemical vapour deposition (CVD) and high pressure-high temperature (HPHT) methods.

5.1.1. HPHT and CVD synthesized diamond samples

The HPHT diamond single crystals were synthesized by the high pressure (4.5−5.0 GPa) and high (1350−1450 °C) temperature gradient technology [188] using the Ni-Fe-C liquid solvent/catalyst carbon metallurgy system. The solvent/catalyst system comprised the 70% Fe and 30% Ni metals in crystal growth cell, respectively. Growth regime was controlled by measurements of electrical power consumption, which was correlated with temperature by additional calibration measurements with precision of ±15 °C. The as-grown single crystal had a cube-octahedral morphology (Fig. 5.1a). The octahedral growth planes prevail on the as-grown crystal, while a cube growth sectors can be observed on the crystal-top plane, situated oppositely to a seed. The cube growth sectors on the side-planes of a crystal are not clearly observable. The as-grown crystal contains a crack, which is marked by a dashed line in Fig. 5.1a. A scheme of wafer sample slicing is presented in Fig. 5.1a. The samples from No. 3 to No. 9 were prepared by slicing of the crystal into wafers across the plane (001) in parallel to the crystal base. The mechanically polished wafers contain surface roughness less than 20 nm, as measured by an AFM. The crystallographic and shape parameters of the investigated HPHT diamond samples are denoted in Fig. 5.1b.

Single-crystal wafer samples of CVD diamond, with dimensions of 3×3 mm^2 and thickness of 300 μm and 500 μm, were purchased from industrial diamond producer Element Six [189]. The single-crystal (100) oriented CVD diamond contained impurities of boron (B) and nitrogen (N) of concentrations

<1 ppb and <5 ppb, respectively. This small concentration of impurities caused the ESR signal intensity below the limit of detection. Also, no frequencies for the IR-active defects modes have been resolved in FTIR spectra. However, PPIS allowed identifying of the defects in CVD diamond samples.

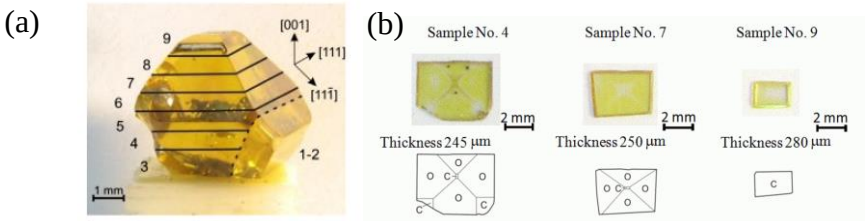

Fig. 5.1 The pictures of the HPHT diamond crystal wafer samples, prepared by slicing of the single crystal (a) and polishing both wafer surfaces are shown in the top row (b). The cubic (C) and octahedral (O) growth sectors on each wafer are denoted in the lower row.

5.1.2. Spectral characteristics of technological defects

The P1 and W8 centres [190,191], ascribed to the substitutional N and the substitutional negatively charged Ni impurities, respectively, have been identified by the ESR measurements in HPHT diamond samples. The ESR resonances associated with N defect have been observed at room temperature (Fig. 5.2), while the peak associated with Ni impurities is present only at low temperatures (100 K). At low temperatures, the ESR resonance signals, ascribed to P1 centres, are as usually saturated. Nitrogen concentration, ranged from 1.2×10^{19} cm^{-3} to 2.4×10^{19} cm^{-3}, has been estimated for HPHT diamond samples. The Ni concentration has been evaluated to be 1.9×10^{17} cm^{-3}, 1.4×10^{17} cm^{-3} and 5.4×10^{16} cm^{-3} for the samples No. 4, No. 7, and No. 9, respectively.

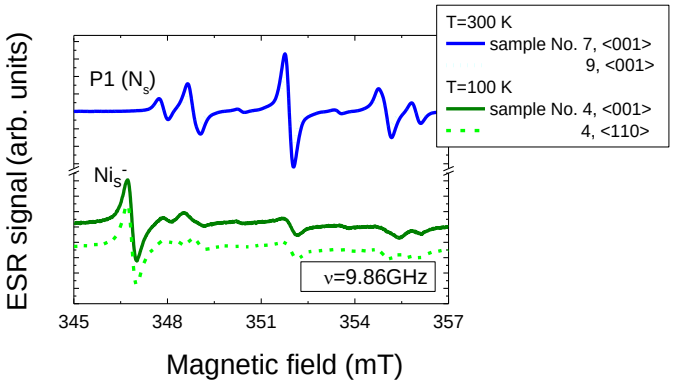

Fig. 5.2 The ESR spectra recorded at room temperature and at 100K temperature in HPHT diamond samples, containing nitrogen and nickel impurities.

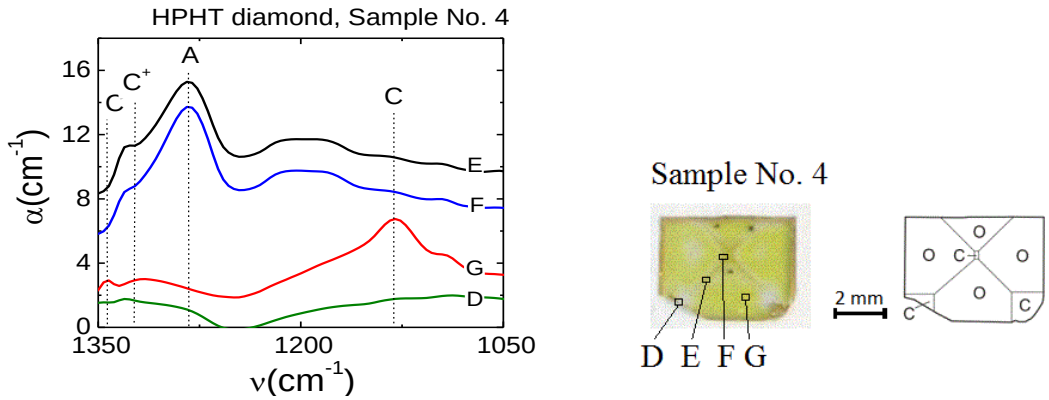

Fig. 5.3 Spectra of absorption coefficient measured by FTIR technique at different locations of HPHT diamond sample No. 4.

In order to investigate the distribution of the technological defects, the spectra of the absorption coefficient have been measured at different locations on sample No. 4. (Fig. 5.3). These locations represent different crystal morphology sectors.

Table 5.1 Concentration of the identified impurities in HPHT diamond wafer samples.

Defect type	Technique	Sample No.4			Sample No.7	Sample No.9
		Defect concentration $\times 10^{18}$ cm^{-3}				
P1 (N)	ESR	24			22	12
P_{Ni}	ESR	0.19			0.14	0.054
		Location on the sample				
		D	F	G	Central area	Central area
C	FTIR	-	-	22	3.6	9.1
A	FTIR	-	23	-	37.0	11.0
C^+	FTIR	-	3	1	1.4	-

The typical spectra have been ascribed to different scanned location points (to cubic morphology sector (D), to a boundary of two octahedral sectors (E), to the intersection line of the octahedral and cubic sectors nearby the centre of the sample (F), and to the octahedral sector (G)). The peaks in spectra have been identified as the neutral C (1130 cm^{-1}) and the charged C^+ (1332 cm^{-1}) isolated substitutional nitrogen centres and the A aggregate (1282 cm^{-1}) being a pair of the nearest neighbour substitutional nitrogen atoms. For the D-point, located at the edge of wafer, the non-luminescent region is inherent. There, concentration of impurities has been evaluated to be below the FTIR detection limit. The peaks related to the A and C^+ defects have been usually observed in the octahedral sectors (E and F location). The C-type neutral isolated substitutional nitrogen

defects revealed to be dominant in the non-luminescent octahedral morphology areas at G-point. Concentration of the identified impurities, evaluated using ESR and FTIR spectral data, are listed in Table 5.1.

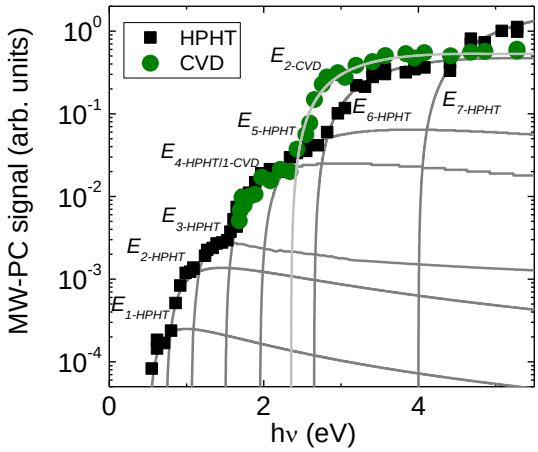

Fig. 5.4 The PPIS spectra obtained on HPHT and CVD diamond samples. Solid lines represent the fitted spectral steps.

Table 5.2 The photo-activation energy values, extracted by using Lucovsky's model, and assignment of defects.

HPHT diamond		CVD diamond	
Photo-activation energy (eV)	Defect type	Photo-activation energy (eV)	Defect type
$E_{1\text{-}HPHT}$=0.52	a-C [192]	$E_{1\text{-}CVD}$=1.5	a-C [192]
$E_{2\text{-}HPHT}$ =0.74	a-C [192]	$E_{2\text{-}CVD}$=2.37	N subst. [193]
$E_{3\text{-}HPHT}$ =1.1	a-C [192]		
$E_{4\text{-}HPHT}$ =1.5	a-C [192]		
$E_{5\text{-}HPHT}$ =1.97	N-V [61]		
$E_{6\text{-}HPHT}$ =2.67	N-VNiV-N[193]		
$E_{7\text{-}HPHT}$ =4.00	Ni, N2-VNi-N2 [193]		

The PPIS spectra for CVD and HPHT diamond samples are illustrated in Fig. 5.4. Values of the photo-activation energy (Table 5.2), have been extracted for different spectral steps (Fig. 5.4) using simulations by Lucovsky's model [109], and allow the identification of the native defects in diamond materials. The shallower levels, with photo-activation energy below 1.5 eV, have been ascribed to a-C defect. An N substitutional type defect with the photo-activation energy of $E_{2\text{-}CVD}$=2.37 eV, has been identified in CVD diamond. A nitrogen-vacancy complexes, with activation energies of $E_{5\text{-}HPHT}$ =1.97 eV and of $E_{6\text{-}HPHT}$ =2.67 eV, and the nickel-related deep levels with activation energy of

$E_{7\text{-}HPHT}$ =4.0 eV, respectively, have been identified for HPHT diamond. The nitrogen is present as an un-avoidable impurity in synthetic diamond while the Ni impurities are commonly incorporated within HPHT diamond, synthesised using a Ni-containing alloy catalyst-solvent, as discussed in section 2.1.2.

5.2. Profiling of diamond sensor signals

5.2.1. Samples and structure of capacitor type sensors

The single-pixel capacitor-type detectors were formed by using HPHT and CVD grown diamond materials and different metallization types in fabrication of electrodes. The pressed-plate type copper electrodes, compatible with micro-strip line formed on printed circuit board (PCB), or two-component silver (Ag paste) and copper (Cu) metallization were employed to fabricate the parallel-plate capacitor-type sensor structures with blocking electrodes (Fig. 5.5). These structures with different type electrodes were examined to clarify the impact of diamond surface states and the role of carrier traps in appearance of the dynamic polarization effect.

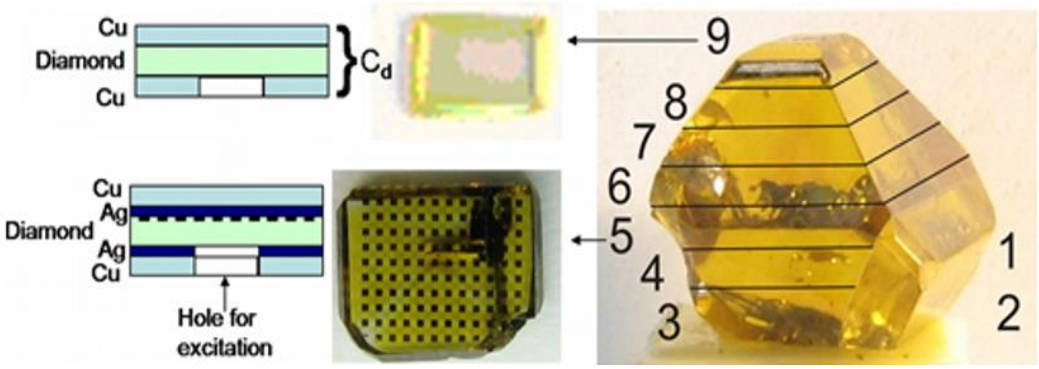

Fig. 5.5 The sketch of the capacitor type sensors made of diamond wafers covered by metallic electrodes and the micro-pixel contacts (sample No. 5).

A mosaic electrode system has been made on the sample No. 5 (Fig. 5.5) of the HPHT wafer set, which contains a rather large concentration of metallic inclusions. The thickness of this wafer sample was d=748 μm. Isle (micro-pixel) type electrodes of dimensions of 200×200 μm^2 were produced by implantation of boron (B). The linear current-voltage dependence for each single micro-pixel has been obtained for applied voltages of up to a few hundred volts over all the set of micro-pixels within the wafer planar surface, while the dark current values

varied in the range from a few fA to a pA. These variations have been ascribed to the lateral distribution of impurities spread within the bulk of this wafer [9], where current variations correlate well with carrier lifetime lateral maps on the wafer surface. Then, the pressed copper electrodes or two-layer metal electrodes (Fig. 5.5) were applied to form a parallel-plate capacitor type sensor on this (No. 5) HPHT diamond sample.

Capacitor type structures on HPHT wafer samples No. 4, No. 7 and No. 9 (Fig. 5.5) using pressed plate electrodes were also made for comparison.

Single-crystal wafer samples of CVD diamond (described in section 5.1) were also involved into measurements. The pressed plate copper electrodes (Fig. 5.5) used in the formation of capacitor type CVD diamond structures were exploited to provide the same experimental conditions as those employed for investigations of HPHT diamond structures. The detailed description of the setup used for TCT measurements can be found in section 3.3.

5.2.2. Models for analysis of drift-diffusion dynamics

Models, based on Shockley-Ramo's theorem [194,195], describing the evolution of ICDC transients have been developed. The Shockley-Ramo's theorem allows a calculation of the induced charge for sandwich structure detectors. The charge Q and current i induced on an electrode by a moving charge q is expressed as:

$$Q = q\varphi(x)$$
$$i = qvE_0(x), \quad (5.1)$$

where $\varphi(x)$, $E_0(x)$ is weighting potential and weighting electric field at the charges position (x), respectively, and v is the instantaneous velocity of charge drift. Moreover, on assuming that the signal is read out from the anode, the weighting potential of this electrode is calculated using the Shockley-Ramo theorem by setting the potential on the anode to 1, and assuming the cathode to be grounded. In the simple case, the weighting potential for planar detector (Fig. 5.6a) is a linear function of depth between electrodes (Fig. 5.6b). However, the calculation of the weighting potential could be very complex in a non-isotropic medium [196]. In the illustrated example, the incident γ radiation

generates n_0 electrons and p_0 holes at a distance Z from the cathode. The number of generated electron-hole pairs is proportional to the deposited energy. The induced charge is dependent on the distance (*dx*) the charges move before they reach the corresponding electrode, the cathode for holes and anode for electrons, respectively, and can be written as:

$$dq = \frac{q_0 dx}{d}. \tag{5.2}$$

The induced charge consists of a two components that is determined by electrons *(n)* drifted a distance *x* and holes *(p)* drifted a distance *(d-x)*. The assumption that no charge is lost due to recombination and trapping gives expression of the induced charge on the cathode $(Q_{cathode})$ and (Q_{anode}):

$$Q_{cathode} = Q_{anode} = n\left(\frac{x}{d}\right) + p\left(\frac{d-x}{d}\right). \tag{5.3}$$

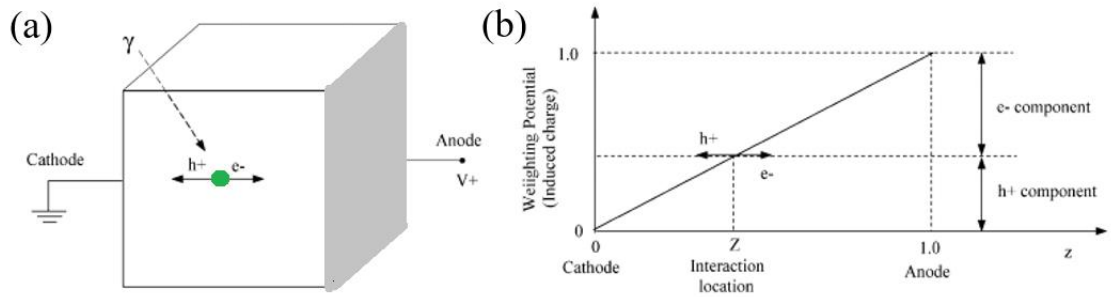

Fig. 5.6 The scheme of a semiconductor detector with planar electrodes (a). The weighting potential of the anode, and signal components arising from the movements of charges (b) [196].

The change of charge on the cathode is converted to a voltage pulse using a charge sensing amplifier and the amplitude of the output signal is proportional to the deposited energy.

The original Shockley-Ramo theorem leads to the deduction that the charge on electrodes induced by a moving charge *q* is independent of applied potentials on electrodes and the space charge. However, the fundamental problem is the charge *q* trapping in the space charge region. The trapping causes the reduction of signal amplitude that depends on the drift length of charge carriers. The drift-diffusion approach is commonly employed to simulate a current transient. However, drift-diffusion model is limited by small charge drift when electric field changes can be ignored. Theoretical analysis of the radiation damage and carrier trapping/emission caused electric field changes is still lacking. Therefore,

dynamic models based on Shockley-Ramo's theorem, under injection of the localized surface domains and of bulk charge carriers have been developed in this work. The transients in capacitor type diamond sensors using dynamic model have been examined.

The electron-hole neutral domain is initially injected in most cases of carrier excitation either as the secondary carrier pairs, generated by high energy particles, or the photo-excited carrier pairs. The electric field acting on drifting electron and hole sub-domains is determined by solving the Poisson's equation including the charge on electrodes, induced by an external voltage source, and the charge induced by the moving charge sub-domains. The current transient detected on a load resistance within external loop of circuit is then varied in time due to charge changes on electrode caused by drift of the injected domain drift, where the external source should balance variations of charge on electrode [194]. Instantaneous current values are then determined by the charge variations in time (integrated over an area of electrode) related to the characteristic transit time.

Simplified sketches of the processes and the formation regimes for current pulses are illustrated in Fig. 5.7–Fig. 5.10. In Fig. 5.7, the energy and charge distributions are sketched for sensor biasing (a), for the phase of the monopolar charge drift (b), and for the polarization charge formation (c). The polarization charge formation is illustrated under both the excess carrier trapping to deep centres (quasi-stationary polarization) and formation of the depletion (from one type of excess carriers) region at electrodes (dynamic polarization) after drifting excess carriers arrive to electrodes. Sketches of the evolution of the light injected bulk charge distribution and of the dynamic polarization are illustrated in Fig. 5.8. In Fig. 5.9, a sketch of separation and drift of the locally injected sheet of carriers under switched-on external voltage of value, capable to separate excess carrier pairs, is shown. In Fig. 5.10, sketches of the diffusion current formation under large amount of the light injected carrier pairs in the bulk of material within inter-electrode gap are illustrated.

The transit time for the drift prevailing processes is evaluated by solving the equation for the instantaneous drift velocity normalized to the whole drift

region length. It had been shown [197] that there are a variety of regimes (Fig. 5.7–Fig. 5.10) such as pure bipolar and mixed (bipolar-proceeded by the monopolar) drift processes and drift proceeded by diffusion. The role of diffusion can be ignored if an injected charge does not exceed the charge on electrode induced by the external voltage source (Fig. 5.8 and Fig. 5.9). On the contrary, the injected charge surface domain is able to screen the electric field caused by a fixed value of the bias voltage if the external voltage is low and the surface density of the injected charge is large (Fig. 5.10). This regime is ascribed to the diffusion limited convection current, namely the current transient appears as a result of the time varied charge, diffused to and collected on electrode.

5.2.3. Models of drift current for injected bulk domain at low applied voltages

The current transients can be caused by the time varied bulk excess charge domain, overwhelming the inter-electrode space, which disappears due to diffusion to and collection of charge on electrode (Fig. 5.8 and Fig. 5.10). This happens if applied external field is insufficient to separate the electron-hole sub-domains over the entire bulk. Then, the carrier reservoir is located within the inter-electrode gap, and the diffusion supplied carriers replace those extracted to electrode.

The charge of non-extracted carrier surface sub-domain screens the external field (Fig. 5.8), and, thus, determines a characteristic length of charged layer. The same charged layer appears at the opposite electrode. These opposite charged layers determine an additional electric field, equivalent to Dember field for ambipolar diffusion. This Dember-like field also prevents diffusion of the non-extracted carriers to electrodes at the opposite sides (Fig. 5.8). The analytical description of current transients, induced by a bulk electron-hole domain, which cannot be disassembled owing to the applied external electric field, can only be performed using several approximations. The drift-diffusion process consists of two components: the initial stage of carrier extraction through carrier drift and the later current flow stage, sustained by diffusion supplied excess carriers from the electrically neutral bulk.

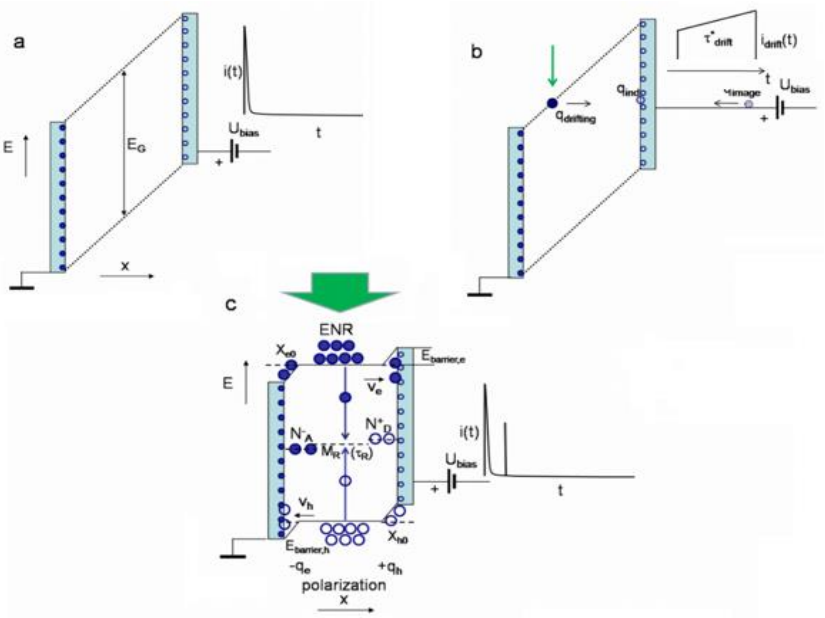

Fig. 5.7 Sketches of the changes of the induced charges and of energy band diagram (E) within a capacitor structure. a - Charges (hollow circles − positive, solid circles − negative charges) induced on electrodes just after switching-on of the DC external voltage. On the right, a current transient of charging of the capacitor sensor is sketched; b - Sketch of the monopolar drift phase for the light injected charge and formation of drift current pulse. Here, the induced charge on electrode and external current (image charge) during drift are also sketched; c - Sketch of the polarization charge ($-q_e, q_h$) formation under both the excess carrier trapping onto deep centres (quasi-stationary polarization) and formation of the (X_{e0}, X_{h0}) depletion (from one type of excess carriers) regions at electrodes (dynamic polarization) after drifting (v_e, v_h) excess carriers arrive to electrodes. In the electrically neutral region (ENR), recombination (τ_R) through centres M_R is possible, while charged centres (N^-_A, N^+_D) can appear due to carrier trapping. On the right, a current transient of charging (the photo-capacitance effect) of the capacitor sensor [A1].

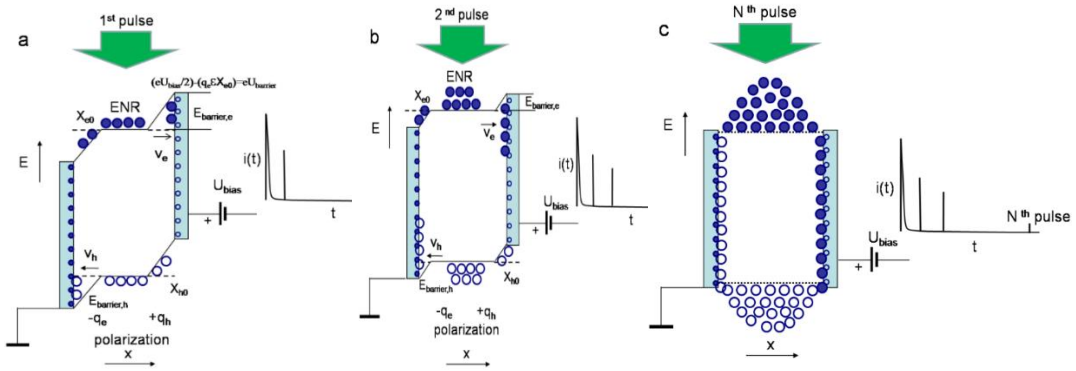

Fig. 5.8 Sketches of evolution of the light injected charges (large circles) under switched-on external voltage of rather small value and of the dynamic polarization through accumulation of the space charge under a set of light pulses (1st-a, 2nd-b, and N-th-c) those inject bulk density of excess carrier pairs. X_{e0} and X_{h0} − the dynamic depletion widths. The diagrams of the capacitor charging currents (vertical lines) are there shown on the right [A1].

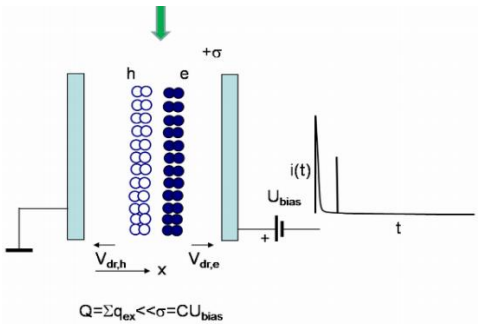

Fig. 5.9 Sketch of separation and drift of the light locally injected charges (of rather small amount) under switched-on external voltage of value capable to separate excess carrier pairs. This sketch illustrates the drift prevailing processes at moderate and high applied voltages. The main notifications and assumptions are the same as for Fig. 5.7 [A1].

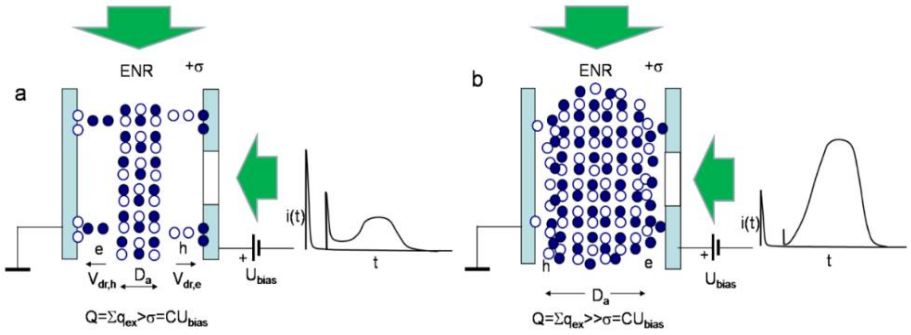

Fig. 5.10 Sketches of diffusion current formation under large amount of the light injected carrier pairs, when the external field ascribed to the injected carriers appears. a - Formation of the partial dynamic depletion layers, separated by ENR (filled with non-separated excess carriers) which supplies diffusing carriers from ENR (for drift within near-electrode regions), during formation of a current pulse under the light injected bulk charge. On the right, a diagram of capacitor charging, of drift current and the pulses of diffusion component are shown; b - Sketch of the diffusion prevailing current pulse under bulk injection of the large amount of the excess carrier pairs which charge is capable to completely screen the external field. Notifications and assumptions are the same as for Fig. 5.7 [A1].

The initial stage of a current pulse is described by the scalar representation of the acting electric field within a half of inter-electrode gap ($0 \le x \le d/2$) under a surface charge ($\sigma/2$) (sketched by small circles in Fig. 5.7) induced by a fixed external voltage ($U/2$) and by excess electron concentration n_0, as:

$$E(x) = -\frac{1}{\varepsilon\varepsilon_0}\left(\frac{\sigma}{2} + en_0 x\right) . \qquad (5.4)$$

Here, symmetry, based on charge conservation at electrodes, enables to consider a half of a system. Therefore, half of σ, U and d are taken into account. By taking the second Poisson integral:

$$-\frac{U}{2} = \int_{d/2}^{d/2-X_e} E(x)dx \quad , \qquad (5.5)$$

the surface charge σ is related to U, n_0, and to an instantaneous position X_e for the extraction of electrons, which density n_0 is equal to that p_0 of the homogeneously in-depth injected holes, as:

$$\sigma = en_0 d - \frac{\varepsilon\varepsilon_0}{X_e} U - en_0 X_e \quad . \tag{5.6}$$

Extraction of electrons persists till the charge σ on electrode is screened. An evolution of energy diagrams under a sequence of excitation pulses in a capacitor sensor biased by a relatively low voltage is sketched in Fig. 5.8, where injected excess carriers are shown by large circles. This condition $\sigma = 0$ determines a quadratic equation for evaluation of the depletion depth $x = X_{e0}$. A negative root of Eq. 5.6 with $\sigma = 0$ leads to:

$$X_{e0}(n_0, U) = \frac{d}{2}\left(1 - \sqrt{1 - \frac{\varepsilon\varepsilon_0 U}{en_0\left(d/2\right)^2}}\right) \approx \frac{d}{2}\left(\frac{\varepsilon\varepsilon_0 (U/2)}{en_0\left(d/2\right)^2}\right) \quad . \tag{5.7}$$

The last approximation in Eq. 5.7 is possible if $X_{e0} << d/2$, at rather low voltages. In Eq. 5.6, a pole for $X_e \equiv 0$ appears if a diffusive outspread is ignored. This pole can also be circumvented by assuming a δ-thick skin-layer on metallic electrode (with initial coordinate X_e-$\delta = 0$ and $\delta \rightarrow 0$, as in depletion approximation [198]). However, the rate of the current rise is always limited by an external circuit. Therefore, the infinity condition never appears in experimental situations. Eq. 5.7 implies that the approximation of the bulk injected domain is relevant when an external field $U/d << en_0(d/2)/\varepsilon\varepsilon_0$ is weak relative to that created by a surface charge at a cross-sectional planes (at boundaries of the ENR centred at $d/2$, Fig. 5.8). This also means that the inequalities $\delta < X_{e0} < d/2$ are held.

The current variation in time during the initial stage of pulse ($i_1(t)$) is then obtained (by differentiating in time the surface charge σ integrated over an area S of the electrode) as:

$$i_1(t) = S\frac{d\sigma}{dt} = \frac{S}{X_e(t)}\left(\frac{\varepsilon\varepsilon_0 U}{X_e(t)} - en_0 X_e(t)\right)\frac{dX_e(t)}{dt} \quad . \tag{5.8}$$

Thus, to obtain the expression for the $i_1(t)$ function, the time dependent variations of the instantaneous positions ($X_e(t)$) of the extracted charge of surface density en_0X_e and the drift velocity $dX_e(t)/dt$ should be described. These

dependencies are obtained by solving the kinetic equation for drift of carriers. For instance, the electron drift velocity can be represented by:

$$\frac{dX_e}{dt} = -\mu_e E(n_0, U, X_e) = -\mu_e \frac{1}{2\varepsilon\varepsilon_0}\left(\frac{\varepsilon\varepsilon_0}{X_e}U - en_0(d + X_e)\right). \quad (5.9)$$

The last expression for acting electric field is obtained by inserting σ calibrated to U (Eq. 5.6 into Eq. 5.4). As a current is determined by the changes in time of charge on electrode, the dimensionless instantaneous position $\psi = X_e/d$ is then essential. Thus, Eq. 5.9 is rearranged as:

$$\frac{d\psi}{dt} = \frac{1}{2}\left(\frac{1}{\tau_{Mn0}}(1+\psi) - \frac{1}{\tau_{TOF}}\frac{1}{\psi}\right). \quad (5.10)$$

By integrating Eq. 5.10, the re-arranged expression of function $\psi(t)$ is obtained for the range of $0 \le \psi' \le \psi$ and $0 \le t' \le t$. Here, the characteristic time of dielectric relaxation is denoted as $\tau_{Mn0} = \varepsilon_0\varepsilon/en_0\mu_e$, and a dimensionless depth of depletion is $\psi_{e0} = X_{e0}/d$. The expression of the transit time τ_{tr} is obtained by integrating Eq. 5.10 for the range of $0 \le \psi' \le \psi_{e0}$ and $0 \le t' \le \tau_{tr}$. These integrals are obtained as:

$$\int_0^{\psi_{e0}} \frac{\psi' d\psi'}{\psi'^2 + \psi' - \frac{\tau_{Mn0}}{\tau_{TOF}}} = \frac{1}{2\tau_{Mn0}} \int_0^{\tau_{tr}} dt' \quad . \quad (5.11)$$

The solutions of Eq. 5.11 can be expressed through the roots of the denominator function as:

$$\psi_{\pm} = \frac{-1 \pm \sqrt{1 + 4\frac{\tau_{Mn0}}{\tau_{TOF}}}}{2}, \quad (5.12)$$

which obeys the transcendental equation:

$$\psi(t) = \psi_+\left[1 - \left(\frac{\psi(t) + \psi_-}{\psi_-}\right)^{-\frac{\psi_-}{\psi_+}} \exp\left(\frac{t}{2\tau_{Mn0}}\left(\frac{\psi_-}{\psi_+} + 1\right)\right)\right]. \quad (5.13)$$

Finally, by inserting Eq.5.10 with solutions of the Eq. 5.13 into Eq. 5.8, the initial stage of current pulse is expressed for the time interval $0 \le t \le \tau_{tr}$ as:

$$i_1(t) = \frac{S\varepsilon\varepsilon_0}{\psi(t)d}U\frac{1}{2\tau_{Mn0}}\left[\frac{1}{\psi(t)} - \frac{\tau_{TOF}}{\tau_{Mn0}}\psi(t)\right] \times \left[1 + \psi(t) - \frac{\tau_{Mn0}}{\tau_{TOF}}\frac{1}{\psi(t)}\right]. \quad (5.14)$$

An identical solution should be obtained by analysis of the hole extraction at the opposite electrode due to correlated, bipolar drift of electrons and holes

(Fig. 5.7–Fig. 5.9). The correlated drift ($\tau_{tr,e} \equiv \tau_{tr,h} = \tau_b$) determines the charge conservation in the system. Possible inequality of carrier mobilities is self-adjusted by different depletion lengths $X_{e0} \neq X_{h0}$. The shift of a peak within the depth distribution profile of excess carrier concentration occurs (like in the case of ambipolar diffusion with different velocities of surface recombination [199,200], and a peak is shifted towards a surface of the slower surface recombination). Thereby, the induced current (on the opposite electrode), due to extraction and drift of holes, can be considered as a displacement current (not an additional current) which completes a circuit. A capacitor type detector with an injected bulk domain of excess carriers really acts as a junction type, partially depleted detector. There the merged electrically neutral regions and a spatially separated junction contact appear (where electrodes play the role of the junction which separates excess carriers). It would be worth to note that recombination of excess carriers within regions nearby the electrodes (of width X_{e0}, X_{h0}) is suppressed by a lack of the recombination counter-partners, – as one type of the excess carriers is extracted to electrode by external electric field.

Further evolution of the induced current, by including even the transitional layer between the depleted and neutral regions, can be iterated using methodology presented by Eqs. 5.5–5.14. However, this leads to the extremely complicated transcendental equations. Therefore, to simplify analytical consideration for the case of large density of excess carrier pairs shown by large circles in Fig. 5.8c and Fig. 5.10, the scaling ($\tau_{tr} << \tau_D$) of the characteristic times of drift τ_{tr} and of ambipolar (with a coefficient D_a) diffusion $\tau_D \cong d_{eff}^2/4\pi^2 D_a$ (where $d_{eff}=d-X_{e0}-X_{h0}$) can be employed (Fig. 5.10). There, the initial, short stage of the current pulse evolution is described by $i_1(t)$ (Eq. 5.14). The slow further stage (Fig. 5.10) of the current pulse evolution is governed by τ_D during which the excess carriers are supplied by diffusion to the depleted layer X_{e0}. There, an assumption of the infinite surface recombination velocity is acceptable, as rapid drift ($\tau_{tr} << \tau_D$) keeps $n_0 \approx 0$ in the depleted near-electrode region. This is equivalent to a boundary condition $n_0 = 0$ for d_{eff}, equivalent to an infinite surface recombination. Using this assumption, the diffusion governed component $i_2(t)$

of the induced current can be estimated by the time varied surface charge on electrode due to varied in time excess carrier concentration $n_0(t)$ (in Eq. 5.6) as:

$$i_2(t-\tau_{tr}) = S\frac{d\sigma}{dt} \cong S\frac{\partial[en_0(t-\tau_{tr})(d-X_{e0}-X_{h0})-\frac{\varepsilon\varepsilon_0}{X_{e0}}U]}{\partial t} = eSd_{eff}\frac{\partial n_0(t-\tau_{tr})}{\partial t} \quad (5.15)$$

Solutions for the time varied concentration of excess carriers, averaged over d_{eff}, are well-known (e.g., [201]) from theory of parabolic equations (with boundary conditions, $n_0|_{x=0;\, x=deff} = 0$). These solutions for a single-dimensional approach are expressed as:

$$< n_0(t-\tau_{tr}) >|_{d_{eff}} = n_0(t=0)\sum_{k=0}^{\infty}\frac{8}{\pi^2}(-1)^k\frac{\exp\left(-\frac{4D_a\pi^2}{d_{eff}^2}(2k+1)^2(t-\tau_{tr})\right)}{(2k+1)^2}. \quad (5.16)$$

As carriers are supplied to X_{e0} by diffusion, the sign within the exponential term of Eq. 5.16 should be replaced by the opposite one, i.e., concentration supplied by diffusion during partial diffusion times $\tau_{D,k}=d_{eff}^2/4D_a\pi^2(2k+1)^2$ changes in time. By differentiating Eq. 5.16, the current component $i_2(t-\tau_{tr})$ with $t = t-\tau_{tr}$ is then re-written as:

$$i_2(t_2) = eSd_{eff}n_0(t=0)\sum_{k=0}^{\infty}\left(\frac{8}{\pi^2}(-1)^k\frac{\exp\left(\frac{4D_a\pi^2}{d_{eff}^2}(2k+1)^2t_2\right)}{(2k+1)^2}\frac{1}{\tau_{D,k}}\right). \quad (5.17)$$

Thereby the entire current evolution within a transient is described by Eqs. 5.14 and 5.17 as:

$$i(t) = \begin{cases} i_1(t)|_{0\le t\le\tau_{tr}} \\ i_2(t-\tau_{tr})|_{t>\tau_{tr}} \end{cases}. \quad (5.18)$$

Taking the carrier recombination τ_R within electrically neutral range into account, the additional current components should be introduced as:

$$i(t)_{+\tau_R} = \begin{cases} i_1(t)|_{0\le t\le\tau_{tr}} - eS\frac{\partial(n_0e^{-\frac{t}{\tau_R}})}{\partial t}X_e(t) \\ i_2(t-\tau_{tr})|_{t_2>\tau_{tr}} + eSd_{eff}n_0(t=0)e^{-\frac{t_2}{\tau_R}}\sum_{k=0}^{\infty}\left(\frac{8}{\pi^2}(-1)^k\frac{\exp\left(\frac{4D_a\pi^2}{d_{eff}^2}(2k+1)^2t_2\right)}{(2k+1)^2}[\frac{1}{\tau_{D,k}}-\frac{1}{\tau_R}]\right) \end{cases}. \quad (5.19)$$

The derived simplified approach describes well the qualitative experimental observations [202]: (i) at large densities of injected carriers (even for the localized initial domain) profiling of current transients by varying applied voltage leads to prevailing amplitude of the second component i_2 attributed to diffusion (as the externally introduced charge on electrodes is screened by the injected excess charge, Fig. 5.10); (ii) both drifts components are observable at moderate densities of excess carriers within the injected bulk domain (Fig. 5.8c and Fig. 5.10) and at relatively low applied voltages, while the initial current i_1 component prevails due to $1/\psi(t)$ for $\psi(t)<<\psi_{e0}(t)$ (Eq. 5.14); (iii) both components can also be observable (Fig. 5.9 and Fig. 5.10) for the perpendicular injection regime (for the excitation laser beam relative to field direction [203]) if an outspreading excitation beam overwhelms the entire inter-electrode gap; (iv) in voltage dependent profiling of transients, both components overlap when threshold value of the applied voltage is sufficient to separate the electron and hole sub-domains over the entire inter-electrode gap.

5.2.4. Models for injection of a localized domain

For the injection of a localized electron (q_e)-hole (q_h) domain, the relation between the surface charge ($+\sigma$) on the high potential electrode and the external voltage U is obtained by taking the second Poisson integral. The solution for a scalar surface charge σ depends on the instantaneous positions ($\psi_e(t)$ and $\psi_h(t)$) of the drifting e-h sub-domains (Fig. 5.9) within an inter-electrode gap of length d. The detailed consideration of the currents induced by the injected carrier capture and drift in capacitor and junction type sensors is presented in [197,204]. There it had been shown that induced instantaneous current values depend on the injected charge amount and on transit time, which is consequently determined by the characteristic times of dielectric relaxation $\tau_{Mq,e,h,}=\varepsilon_0\varepsilon d/q_{e,h}\mu_{e,h}$ and of free flight $\tau_{TOF,e,h}= d^2/U\mu_{e,h}$ of the sub-domains of injected carriers with mobilities $\mu_{e,h}$. Thereby an instantaneous velocity and the transit time depend on the amount of injected charge ($q_{e,h}$). Also, current depends on time variations of the instantaneous positions of sub-domains ($\psi_{e,h}(t)$). The latter $\psi_{e,h}(t)$

dependence is significant when the injected charge can be captured by defects. Then, the expression for current variations in time for the carrier capture processes is represented as:

$$i(t)=\frac{d\sigma}{dt}S=[-\frac{\partial q_e(t)}{\partial t}(1-\psi_e(t))-q_h(t)\frac{d\psi_h(t)}{dt}-\frac{\partial q_h(t)}{\partial t}\psi_h(t)-q_h(t)\frac{\partial\psi_h(t)}{\partial t}]S \quad . (5.20)$$

For the mixed regime, containing stages of the bipolar and monopolar drift, the initial velocity of holes (electrons) should be evaluated and the re-calibration of charge on the electrodes should be performed as described in [197], to satisfy the conservation of charge and charge momentum (qv). This gives a coincidence of $v_{0,h,mon}$ and $v_{\sum bip}\big|_{\psi h}{}^{*0}$ values at position $\psi_h{}^{*0}$ of the hole domain. The generalized expression for current, attributed to the bipolar drift prolonged by the monopolar drift of holes, is represented as:

$$i(t)=\begin{cases} i_1=\dfrac{qS}{\tau_{tr,e}}[\psi_0\exp(-\dfrac{t}{\tau_{tr,e}})+(1-\psi_0)], \quad \text{for} \quad 0\le t\le\tau_{tr,e}=\tau_{bC}; \\ i_2=\dfrac{q_hS}{\tau_{Mq,h}}\exp(\dfrac{t}{\tau_{Mq,h}})[\dfrac{v_{0,\Sigma bip}}{d}\tau_{Mq,h}+\dfrac{\tau_{Mq,h}}{\tau_{TOF,h}}-1], \quad \text{for} \quad 0\le t\le\tau_{tr,h}\equiv\tau_{tr,h,mon} \end{cases} .(5.21)$$

The duration of the entire pulse (t_P) is obtained as a sum of the bipolar drift τ_{bC} and the hole domain drift $\tau_{dr,h,mon}$, as $t_P=\tau_{bC}+\tau_{dr,h,mon}$. Similar solutions are obtained for electron prolonged drift for the mixed bipolar-proceeded by electron monopolar drift process. In the case of small charge drift, only an approximate analytical description of the process is possible, and the more rigorous consideration can be performed by including the retardation and magnetic field effects [205–207].

In the case of pure bipolar drift, a drift velocity appears to be invariable due to $\psi_{e,h}(t)\sim t$. This leads to a square-wave shape of the current pulse. The real evolution (the rise to peak) of the current should be considered by including the external circuit parameters, to account for the CUD (C_d) capacitance charging process. The current decreases after the initial peak for the mixed drift regime, due to the drag (of a late arrived sub-domain) by the counter-partner sub-domain. The phase of the monopolar drift only contains the increasing (if $\tau_{TOF,h}=\tau_{Mq,h}$) or nearly constant (if $\tau_{TOF,h}<\tau_{Mq,h}$) component of velocity. Thereby the double peak current pulse can be inherent for the mixed (a bipolar changed by a monopolar)

drift regime. These drift prevailing regimes of current pulse formation are inherent for injection of sharply localized domains and even for bulk domains, overwhelming the entire inter-electrode gap at sufficiently large voltages, capable of separating the initially neutral domain into the electron-hole sub-domains. In the latter case, the model of drifting (of localized charge sheet, − lateral surface charge plane) charge sub-domains can be acceptable, if the time of carrier grouping (increase of local carrier concentration) is shorter than the transit time of the drifting sub-domain.

5.2.5. Effects of the excess carrier photo-generation, recombination and surface charging

In this work, the excitation quanta of less energy (E_{ph} = 3.50 eV and 2.33 eV) than the forbidden energy-gap in diamond (E_G = 5.47 eV) were used. Thereby, the excess carrier domains can be generated either by non-linear absorption or via photo-ionization of filled deep traps. Therefore, for separation of prevailing mechanisms of photo-excitation, it is important to clarify whether the monopolar or bipolar (as carrier pair) initial generation is implemented. The non-linear absorption processes of two-photon via virtual states or two-step absorption through empty deep levels are most probable processes. It had been shown [9] that both two-photon and two-step processes compete in generation of excess carrier pairs in defect-rich HPHT diamond samples at elevated excitation intensities. It was revealed that photo-ionization of filled deep traps can be performed by 2.33 eV quanta in defect-rich HPHT diamond samples [9]. This leads to a nearly linear dependence of the optical transmission signal on excitation intensity. The carrier pair generation has been implied from these measurements where electrons are generated from donor type deep traps while holes appear in valence band through rapid capture of electrons from valence band to the photo-emptied traps of large density.

Optical transmission of the d thick wafer sample can be described by a function:

$$\frac{I_0}{I_{tr}} = \left(\frac{\alpha + [\beta + \beta_s] P_{ex}}{\alpha} \right) \times \exp(\alpha d) \times \left(1 - \frac{[\beta + \beta_s] P_{ex}}{\alpha + [\beta + \beta_s] P_{ex}} \times \exp(-\alpha d) \right) \qquad (5.22)$$

of the excitation power density P_{ex} and of the coefficients of the linear absorption α, of the two-photon absorption β and of the two-step absorption β_S if all the mentioned photo-excitation processes appear simultaneously. In spectral range of sample transparency (for $\alpha d << 1$ and $\alpha d < (\beta+\beta_S)P_{ex}d$), this expression can be simplified as:

$$\frac{I_0}{I_{tr}} - 1 \approx (\beta + \beta_S) P_{ex} d \,. \tag{5.23}$$

Then, carrier excitation rate is related to the absorption and laser pulse parameters as:

$$n_0 \approx [\alpha + (\beta + \beta_S) P_{ex}] I_0 \,. \tag{5.24}$$

The concentration generated at the end of a laser pulse τ_L (in the case of fast recombination $\tau_L \leq \tau_R$) is evaluated by the convolution integral averaged over laser pulse duration τ_L and expressed as:

$$n_0(t = t' - \tau_L = 0) \approx \frac{1}{\tau_L} \int_0^{t'} n_0 \exp\left(-\frac{(\Theta - \tau_L)^2}{b\tau_L^2}\right) \exp\left(-\frac{t' - \Theta}{\tau_R}\right) d\Theta \,. \tag{5.22}$$

Here, b is the dimensionless parameter characterizing a temporal width of Gaussian laser pulse. It has been obtained that $n_0(t=0)$ varies as a function of excitation intensity I_0: for HPHT samples, as $n_0(t=0) \sim I_0$ for the range of a threshold I_0 values, sufficient to detect current transients. While it becomes $n_0(t=0) \sim I_0^2$ for HPHT sensors at elevated excitation intensities. For the CVD diamond samples, the $n_0(t=0) \sim I_0^2$ characteristic prevails over the entire range where current transient signals can be detected. This implies a higher CVD crystal quality also confirmed by the significantly longer carrier lifetimes in this material relative to the tested HPHT diamond samples. On the other hand, the concentration of the electrically active defects, attributed to the residual metals and Ni in the HPHT diamond material [9], exceeds that of CVD diamond [189] by more than four orders of magnitude. Additionally, owing to the longer carrier lifetime in CVD diamond, the peak amplitude of the initial component of the current pulse has been examined as a function of excitation intensity keeping a fixed value U of the applied voltage to capacitor type detector (Fig. 5.11). As

can be deduced from Eq. 5.7 and Eq. 5.14, the $i_{1,peak}$ is proportional to $\sim(S\varepsilon\varepsilon_0 U/2d\psi)\tau_{Mn0}^{-1} \approx (S\varepsilon\varepsilon_0 U/2X_{e0})\tau_{Mn0}^{-1} = (e\mu_e SU/X_{e0})n_0$ and $X_{e0}\sim n_0^{-1}$, *i.e.*, $i_{1,peak} \sim n_0^2$.

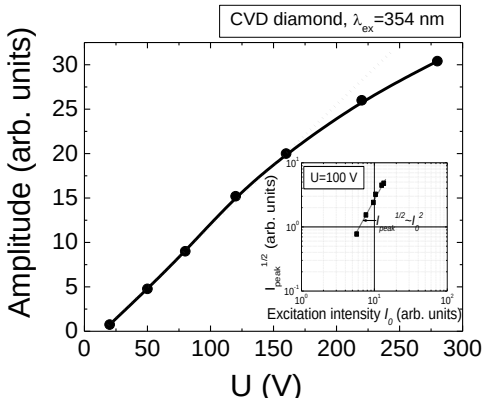

Fig. 5.11 The current peak amplitude as a function of applied voltage for the fixed excitation intensity. Both characteristics were measured for CVD diamond by using injection of bulk domain with UV excitation wavelength λ_{ex}=354 nm. The current peak amplitude as a function of excitation intensity at fixed value of applied voltage are shown in the inset.

The measured dependence of $i_{1,\,peak}$ on excitation intensity (for capacitor type CVD diamond detector with injected bulk domain) is presented in the inset of Fig. 5.11. This dependence corroborates $n_0(t=0)\sim I_0^2$, i.e., the excess carrier generation through the two-photon absorption dominates in CVD diamond.

The signal dependence on applied voltage for the fixed excitation intensity can be considered as a linear function (Fig. 5.11) over a wide range of voltages. This can be explained by a relation $i_{1,peak}\sim(S\varepsilon\varepsilon_0 U/2X_{e0})\tau_{Mn0}^{-1}\sim U$. However, the change of the current enhancement slope with applied voltage within $i_{1,peak}\sim f(U)$ characteristic can be observed in Fig. 5.11, at the highest voltages exploited. This effect of $i_{1,peak}\sim f(U)$ slope change (similar to a current saturation effect) can be explained by competition of voltage dependent changes of $i_{1,peak} \sim U/X_{e0}$ (Eqs. 5.8 and 5.9) and of $X_{e0}\sim U$ (Eq. 5.7). This effect is also similar to a change of an IV characteristic going from partial depletion regime to that of above full depletion voltage regime, within junction structures. Thereby, the saturation effect is determined by the significant separation of the injected sub-domains by the external voltage caused electric field.

Capacitance charging current transients have been complementarity measured by applying the linearly increasing voltage (LIV) pulse together with

the synchronized laser pulses (400 ps duration, 352 nm wavelength). The comparison of capacitance charging current transients measured in CVD and HPHT diamond sensors as well as LIV and synchronization pulses is presented in Fig. 5.12a.

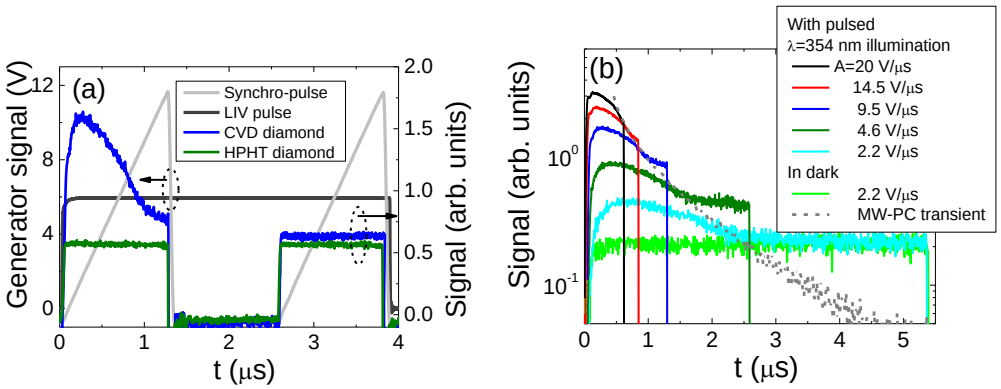

Fig. 5.12 LIV pulses and the capacitance charging current transients in HPHT and CVD diamond samples measured under pulsed laser illumination (a). Capacitance charging current transients measured in CVD diamond with pulsed laser illumination and in dark at different ramps of the LIV pulses (b). The MW-PC transient is also shown in figure (b)[A3].

Current transients of the capacitance charging by the LIV pulse, recorded in dark, show the square-wave responses for both CVD and HPHT diamond structures, indicating the rather perfect blocking electrodes. The square-wave response pulse under bias of the triangle-shape LIV pulse is obtained due to complete compensation of the linear discharge of the capacitor under test by the linear increase of the LIV biasing. The current $i(t)$ within the vertex of the square-wave response pulse can be expressed as a change in time t of the charge $Q(t)$ on the electrode: $i(t)=dQ(t)/dt=d(CU(t))/dt=d(CAt)/dt=CA=const$. Here, $A=U_{peak}/\tau_{LIV}$ is the ramp of LIV pulse with peak voltage (U_{peak}) and pulse duration (τ_{LIV}). Any injection from the electrodes would change the charge within the inter-electrode gap and the capacitance of the device. Alternatively, this would generate a convection current component of $i_{conv}(t)=(\Delta\rho d/S)\times U_{LIV}(t)\neq$const, due to a change of resistivity $\Delta\rho$ in the capacitor medium with d the length of inter-electrode gap and area of electrodes S. For instance, the change within the vertex of the response pulse can be observed if the spreading current increases with voltage due to an injecting point-like electrode [23].

The pulsed light injection of carriers of rather large density within the bulk of the inter-electrode gap, as performed in these experiments, would generate a convection current if the carrier lifetime is not too short. In the range of rather low LIV peak voltages (≤ 12 V available with the used LIV generator), the charge of the light injected carriers would screen the charge on the electrodes supplied by LIV and the excess carrier diffusion transporting charge to the electrodes would be collected. The transient of the collected charge represents then a Gaussian profile. Such a profile is acquired for transients recorded on CVD diamond devices (Fig. 5.12a). Temporal width (τ_D) of this charge collection pulse can be employed for estimation of the coefficient D_a of carrier ambipolar diffusion by using equation: $\tau_D = d^2/4D_a$. Using the parameters of the CVD diamond device, a value of $D_a = 80 \pm 10$ cm^2/s has been obtained. The accuracy of this estimation is limited by the excess carrier recombination lifetime. A rear slope of the BELIV transient is sufficiently modified by the recombinative carrier decay. These final phases of charge collection BELIV transients correlate well with the MW-PC transient (Fig. 5.12b), which is completely determined by carrier recombination, as recorded in the CVD diamond device. The carrier lifetime in the range of $\tau_R \approx 2-5$ ns was obtained for HPHT diamond material, while these lifetimes were considerably longer ($\tau_R \geq 110$ ns) for CVD diamond, as obtained from MW-PC measurements. The very short carrier lifetime in HPHT diamond is the main reason of invisibility of the BELIV response under carrier photo-injection for LIV pulses of $\tau_{LIV} \geq 1$ μs in this material device. For the CVD diamond device, the amplitude of the BELIV response increases with shortening of τ_{LIV} pulse due to increased ramp (A), as can be deduced from Fig. 5.12b. Consequently, the observable charge collection pulse is also shortened when the ratio τ_{LIV} / τ_D becomes less than unity. For the rather long LIV pulses applied, with $\tau_{LIV} >> \tau_R$, the vertex of the BELIV response is restored to the capacitor inherent (square-wave) shape, if recombination suppresses most of the photo-generated carriers. Then, no

injection ascribed signal is observed within the second pulse in the sequence of LIV pulses (Fig. 5.12a).

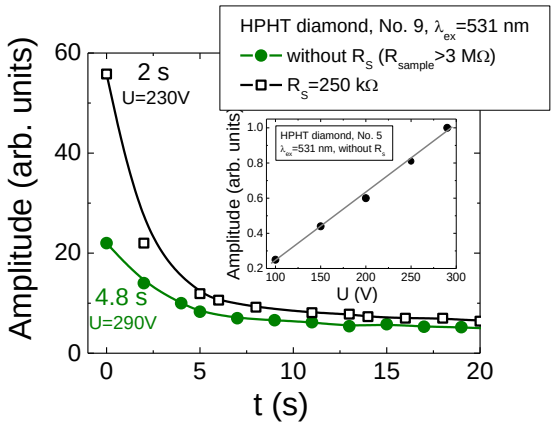

Fig. 5.13 Evolution of the current peak amplitude just after sharp switch-on voltage of 290 V without and with shunt resistance, measured in capacitor type. The current peak amplitude as a function of applied voltage for the fixed excitation intensity are shown in the inset.

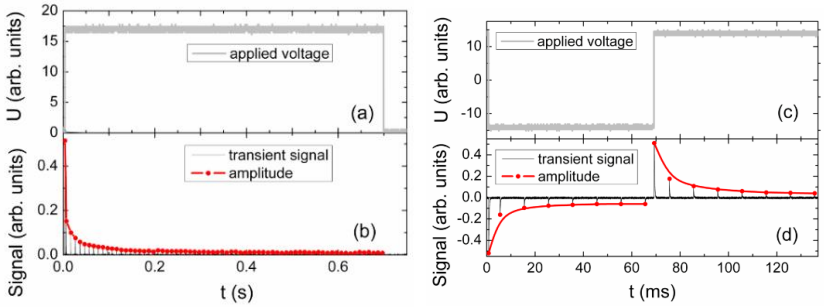

Fig. 5.14 a - The unipolar bias (16 V) voltage pulse applied to CVD diamond capacitor. b - A sequence of the charging current amplitudes. The solid (red) curve is an eye-guide which shows the charging current decrease after each laser pulse in sequence of 70 laser pulses. c - The bipolar ±14 V bias voltage pulse applied to CVD diamond capacitor. d - A sequence of the charging current amplitudes. The red curve shows the charging current reduction after each laser pulse for the negative and the positive polarity of bias voltage, respectively [A3].

A polarization effect, observed also by other authors [94,194,208,209], has been unveiled in diamond samples (Fig. 5.13a and Fig. 5.14). This effect appears as a decrease of the current peak amplitudes under action of a set of light pulses with invariable switched-on DC voltage. The current signal nearly disappears using the same injection conditions (λ_{ex}=531 nm) if a capacitor type detector is kept with unipolar applied voltage of moderate values for a long exposure to a set of the injection light pulses with rather high repetition rate.

The polarization effect was observed for all the investigated HPHT and CVD diamond samples, being a little bit stronger for HPHT samples. This effect can be slightly suppressed by increasing of the applied voltage value. Therefore,

evolution of the current peak amplitudes in profiling measurements has been examined just after a sharp voltage switch-on, i.e., ascribed to a single light pulse, to keep the same acting electric field. The recovery of the acting electric field can be implemented either by a short-circuiting of the device electrodes or by applying the opposite polarity voltage. In the latter case, the capacitor charging current pulse of the opposite polarity is inevitably observed. Therefore, examination of the drift current transients is preferential at elevated applied voltages of moderate and large values, in order to reduce the role of the polarization effect.

The recorded evolution of the current peak amplitude in HPHT diamond structure just after a sharp switch-on of the applied voltage is illustrated in Fig. 5.13a for 531 nm excitation wavelength. The polarization effect was found for both 531 and 354 nm excitation wavelengths. The nearly linear dependence of the current peak amplitudes on the applied voltage have been obtained for the HPHT diamond detectors (inset of Fig. 5.13). This characteristic proves the non-injecting electrodes over the range of applied voltages and of densities of the injected excess carriers. Therefore, the carrier trapping/recombination component has been hypothesized within induction currents in HPHT diamond samples. In case of the linear excess carrier excitation regime (Fig. 5.13), the formation of current transients can be described by the additional, carrier trapping component in Eq. 5.21. In the reported approaches [94], the polarization effect is exceptionally interpreted assuming only this carrier trapping/de-trapping current component caused by non-movable space charge formation. Rapid trapping of the excess carriers onto deep centres can lead to the formation of the localized non-movable charge within X_{e0} region. This localized charge within a distance X_{e0} keeps the induced charge $\Delta\sigma$ at electrode till then the excess carriers are thermally/optically de-trapped from the deep centres to conduction/valence bands. The long de-trapping time from these deep centres can be a reason for a rather long relaxation (Fig. 5.13) of the quasi-stationary polarization field. To clarify whether this polarization appears due to bulk localized charge within X_{e0} or via charge induction at electrode, the bypassing

circuit was employed using a shunt resistance connected in parallel to the device under test (Fig. 3.2a). Verification of polarization was based on possibility to drain the induced charge $\Delta\sigma$ from electrodes through shunt resistance. This shunt was tuneable to change the bulk localized charge within X_{e0} till then the de-trapped carriers are brought from the X_{e0} by their drift. The accumulated charge on electrodes can additionally be a reason for shielding of the external voltage source field. These measurements showed (Fig. 5.13) that the current signal increases and relaxation becomes faster, if shunt resistance is connected, relative to that without bypass circuit. Thereby, it can be assumed that the polarization effect is caused by a cumulating of the induction charge on electrodes due to excess carrier localization at deep centres. Then, the space charge within widths X_{e0}, X_{h0} can appear due to charging of deep traps by captured excess carriers. This bulk localized charge determines the slow component of recharging through excess carrier de-trapping.

These observations prove a hypothesis of the induced charge $\Delta\sigma$ on the electrodes and its accelerated extraction by partial shunting. The changes of the relaxation rate also imply a dynamic component of the polarization effect attributed to free excess carriers (Fig. 5.7c and Fig. 5.8). A current transient may contain two components (Eq. 5.20) for each type of excess carriers: i) caused by the excess carrier drift and ii) by the changes in time of the excess charge amount via carrier capturing into deep traps. As a result, the extracted charge at electrode appears (through the fast drift component) which prevents further extraction of the same type carriers. Really, the external battery determines flow of currents by balancing the induction charges, to keep invariable external voltage. As a consequence of surface and bulk charges, the internal electric fields appear, those are able to compensate the external source determined field. Thereby, the resulting electric field, acting on excess carriers, changes under cumulated excess carriers, if repetition rate of the injection light pulses is high in comparison with dielectric relaxation rate (Fig. 5.13). The polarization effect can alternatively be explained (Fig. 5.8) by free carriers accumulated within regions of electrodes (polarity of which, for instance, positively charged contact for

excess holes prevents extraction of free non-equilibrium holes to electrode) and separated by ENR at low applied voltages. This hypothesis seems to be supported by the existence of the polarization effect irrespective of the significant difference in concentration of deep traps in HPHT and CVD diamond. The electrically active impurities (e.g., concentration of nitrogen) in HPHT diamond is of about 2×10^{19} cm^{-3}, while it is less by a few orders of magnitude in CVD diamond, would be the reason for the localized bulk charge. Recombination of the accumulated excess carriers in the region between the ENR and the electrodes is prevented due to a lack of the annihilation counter-partners (for instance, excess electrons are always extracted by external field at positively charged electrode while excess holes are accumulated). The capacitor charging current (determined by the external battery) can then be reduced (after each injection light pulse) by increase of X_{e0} and X_{h0} (Fig. 5.8 and Fig. 5.14), where internal voltage compensates the battery's voltage (more and more after each pulse within a set of laser pulses). The sequenced generation of additional excess carriers with rather high rate of laser pulse repetition might then cause a cumulating of the induced charge $\Delta\sigma$ at electrode. It also allows us to understand why the polarization effect is independent of surface metallization of the same set of samples, as the induced charge $\Delta\sigma$ at electrode is not caused by ions collected on surface from atmosphere and from surface traps, as well. Thus, recovery of the applied field is only possible by reversing polarity of the external battery when surface charges cumulated at electrodes are rapidly extracted from electrodes.

To clarify the dynamic component of polarization field, experiments with pulsed external voltage source were performed using a scheme shown in Fig. 3.2c. The bias voltage pulse duration was chosen to cover a set of identical laser excitation pulses running with 100 Hz repetition rate. Then the set of current transients, flowing through a load resistance from a pulsed voltage source, was recorded. The first pulse is attributed to the charging current of the capacitor under test by external voltage pulse (Fig. 5.13a) while the remaining current pulses are ascribed to current transients originated from the carrier

injection pulses. The amplitude of current transients decreases under a sequence of excitation pulses due to an increase of the accumulated charge nearby the electrodes. The accumulated charge then screens the external electric field. Therefore, every further injection pulse in the sequence determines the smaller charging current (Fig. 5.13b). The sudden change of voltage polarity (Fig. 5.13c) leads to a rapid discharge (with sharp voltage decrease within rear phase of square-wave pulse) and fast charging of the discharged capacitor (Fig. 5.13d). Then, the first pulse of the opposite polarity charging reaches the same initial value (for a positive voltage pulse relative to the previous negative one). Afterwards, the decrease of charging current repeats, keeping symmetry of the relaxation curves (Fig. 5.13d). Thereby it can be inferred that polarization effect is originated from accumulation of the light injected excess carriers. Thereby it can be inferred that polarization effect is determined by processes modelled in the beginning of Section 5.2 (Fig. 5.8), and it is originated from accumulation of the light injected excess carriers.

The polarization effect is mostly manifested in the range of rather low voltages. However, it also depends on density of the injected excess carriers and injection (bulk or local) regime. To have a recordable current signal at rather low voltages (for bulk excitation regime covering the entire inter-electrode gap) a considerable amount of excess carrier pairs is needed, as the $i_{1,peak}$ signal value decreases with reduction of voltage due to reduction of surface charge n_0X_{e0} (Fig. 5.8). The nearly linear current $i_{1,peak}$ dependence on applied voltage U (Eq. 5.14), $i_{1,peak}\sim(S\varepsilon\varepsilon_0U/2X_{e0})\tau_{Mn0}^{-1}\sim U$) can be predicted in this range. The increased density n_0 of excess carrier pairs for a fixed low voltage may nevertheless enhance the dynamic polarization effect (Fig. 5.14). The latter leads to a reduction of $i_{1,peak}$ through screening of the external field (which can be assumed to be equivalent to a reduction of the effective U) if the laser pulse repetition rate is rather high. The short current transient represents the excess carrier drift (if $\tau_{tr}<<\tau_R$) or carrier recombination/trapping (if $\tau_{tr}>\tau_R$) dominated current components. For carrier recombination/trapping prevailing regime, the current pulse duration is close to a recombination lifetime. For the drift

determined current, the pulse duration should depend on the applied voltage. Then, the polarization effect of the long relaxation component, determined by the space non-movable charge formation, is more probable. Therefore, the profiling of current transients in the range of low voltages was performed by measurements using a single injection pulse method. The acting electric field was recovered to the same value for each excitation pulse by manipulating polarity of applied voltage.

Enhancement of the applied voltage reduces the role of the polarization effect in creation of the acting electric field (by weaker screening of the external source field). This leads to the increase of $i_{1,peak}$~($S\varepsilon\varepsilon_0 U/2X_{e0}$) with U. However, a width $X_{e,h,0}$ of depleted region simultaneously increases with U. The $i_{1,peak}$ dependence on U starts to saturate if rates of the enhancement of U and of $X_{e,h,0}(U)$ become the same (Fig. 5.13). Further enhancement of U to values capable to separate excess carrier pairs, the components of carrier ambipolar (τ_D) diffusion (which broadens the ENR region and supplies carriers to drift) and of drift (τ_{tr}) can be observable (Fig. 5.10), in case the carrier lifetime is properly long ($\tau_{tr} < \tau_D << \tau_R$). The latter components can be highlighted in the current transient profiling by applied voltage under bulk injection of excess carrier (either in parallel measurement geometry or by using the unfocused laser beams of diameter covering the inter-electrode gap in perpendicular measurement geometry, Fig. 3.2a and b, respectively).

For perpendicular geometry of measurements (Fig. 3.2b), the profiling of current transients has been implemented by varying a position of the local injection at sufficiently elevated voltages, to highlight the carrier drift components. This voltage should thus be sufficient to separate electron and hole pairs. It was assumed in the above discussed situations that the density of injected carrier pairs is kept rather small, a little above the threshold value, necessary to get the recordable currents. The enhancement of the injected carrier density leads, certainly, to an increase of the peak currents. However, the enhancement of excitation density has been performed gently, especially for capacitor type sensors of a rather small area of the electrodes. The injected large

density of carriers might be a reason for the screening of external field (Fig. 5.10). Then current contains pure convection component governed by the ambipolar diffusion. The geometrical and the voltage as well as the injection parameters should be properly chosen to perform correctly (by avoiding diffusion components) the profiling experiments, when using the perpendicular injection regime.

5.2.6. Profiling of current transients in HPHT diamond

Variation of current transients obtained by changing the fixed values of applied voltage in capacitor type detector made of HPHT diamond sample No. 5 is illustrated in Fig. 5.15. Here, excitation by 531 nm light pulses was implemented. In this case, excess carrier generation from deep centres prevails and a bulk charge domain is injected. The shape of the induced current transients is inherent for the carrier recombination-drift dominated process.

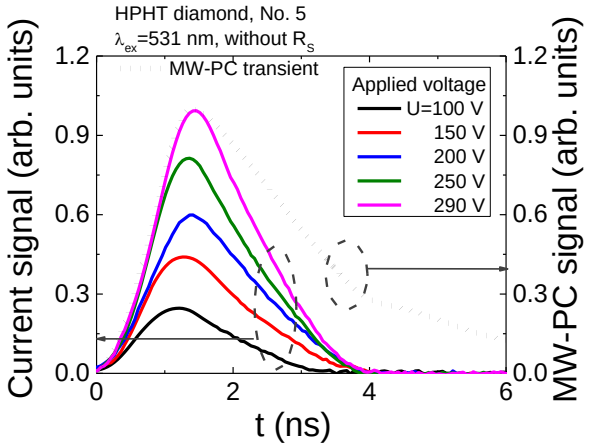

Fig. 5.15 Variation of the induction current transients dependent on the applied voltage in a capacitor type detector made of a mosaic set of implanted contacts and metal electrodes containing HPHT diamond sample No. 5 [A1].

The initial current peak can be ascribed to the bipolar drift of the injected carriers, where pulse duration and further current decrease can be ascribed to carrier trapping/recombination. The normalized amplitude of MW-PC signal (Fig. 5.15) is exploited to adequately scale the MW-PC and ICDC transients. The range >100 V of applied voltages (Fig. 5.15) was sufficient to get a short (<2 ns) transit time for the drift-recombination of the injected carriers, where the role of the polarization effect is reduced. The rather large applied voltage determines the sufficiently wide depletion regions (X_{e0}, X_{h0}) nearby the

electrodes. Therefore, the current component ascribed to extraction of the diffusion brought carriers is also rather short, and it overlaps with current component attributed to carrier drift. In order to separate different components of the induced current in time scale, where temporal resolution and duration of processes is of the same order of magnitude, the deconvolution of transients was performed using the parameters of the external circuit and of excitation pulse.

However, it was not possible to clearly discriminate the components of a current transient due to short characteristic times (τ_{tr}, τ_R). This issue can also be implied from Fig. 5.15, where no clear shift of the kink point relative to time axis, attributed to arrival of drifting carriers, is resolved when applied voltages have been varied significantly. Such a result hints the competition between the drift and recombination, assumed within equation (Eq. 5.20). The similar voltage dependent characteristics (transient shapes and temporal parameters) have been obtained for all the investigated HPHT diamond detectors under injection of bulk domains by UV light (354 nm) pulses. These results show that usage of the pressed plate electrodes (pinned to either bare polished wafer samples surfaces (No. 7 and No. 9) or to additionally metallized surfaces (sample No. 5)) exhibits the capacitor type detector features.

The cross-sectional profiles of the peak values of current induced by scanning location of a focused injection beam of either 531 nm or 354 nm light, obtained for HPHT diamond sample No. 9, are illustrated in Fig. 5.16. This sample is rather homogeneous and contains a single growth sector of cubic orientation. A strip focusing regime implemented by a cylindrical lens enables to exclude the impact of the transverse carrier diffusion.

Flat vertex of the profile, scanned by using 531 nm (Fig. 5.16) light pulses, indicates the recombination prevailed drift process. The profile unveiled by the two-photon bulk domain injection, when using 354 nm (Fig. 5.16) light pulses, has a clear relief. The peak values of the induced current are increased by approaching of injection beam location to electrodes. This indicates the prevailing of carrier drift. Then, the current increase at electrodes is explained by the shortest drift path and, thereby, the shortest transit time.

Complementarily, these current values are the smallest ones for the injection beam locations in the mid of an inter-electrode gap.

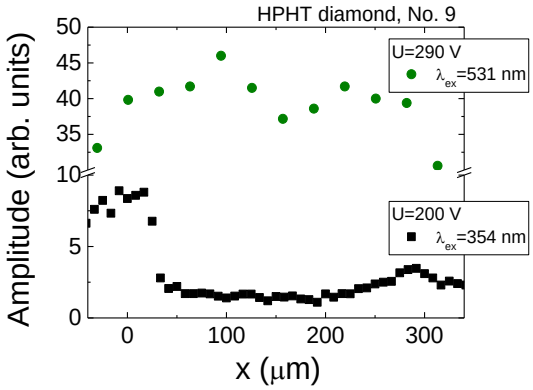

Fig. 5.16 The cross-sectional profiles of the peak values of current traced by scanning location of a focused injection beam of 531 nm (green circle) and 354 nm (black square) light, obtained for HPHT diamond sample No. 9.

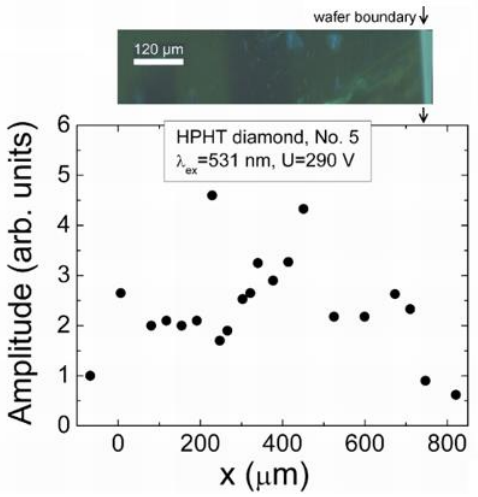

Fig. 5.17 The cross-sectional profile of the peak values of current recorded by scanning location of a focused injection beam of 531 nm light, obtained for HPHT diamond sample No. 5. The microscopy image of wafer boundary (the extended defects are imaged by luminescence spots (bright-blue)) taken in UV light for the scanned area is shown on the top [A1].

Carrier recombination also might be an additional reason for reduction of the collected charge when the drift time is close or even exceeds that of carrier recombination lifetime. A cross-sectional profile of the induction current obtained for detector formed on the sample No. 5 (inclusion of metallic precipitates was visualized by microscopy imaging within sample depth (Fig. 5.17) shows a random distribution of the current peak values. Such a profile qualitatively correlates with cross-sectional wafer image where defects of different size and origin can be resolved.

5.2.7. Profiling of current transients in CVD diamond

Evolution of the induced current transients, recorded in CVD diamond device profiled at fixed excitation intensity by varying applied voltage, are illustrated in the inset of Fig. 5.18. The transients displayed within a sub-microsecond time scale enable observation of both current components, namely, i_1 and i_2, discussed in the beginning of this Section 5.2 (Eq. 5.19). The peak values of the drift current component i_1 significantly exceed those attributed to the diffusion supplied carrier extraction component i_2. Increasing of the applied voltage leads to an enhancement of a width of the depleted regions at electrodes and of the acting electric field. The reduced time necessary to extract the diffusion supplied carriers determines a shift of the peak position ascribed to the i_2 current component. Thereby, the parameter of an effective time $\tau_{D,eff}$ ascribed diffusion, determined as a time shift between the current components i_1 and i_2 fixed by their peak values, can be introduced. This $\tau_{D,eff}$ time (Fig. 5.18) is weakly dependent on applied voltage for the range of elevated U>50 V values, where the excess carrier drift prevails. Contrary, reduction of applied voltage below the U <50 V leads to a sharp increase of $\tau_{D,eff}$. $\tau_D \cong d_{eff}^2/4\pi^2 D_a$ values, extracted for the voltage range U<50 V, indicates a prevalence of diffusion process. This enables estimation of values of a coefficient D_a of the carrier ambipolar diffusion in CVD diamond, assuming that current $i_{2,peak}$ peak value is attributed to the main (regular regime [201]) mode (k=0) of diffusion in sample with infinite surface recombination. The estimated value of D_a=97 cm^2/s is in good agreement with those values calculated using the parameters of carrier drift mobilities, published in literature [208].

In order to examine the current fast component i_1, current transients were recorded within short (a few ns) display scale. Evolution of this transient component as a function of applied voltage is represented in Fig. 5.19a.

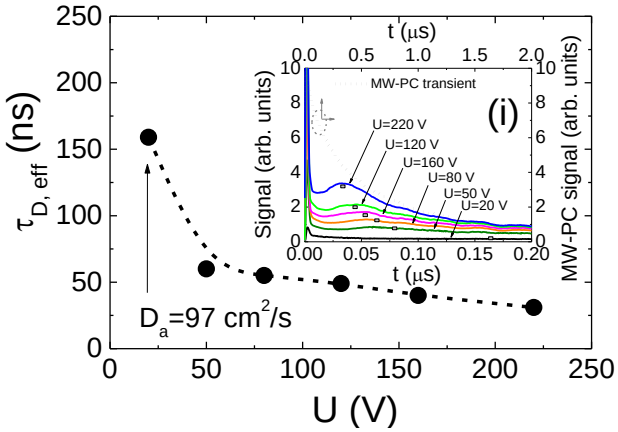

Fig. 5.18 Diffusion ascribed effective time $\tau_{D,eff}$ (determined as a time shift between the current components (peak values $i_{1,peak}$ and $i_{2,peak}$) within a long time scale of transient display) as a function of applied voltage. In the inset, variation of the current and MW-PC transients is presented. These transients are recorded in the CVD diamond device by changing bias voltage when excess carrier bulk domain is injected through electrode using UV 354 nm light pulses [A3].

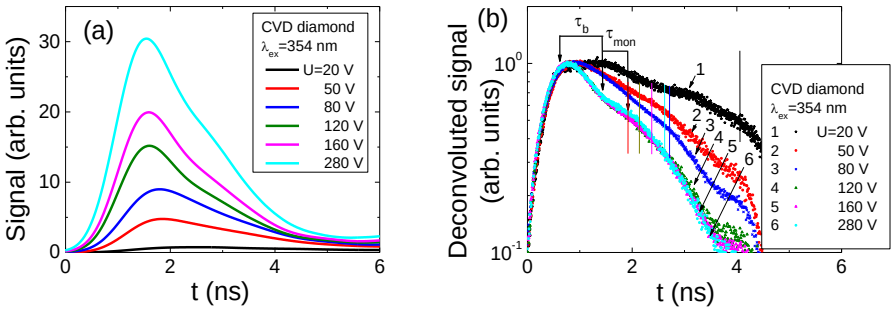

Fig. 5.19 a - Variation of the current transients recorded in short display scale by changing bias voltage when excess carrier bulk domain is injected through electrode using UV 354 nm light pulses; b - The deconvoluted transients as a function of applied voltage. The bipolar (τ_b) and monopolar (τ_{mon}) drift components are denoted by arrows for drift of electrons within the final phase of transient at U = 280 V [A1].

The asymmetric shape transients, relative to a peak position, were obtained. Unfortunately, due to improper temporal resolution of the experimental arrangement exploited, direct analysis of drift characteristics is impossible. Therefore, the transients have been deconvoluted using Gaussian convolution function with parameters adjusted to the initial delay component correlated with the experimental transients (Fig. 5.19b). This kink instant on vertex of a current pulse is employed to estimate the transit time which is measured between the initial peak ($i_{1,peak}$, this indicates the end of excitation pulse), and the rearward instant of kink formation on vertex of current pulse, which indicates the end of drift. The instant of a kink point, (shown by vertical

lines in Fig. 5.19b, depends on applied voltage, and it shifts towards the beginning of current pulse, with enhancement of voltage. There the components of the bipolar and monopolar drift can tentatively be implied. However, the unambiguous attribution of these components to the paths of the hole and electron drift and to their transit times is very complicated in the parallel geometry (Fig. 3.2a) regime. Such changes again have a clear tendency only in the range of elevated voltages $U > 50$ V. For the range of $U < 50$ V, the amplitude of the deconvoluted transient (Fig. 5.19b) increases considerably together with its duration, and this implies an overlap of drift and diffusion governed components. In this case, the induced current transients are inappropriate for analysis of transit times.

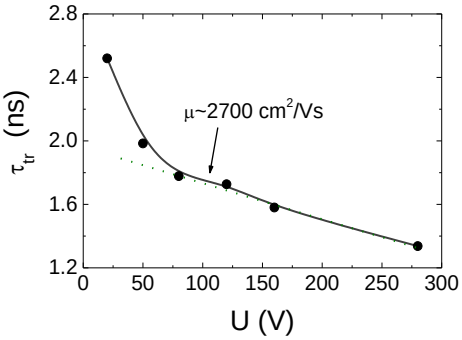

Fig. 5.20 The transit time evaluated from the deconvoluted current transients as a function of applied voltage using an approximation of the flat vertex of pulse.

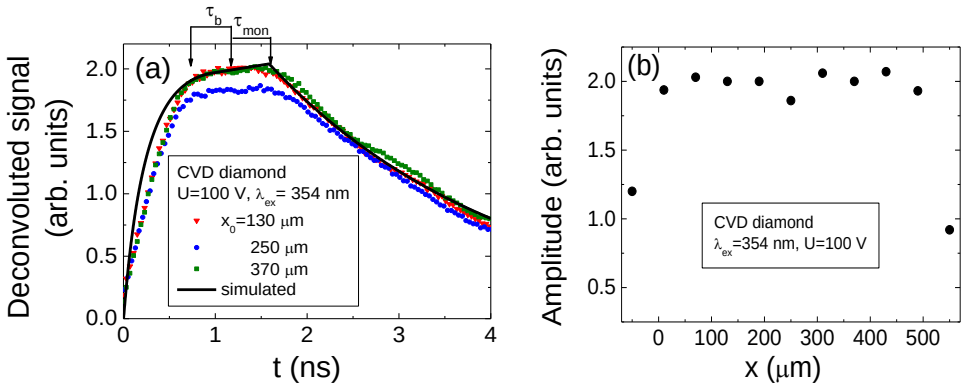

Fig. 5.21 a - The deconvoluted current transients for several injection positions recorded within cross-sectional scans of the CVD diamond capacitor type detector. The bipolar (τ_b) and monopolar (τ_{mon}) drift components are denoted by arrows for drift of electrons within the final phase of transient. The solid curve represents a simulated transient for injection location x=130 μm relatively to the negative electrode at voltage $U_{bias\ DC}$ = 100 V; b - The amplitude of the induced current (ascribed to the bipolar drift component) as a function of the injection position within inter-electrode gap, measured in capacitor type detector made of CVD diamond [A1].

The transit time τ_{tr} increases almost linearly with reduction of applied voltage (Fig. 5.20) for the range of voltages U = 75–300 V. There precision of evaluation of the τ_{tr} falls down in the range of U>200 V. There both the extraction depth and an amount of extracted charge become dependent on applied voltage, and they partially compensate variations of each other. Nevertheless, the roughly estimated value of carrier mobility $\mu \approx [2X_0^2/(U\tau_{tr})] \approx 2700$ cm^2/Vs is in good agreement with the values reported in literature [208]. This evolution of a short current component enables only estimation of the averaged carrier mobility at assumption of the flat vertex of current pulse. The assumption of the flat vertex of a current pulse is closely related to the steady-state models where charge supplied from voltage source during carrier drift is ignored [197,204]. The widely developed steady-state models are based on assumption of the independent drift of holes as well as of electrons. The Shockley-Ramo's effect is ignored in these models. The steady-state model for the carrier drift process can be simulated by using TCAD [204]. However, the simulated transients using the steady-state and the dynamic models can considerably differ [204].

The assumption of non-correlated drift of holes and electrons, used in steady-state models, is equivalent to the increased drift path d_Σ, as $d_\Sigma = d_e + d_h > d$, which exceeds the inter-electrode gap d. It can be also interpreted that the double elementary charge e, i.e. $e \times 2$, is carried during the bipolar drift of an electron-hole (e-h) pair. Therefore, a e-h pair carries (over the path of the bipolar drift) the same elementary charge e as either a single hole or electron [204], which proceeds the charge transport process after one counter-partner of a pair reaches the electrode. Thus, ignoring of the changes of the acting electric field, caused by charge supplied to electrodes from an external voltage source, leads to the underestimated carrier mobility values, if $d_\Sigma > d$ is considered.

In current transients (Fig. 5.21a), recorded by cross-sectional profiling on CVD diamond sample, only a short current component has been observed ascribed to the drift of the separated electron-hole sub-domains. The simulated transients (Fig. 5.21a) have been employed for evaluation of carrier mobilities

using developed dynamic models and published in more detail in [9,197]. There parameters of the injected charge amount, of the external circuit, of carrier trapping/detrapping have been taken into account in the simulations. Values of electron and hole mobility values of μ_e=4000 cm^2/Vs and μ_h=3800 cm^2/Vs, respectively, have been evaluated by fitting of the simulated transient to the experimental one at different applied voltages. The close values of μ_e and of μ_h, nevertheless, lead to a rather flat vertex of the recorded transients. The separated values of μ_e=4000 cm^2/Vs and μ_h=3800 cm^2/Vs by using the cross-sectional profiling of the charge injection location exceed that value μ=2700 cm^2/Vs extracted from the voltage profiling on CVD diamond sample in parallel measurement geometry. The profile of the induced current amplitude as a function of this beam location also exhibits a rather flat vertex (Fig. 5.21b). This profile is also linked to the assumption of close values of μ_e and of μ_h. A shallow sag within the profile vertex, when excitation beam is localized in the mid of the inter-electrode gap (Fig. 5.21b) can be attributed to current reduction due to the increased transit time.

The reliable discrimination of prevailing mechanisms in the formation of shapes and durations of the induced current pulses can be implemented by combining profiling of current transients by injection of the bulk and the localized excess carrier domains. It has been shown that current transient profiling by the cross-sectional scans of the injection location can be a sensitive tool for identification of depth distribution of growth defects. The cross-sectional profiling of current transients enabled us to evaluate the impact of diamond crystal quality on the operational characteristics of the capacitor type detectors.

6. Spectroscopy of defects in heavily irradiated Si

6.1. Difficulties of identifying defects in heavily irradiated Si

Despite of significant progress in development of WBG semiconductor based detectors, the Si based detectors are currently widely used as particle detectors in experiments of high energy physics [210]. A deep understanding of radiation damage of Si particle detectors is important in order to extend the sensor lifetime and radiation hardness and potentially to restore their functionality after degradation caused by irradiation. A way to recover detector operational features is heat treatments at technically acceptable temperatures [21]. In order to develop annealing procedures, there is a need to understand the evolution of the most harmful radiation induced defects under heat-treatment procedures. The most harmful defects induced by hadron irradiations seem to be clusters those are fast recombination centres and lead to decrease of CCE in Si particles detectors. Heat treatments at elevated temperatures might be a tool for destruction of clusters. However, it is quite difficult to investigate the radiation-induced defects in defects-rich materials by applying conventional methods. Therefore, the Current-DLTS (I-DLTS) and the temperature-dependent trapping lifetime (TDTL) techniques can be applied in order to prevail dominant defects despite of the large ratio of trap concentration to doping. Thus, these methods have advantage over other conventional methods (e.g. C-DLTS, TSC) due the possibility to be employed for the defect identification in heavily irradiated materials. I-DLTS and TDTL techniques have already been used to investigate the radiation damage in Si samples irradiated with electrons [106]. However, the radiation damage caused by charged hadrons may differ from that caused by electrons. There is also a lack of investigations that address the pion-induced radiation damage in Si material.

6.2. Spectroscopy of trapping centres in heavily irradiated Si

6.2.1. Types of irradiated samples and irradiation conditions

Table 6.1 describes the used materials and performed irradiations. Wafer fragments of the CZ (380 μm thick) and FZ grown (280 μm thick) n- and p-type

Si of resistivity >3 kΩcm were irradiated with hadrons up to fluences that are expected for inner layers of tracking detectors for experiments at the LHC. The Schottky barrier was formed on the same irradiated-material wafer fragments, by 30 nm thick Au evaporated layer on HF freshly-etched wafer top-surface. The ohmic contact (area 3.85×10^{-1} cm^2) was fabricated by evaporation of Ni (100 nm).

Irradiations by protons and pions were performed at CERN and at Paul Scherrer Institute, respectively. The relativistic protons and pions induce depth-homogeneous distribution of radiation defects in samples of employed thicknesses.

Table 6.1 Description of samples and irradiation conditions.

Type of irradiation	Protons (p)		Pions (π^+)	
Relativistic hadrons	24 GeV/c		300 MeV/c	
Fluence range	10^{12}-3×10^{16} p/cm^2		10^{11}-3×10^{15} π^+/cm^2	
Si material	FZ n-Si	CZ p-Si	CZ n-Si	FZ n-Si
Dopant concentration/ resistivity	10^{12} cm^{-3} >3 kΩcm	10^{12} cm^{-3} 10 kΩcm	10^{12} cm^{-3} >3 kΩcm	10^{12} cm^{-3} >3 kΩcm

The isochronal anneals for 24 hours were performed at the temperatures in the range from 80 °C to 300 °C by temperature steps of 20 °C to 50 °C in N_2 gas ambient. The hadron irradiated samples were isothermally annealed at 80 °C up to 5 hours before isochronal (24 h) anneals at elevated temperatures.

6.2.2. Spectra recorded on n-type FZ and p-type CZ Si irradiated by 24 GeV/c protons

For Si wafer fragments as-irradiated by hadrons, the trapping component within MW-PC transients is not observable. The τ_R are nearly independent of technology of Si material (Fig. 6.1). Moreover, nearly the same τ_R values are obtained for a fixed fluence (calibrated to 1 MeV neutron equivalent) value irrespective of hadron type (Fig. 6.1). Values of τ_R and their dependencies on hadron irradiation fluence, measured on as-irradiated Si detector structures and wafer samples, actually coincide for both measurement modes, i.e. taken from irradiation chamber (a) or during irradiation (b), respectively (Fig. 6.1) [211]. This result implies that radiation defects initially form the deep levels, which act as pure recombination centres. Heat-treatments at T_{an}=80 °C lead to an

appearance of trapping effect which determines a relatively small increase of τ_R (Fig. 6.1a), even after long-exposure anneals. This can be explained by insufficient thermal energy (kT_{an}) to activate transforms of the radiation defects.

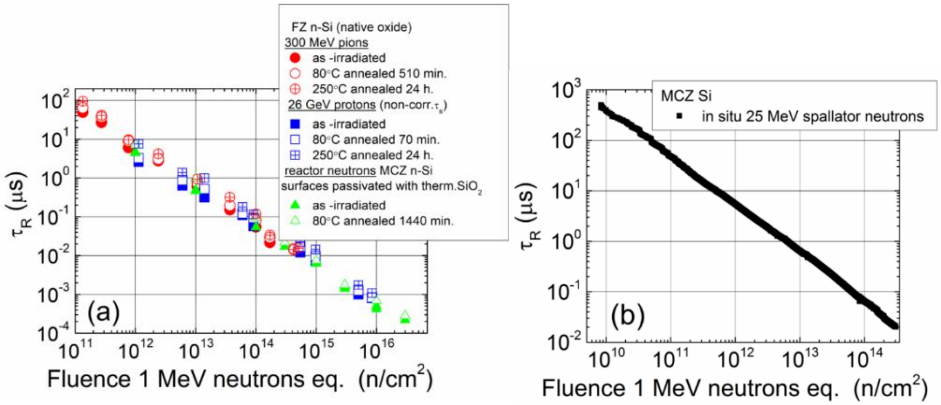

Fig. 6.1 Recombination lifetime in the as-irradiated and annealed Si wafer fragments as a function of fluence of the reactor neutrons, 24 GeV/c protons and 300 MeV/c pions (a). *In situ* variations of recombination lifetime as a function of spallator neutrons. Neutron irradiated MCZ (CZ Si with applied magnetic field) material was also examined (b) [A6].

Thus, the temperature scans of trapping lifetime variations allow to examine the thermal emission centres ascribed to the dominant point defects (Fig. 6.2). In spectra for the 24 GeV/c proton irradiated CZ p-Si samples (Fig. 6.2) using fluences of Φ=10^{13} and 5×10^{13} p/cm^2, the dominant peaks with activation energies of 0.17, 0.23, and 0.32 eV have been observed after heat-treatments at 200 °C. The activation energies have been extracted by fitting (using Eq. 3.16) the experimental TDTL spectra (Fig. 6.2). The highlighted defects have been attributed to H complexes [212], $V_2^=$ and VO centres.

The trapping lifetime changes, recorded on n-type FZ Si samples, irradiated with fluences of 10^{14} and 5×10^{15} p/cm^2 and heat-treated at 250 °C (Fig. 6.3) reveal the dominant traps, ascribed to VO, H-related complexes [212], di-vacancies (V_2^- and $V_2^=$) [213–215], and an unidentified centre with activation energy 0.3 eV. Due to the considerably low concentration of oxygen impurities in FZ Si, the VO centres have been identified only for the sample, irradiated with Φ=10^{14} p/cm^2.

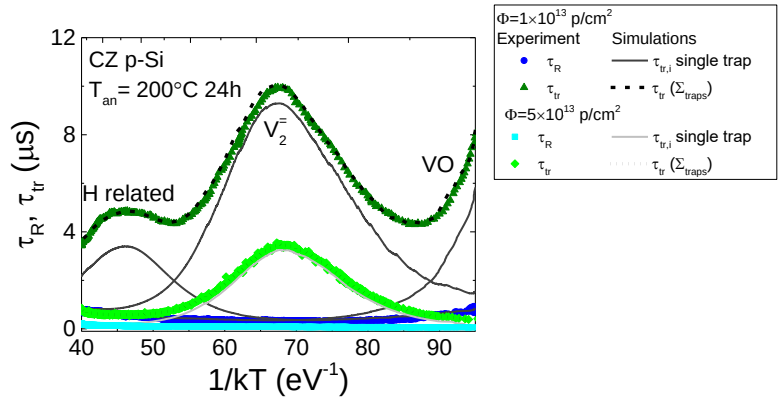

Fig. 6.2 Comparison of the simulated and experimental variations of the $\tau_{tr}(kT)$ for p-type CZ Si samples irradiated with fluences 1×10^{13} and 5×10^{13} p/cm^2 after 200 °C heat-treatment [A6].

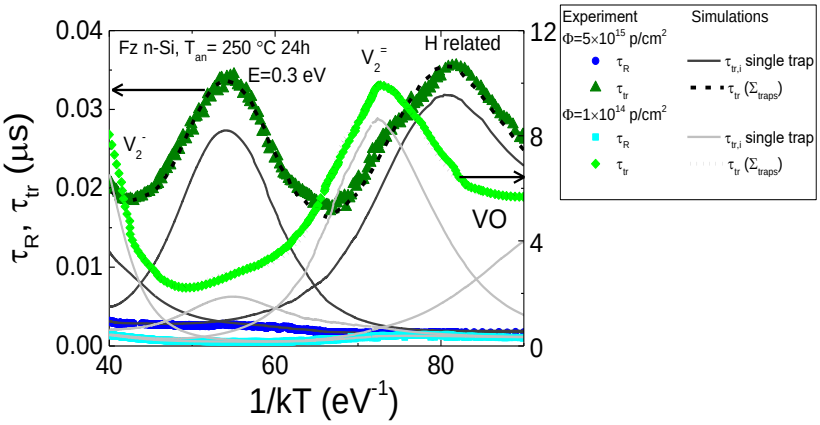

Fig. 6.3 Comparison of the simulated and experimental variations of the $\tau_{tr}(kT)$ for n-type FZ Si samples irradiated with fluences 1×10^{14} and 5×10^{15} p/cm^2 after 250 °C heat treatment [A6].

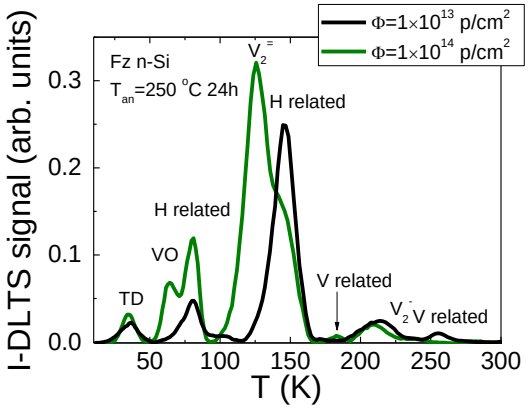

Fig. 6.4 I-DLTS spectra recorded on n-type FZ Si diodes irradiated with 1×10^{13} p/cm^2 and 1×10^{14} p/cm^2 fluences and annealed at 250 °C [A6].

Comparison of DLTS spectra, recorded on n-type FZ Si diodes irradiated with 10^{13} p/cm^2 and 10^{14} p/cm^2 fluences and annealed at 250 °C, is presented in

Fig. 6.4. The predominant peak (150K) for the sample irradiated with fluence Φ=10^{13} p/cm^2 is attributed to H-related defects (E_{tr}=0.32 eV). While, spectral peaks, observed at 220K (0.42 eV) and 260K (0.57 eV), are attributed to di-vacancy (V_2^-) and V-related defects. The spectral peaks at low temperatures, 80K (E_{tr}=0.2 eV) and 40K (0.15 eV), are attributed to H-related defects and thermal donors (TD), respectively. In samples irradiated with higher fluence Φ=10^{14} p/cm^2, the predominant peak is attributed to $V_2^=$ (E_{tr}=0.23 eV). The additional peak obtained at the 60K is attributed to VO defects. An increase of the amplitudes of the peaks at 80K, 60K and 40K has been observed.

6.2.3. Spectra recorded on n-type FZ and CZ Si irradiated by 300 MeV/c pions

The dominant defects in n-type FZ Si, induced by pion irradiations and heat treatments using T_{an}=150 °C, have been ascribed to di-vacancies (V_2 and $V_2^=$) and to VO complexes, as revealed by TDTL measurements (

Fig. 6.5). While for the CZ Si samples processed using the same procedures, the predominant defects are $V_2^=$ and C_iC_s complexes [213–215]. After heat treatment at T_{an}=150 °C (Fig. 6.6), the $V_2^=$ and VO defects become predominant in FZ and CZ Si. It has been observed, that C_iC_s complex anneals out in CZ Si samples (Fig. 6.6), irradiated with Φ =1×10^{14} π^+/cm^2. There, the V_2 complex and the unidentified defect with activation energy E_{tr}=0.3 eV have been revealed in FZ n-Si samples.

From DLTS measurements, performed on samples irradiated with small pion fluences (Fig. 6.7), VO, $V_2^=$, H-related and V-related defects [212] have been inferred as dominant in CZ n-Si samples after heat treatment at 250 °C. While, the TD and V_2^- defects are dominant in the FZ n-Si samples. Concentrations of these defects, which are proportional to the obtained peak amplitudes in DLTS spectra, indicate that production of radiation defects is less efficient for FZ Si.

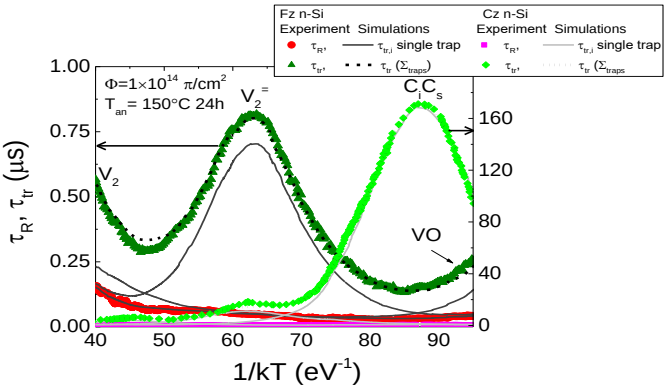

Fig. 6.5 Comparison of the simulated and experimental variations of $\tau_{tr}(kT)$ for n-type FZ and CZ Si samples irradiated with fluence Φ=1×10^{14} π^{+}/cm^{2} and heat-treated at 150 °C [A6].

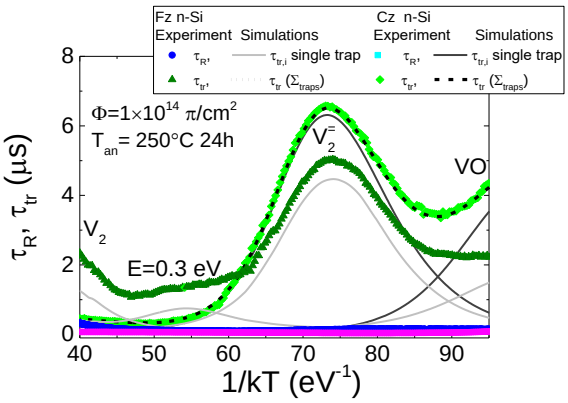

Fig. 6.6 Comparison of the simulated and experimental variations of the $\tau_{tr}(kT)$ for n-type FZ and CZ Si samples irradiated with fluence Φ=1×10^{14} π^{+}/cm^{2} after heat treatment at 250 °C [A6].

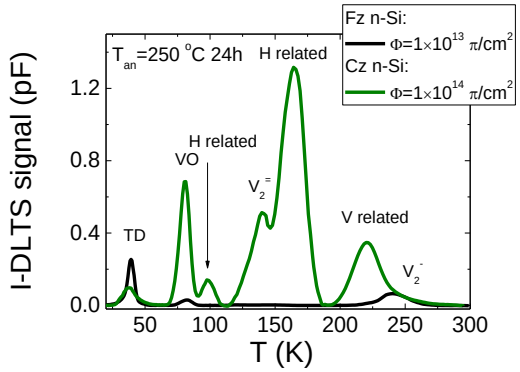

Fig. 6.7 I-DLTS spectra recorded on n-Si samples of FZ material, irradiated with 1×10^{13} π^{+}/cm^{2} fluence, and CZ material, irradiated with Φ =1×10^{14} π^{+}/cm^{2} fluence after heat treatment at 250 °C [A6].

The resolved spectra of point defects and their variations after heat treatments imply dissociation of radiation clusters, those prevail in the hadron

as-irradiated material. Therefore, the density of the heat-treatment produced point defects increases with anneal steps.

6.2.4. Comparison of results obtained by TDTL and I-DLTS techniques

The parameters of traps introduced by irradiation of relativistic protons and pions of nearly the same fluence are listed in Tables 6.2 and 6.3, respectively.

Table 6.2 Anneal dependent variation of the parameters of the trapping centres introduced by 24 GeV/c protons.

Activation energy (eV)	Defect identification	Heat-treatment	T_{an} 100 °C	T_{an} 150 °C	T_{an} 200 °C	T_{an} 250 °C
			Φ=5×10^{13} p/cm^2			
		Sample material	Concentration of trapping centres (10^{13} cm^{-3})			
0.32±0.02	H-related [212]	CZ p-Si	7	15	10	220
0.36±0.02	V_2^0 [212]	FZ n-Si	2	11	6	660
0.25±0.01	$V_2^=$ [212]	CZ p-Si	8	12	14	160
		FZ n-Si	8	9	10	180
0.18±0.01	VO [212]	CZ p-Si	0.5	1	1.2	20
		FZ n-Si	0.5	1	1.6	7

Table 6.3 Anneal dependent variation of the parameters of the trapping centres introduced by 300 MeV/c pions.

Activation energy (eV)	Defect identification	Heat-treatment	T_{an} 100 °C	T_{an} 150 °C	T_{an} 200 °C	T_{an} 250 °C
			Φ=3×10^{13} π^+/cm^2			
		Sample material	Concentration of trapping centres (10^{13} cm^{-3})			
0.36±0.02	V_2^0 [212]	CZ n-Si	8	13	25	5
		FZ n-Si	2	6	12	20
0.25±0.01	$V_2^=$ [212]	CZ n-Si	7	15	20	20
		FZ n-Si	2	7	14	18
0.18±0.01	VO [212]	CZ n-Si	0.2	0.2	0.2	0.6
		FZ n-Si	0.4	0.7	0.8	1

The non-monotonous variations of trap densities after different anneal steps can be deduced from Tables 6.2 and 6.3. The similarity between DLTS spectra, obtained for samples rather low fluence irradiated by protons and pions, indicate that the irradiation with various type penetrative hadrons induce the same defects. Nevertheless, irradiations with pions lead to introduction of the VO, $V_2^=$, H- and V-related complexes which are dominant in the n-type CZ Si samples. While, thermal donors (TD) and V_2^- defects are dominant in the n-type FZ Si samples. The amplitudes of peaks within DLTS and TDTL spectra, recorded on samples irradiated with the same fluence, indicate that the

production of radiation defects is less efficient in FZ Si, due to the lower concentration of the contaminants and native defects in comparison with CZ Si.

Density of V- and H-related defects increases with T_{an} due to enhancement of defect activation energy with heat-treatment temperature. The C_iC_s complexes have been revealed to be the predominant defect in pion irradiated CZ n-Si material after heat treatment at 150 °C, as carbon impurities of concentration $>10^{16}$ cm^{-3} and oxygen impurities of $>10^{18}$ cm^{-3} are present in the pristine Si material. However, in the hadron irradiated material, anneal induced transformations of cluster defects lead to predominance of C_iC_s complexes in CZ Si at intermediate heat treatment temperatures of 150 °C. Also, concentration of oxygen impurities of $\sim10^{16}$ cm^{-3} is sufficient to observe VO traps after intermediate heat treatment at 150 °C. The subsequent annealing out of the C_iC_s traps is accompanied by formation of the unidentified defect (E_{tr}=0.3 eV). The latter defect had been also observed in electron irradiated Si [106].

Carrier recombination lifetime shows a tendency of linear decrease in log-log scale (Fig. 6.1), due to increase of the density of cluster defects (N_{cl}) with fluence of hadrons. Assuming the same rate of cluster destruction by heat treatments, the ratio of point defect density to that of clusters decreases with enhancement of fluence. Thus, the amplitude of trapping component is also reduced for heavily irradiated and annealed samples, and sensitivity of TDTL technique, as well as I-DLTS, to resolve spectra of emission centres falls down with increase of fluence (as $\tau_{inst,tr} \approx \tau_R \times (N_{tr}/N_{C,V}) \times \exp(E_{tr}/kT)|_{Ktr>1, Ntr/Ncl<1} \sim N_{tr}/N_{cl} \sim \tau_R$ even for $t \to \infty$). Heat treatment induced transformations and reactions of point radiation defects (for instance, $V \to V_2$, VO) with native ones lead to the intricate changes of TDTL spectra dependent on Si material type and T_{an}, as well as on irradiation fluence. Nevertheless, a clear tendency of cluster destruction and consequent formation of trapping centres with enhancement of isochronal T_{an} can be deduced from Table 6.2 and Table 6.3. While, different shape functions (increasing, non-monotonous, saturating) can be implied from Table 6.2 and Table 6.3 for anneal induced variations of the density of various emission centres, identified for a fixed irradiation fluence.

It has been demonstrated that contactless spectroscopy of carrier recombination and trapping lifetime using MW-PC and TDTL temperature scans allows simultaneous control of interactions among several radiation defects within large fluence irradiated Si structures. This technique is promising for spectroscopy of radiation defects when the standard contact methods become unsuitable due to the disordered structures and internal electric fields existing within heavily radiation damaged materials.

7. Summary

1. The nearly invariable values of charge collection efficiency and carrier lifetimes in AT GaN over wide range of moderate neutron fluences $\Phi \leqslant 10^{15}$ cm^{-2} confirmed the high radiation hardness of this material. The prevailing of vacancy associated complexes of $V_{Ga}O_N$ or $V_{Ga}H_N$ are revealed to be responsible for the degradation of neutron-irradiated AT GaN samples.
2. The observed decrease of the stretched-exponent index β_{SER} with enhancement of threading dislocation density (TDD) indicates the increase of disorder degree dependent on the growth regimes of the MOCVD GaN epilayers. Reduction of τ_{SER} lifetimes with increase of density of threading density (TDD) implies prevailing of carrier decay through dislocation cores when TDD enhances.
3. Values of the PL-decay times are nearly independent of edge dislocation density and their values vary not more than 20% when changing the growth regimes of MOCVD GaN layers. Vacancy, anti-site and carbon impurity related defects dominate within MOCVD GaN single-crystal regions, as deduced from PPIS measurements.
4. *In situ* measurements of proton-beam excited luminescence and BELIV transients, during proton irradiation, allowed to unambiguously separate the recombination processes in the radiative and non-radiative channels. These devices are suitable for simultaneous detection of both the electrical and optical signals.
5. The potential applications of the rearranged GaN-LED sensors to dosimetry has been demonstrated.
6. Analytical models have been developed and applied to interpret the evolution of current pulse transients induced by the bulk and localized domains of injected charge carriers. The current components ascribed to carrier drift, diffusion and recombination processes have been clearly discriminated.

7. The combined profiling of current transients by injection of the bulk and of the localized domains of excess carriers enable the evaluation of the carrier transport characteristics for CVD diamond.
8. The current transient technique based on profiling by the cross-sectional scans of the injection location can be a sensitive tool for identification of the depth distribution of native defects in diamond samples.
9. TDTL and I-DLTS measurements allow to resolve interactions among several radiation defects in heavily irradiated Si structures. The increase of concentration of the emission centres in the heat-treated Si samples implies dissociation of the extended radiation clusters those act as the prevailing recombination centres in the hadron as-irradiated Si materials.

References

[1] C.J.H. Wort, R.S. Balmer, Diamond as an electronic material, Mater. Today. 11 (2008) 22–28. doi:10.1016/S1369-7021(07)70349-8.

[2] K. Takahashi, A.A. Yoshikawa, A. Sandhu, Wide bandgap semiconductors:fundamental properties and modern photonic and electronic devices, Springer, 2007.

[3] S. Fujita, Wide-bandgap semiconductor materials: For their full bloom, Jpn. J. Appl. Phys. 54 (2015) 30101. doi:10.7567/JJAP.54.030101.

[4] J.L. Abelleira Fernandez, C. Adolphsen, A.N. Akay, H. Aksakal, J.L. Albacete, S. Alekhin, P. Allport, V. Andreev, R.B. Appleby, E. Arikan, N. Armesto, G. Azuelos, M. Bai, D. Barber, et al, A Large Hadron Electron Collider at CERN Report on the Physics and Design Concepts for Machine and Detector, J. Phys. G Nucl. Part. Phys. 39 (2012) 75001. doi:10.1088/0954-3899/39/7/075001.

[5] H. Heinke, V. Kirchner, S. Einfeldt, D. Hommel, X-ray diffraction analysis of the defect structure in epitaxial GaN, Appl. Phys. Lett. 77 (2000) 2145. doi:10.1063/1.1314877.

[6] P. Fini, X. Wu, E.J. Tarsa, Y. Golan, V. Srikant, S. Keller, S.P. Denbaars, J.S. Speck, The effect of growth environment on the morphological and extended defect evolution in GaN grown by metalorganic chemical vapor deposition, Jpn. J. Appl. Phys. 37 (1998) 4460–4466. doi:10.1143/JJAP.37.4460.

[7] M.E. Coltrin, J. Randall Creighton, C.C. Mitchell, Modeling the parasitic chemical reactions of AlGaN organometallic vapor-phase epitaxy, J. Cryst. Growth. 287 (2006) 566–571. doi:10.1016/J.JCRYSGRO.2005.10.077.

[8] J.R. Creighton, G.T. Wang, W.G. Breiland, M.E. Coltrin, Nature of the parasitic chemistry during AlGaInN OMVPE, J. Cryst. Growth. 261 (2004) 204–213. doi:10.1016/J.JCRYSGRO.2003.11.074.

[9] E. Gaubas, T. Ceponis, A. Jasiunas, V. Kalendra, J. Pavlov, N. Kazuchits, E. Naumchik, M. Rusetsky, Lateral scan profiles of the recombination parameters correlated with distribution of grown-in impurities in HPHT diamond, Diam. Relat. Mater. 47 (2014) 15–26. doi:10.1016/J.DIAMOND.2014.05.003.

[10] A. Tallaire, M. Lesik, V. Jacques, S. Pezzagna, V. Mille, O. Brinza, J. Meijer, B. Abel, J.F. Roch, A. Gicquel, J. Achard, Temperature dependent creation of nitrogen-vacancy centers in single crystal CVD diamond layers, Diam. Relat. Mater. 51 (2015) 55–60. doi:10.1016/J.DIAMOND.2014.11.010.

[11] F. V Kaminsky, G.K. Khachatryan, Characteristics of nitrogen and other impurities in diamond, as revealed by infrared absorption data, Can. Mineral. 39 (2001) 1733–1745. doi:10.2113/gscanmin.39.6.1733.

[12] J. Wang, P. Mulligan, L. Brillson, L.R. Cao, Review of using gallium nitride for ionizing radiation detection, Appl. Phys. Rev. 2 (2015) 31102. doi:10.1063/1.4929913.

[13] P.J. Sellin, J. Vaitkus, New materials for radiation hard semiconductor dectectors, Nucl. Instrum. Methods Phys. Res. Sect. A-Accel. Spectrom. Dect. Assoc. Equip. 557 (2006) 479–489. doi:10.1016/j.nima.2005.10.128.

[14] J.W. Tringe, A.M. Conway, T.E. Felter, W.J. Moberly Chan, J. Castelaz, V. Lordi, Y. Xia, C.G. Stevens, C. Wetzel, Radiation effects on InGaN quantum wells and GaN simultaneously probed by ion beam-induced luminescence, IEEE Trans. Nucl. Sci. 55 (2008) 3633–3637. doi:10.1109/TNS.2008.2006169.

[15] J.W. Tringe, T.E. Felter, C.E. Talley, J.D. Morse, C.G. Stevens, J.M. Castelaz, C. Wetzel, Radiation damage mechanisms for luminescence in Eu-doped GaN, J. Appl. Phys. 101 (2007) 54902. doi:10.1063/1.2696527.

[16] E. Gaubas, V. Kovalevskij, A. Kadys, M. Gaspariunas, J. Mickevicius, A. Jasiunas, V. Remeikis, A. Uleckas, A. Tekorius, J. Vaitkus, A. Velicka, In situ variations of recombination characteristics in MOCVD grown GaN epi-layers during 1.7 MeV protons irradiation, Nucl. Instruments Methods Phys. Res. Sect. B Beam Interact. with Mater. Atoms. 307 (2013) 370–372. doi:10.1016/j.nimb.2012.11.059.

[17] V. Eremin, N. Strokan, E. Verbitskaya, Z. Li, Development of transient current and charge techniques for the measurement of effective net concentration of ionized charges (N_{eff}) in the space charge region of p-n junction detectors, Nucl. Instruments Methods Phys. Res. Sect. A Accel. Spectrometers, Detect. Assoc. Equip. 372 (1996) 388–398. doi:10.1016/0168-9002(95)01295-8.

[18] C. Zhen, X. Liu, Z. Yan, H. Gong, Y. Wang, Characteristics of Au/Ti/p-diamond ohmic contacts prepared by r.f. sputtering, Surf. Interface Anal. 32 (2001) 106–109. doi:10.1002/sia.1017.

[19] K. Das, V. Venkatesan, T.P. Humphreys, Ohmic contacts on diamond by B ion implantation and

TiC-Au and $TaSi_2$-Au metallization, J. Appl. Phys. 76 (1994) 2208–2212. doi:10.1063/1.358510.
[20] G. Lindström, Radiation damage in silicon detectors, Nucl. Instruments Methods Phys. Res. Sect. A Accel. Spectrometers, Detect. Assoc. Equip. 512 (2003) 30–43. doi:10.1016/S0168-9002(03)01874-6.
[21] Z. Li, E. Verbitskaya, V. Eremin, A. Ivanov, J. Harkonen, E. Tuovinen, P. Luukka, Detector recovery/improvement via elevated-temperature-annealing (DRIVE): a new approach for Si detector applications in high radiation environment in SLHC, in: IEEE Nucl. Sci. Symp. Conf. Rec. 2005, IEEE, n.d.: pp. 1106–1111. doi:10.1109/NSSMIC.2005.1596445.
[22] D. V. Lang, Deep-level transient spectroscopy: A new method to characterize traps in semiconductors, J. Appl. Phys. 45 (1974) 3023–3032.
[23] J. Wang, P. Mulligan, L. Brillson, L.R. Cao, Review of using gallium nitride for ionizing radiation detection, Appl. Phys. Rev. 2 (2015) 31102. doi:10.1063/1.4929913.
[24] V. Moroz, H.Y. Wong, M. Choi, N. Braga, R. V. Mickevicius, Y. Zhang, T. Palacios, The impact of defects on GaN device behavior: modeling dislocations, traps, and pits, ECS J. Solid State Sci. Technol. 5 (2016) P3142–P3148. doi:10.1149/2.0211604jss.
[25] M. Huhtinen, Simulation of non-ionising energy loss and defect formation in silicon, Nucl. Instruments Methods Phys. Res. Sect. A Accel. Spectrometers, Detect. Assoc. Equip. 491 (2002) 194–215. doi:10.1016/S0168-9002(02)01227-5.
[26] C. Inguimbert, P. Arnolda, T. Nuns, G. Rolland, "Effective NIEL" in silicon: calculation using molecular dynamics simulation results, IEEE Trans. Nucl. Sci. 57 (2010) 1915–1923. doi:10.1109/TNS.2010.2049581.
[27] S. Dhomkar, J. Henshaw, H. Jayakumar, C.A. Meriles, Long-term data storage in diamond, Sci. Adv. 2 (2016) e1600911–e1600911. doi:10.1126/sciadv.1600911.
[28] L. Childress, R. Hanson, Diamond NV centers for quantum computing and quantum networks, MRS Bull. 38 (2013) 134–138. doi:10.1557/mrs.2013.20.
[29] E.R. Weber, Understanding defects in semiconductors as key to advancing device technology, Phys. B Condens. Matter. 340–342 (2003) 1–14. doi:10.1016/J.PHYSB.2003.10.001.
[30] S.J. Pearton, GaN and related materials II, CRC Press, 2000.
[31] M. Frentrup, L.Y. Lee, S.-L. Sahonta, M.J. Kappers, F. Massabuau, P. Gupta, R.A. Oliver, C.J. Humphreys, D.J. Wallis, X-ray diffraction analysis of cubic zincblende III-nitrides, J. Phys. D. Appl. Phys. 50 (2017) 433002. doi:10.1088/1361-6463/aa865e.
[32] C.-Y. Yeh, Z.W. Lu, S. Froyen, A. Zunger, Zinc-blende-wurtzite polytypism in semiconductors, Phys. Rev. B. 46 (1992) 10086–10097. doi:10.1103/PhysRevB.46.10086.
[33] S.A. Kukushkin, A. V Osipov, V.N. Bessolov, B.K. Medvedev, V.K. Nevolin, K.A. Tcarik, Substrates for epitaxy of gallium nitride: new materials and techniques, Rev.Adv.Mater.Sci. 17 (2008) 1–32. doi:10.1016/S0927-796X(02)00008-6.
[34] C. Chang, S. Lien, C. Liu, C. Shih, N.- Chen, P. Chang, H. Peng, T. Tang, W. Lien, Y. Wu, K. Wu, J. Chen, C. Liang, Y. Chen, T. Lu, T. Lin, Effect of buffer layers on electrical, optical and structural properties of AlGaN/GaN heterostructures grown on Si, Jpn. J. Appl. Phys. 48 (2006) 2616. doi:10.1143/JJAP.45.2516.
[35] A. Sakai, H. Sunakawa, A. Usui, Defect structure in selectively grown GaN films with low threading dislocation density, Appl. Phys. Lett. 71 (1998) 2259. doi:10.1063/1.120044.
[36] C. Boney, A. Carreno, A. Bensaoula, Z. Zhang, H.D. Lee, W.K. Chu, A. Vigliante, Reduction of defects in RF-MBE grown GaN on sapphire by optimization of nitridation temperature and intermediate layer parameters, in: Int. Conf. Mol. Bean Ep., IEEE, San Francisco, 2002: pp. 205–206. doi:10.1109/MBE.2002.1037831.
[37] F.K. Yam, L.L. Low, S.A. Oh, Z. Hassan, Gallium nitride: an overview of structural defects, INTECH Open Access Publisher, 2011. http://cdn.intechweb.org/pdfs/20503.pdf (accessed February 13, 2018).
[38] K. Motoki, T. Okahisa, S. Nakahata, N. Matsumoto, H. Kimura, H. Kasai, K. Takemoto, K. Uematsu, M. Ueno, Y. Kumagai, A. Koukitu, H. Seki, Growth and characterization of freestanding GaN substrates, J. Cryst. Growth. 237–239 (2002) 912–921. doi:10.1016/S0022-0248(01)02078-4.
[39] Y. Oshima, T. Eri, M. Shibata, H. Sunakawa, K. Kobayashi, T. Ichihashi, A. Usui, Preparation of freestanding GaN wafers by hydride vapor phase epitaxy with void-assisted separation, Jpn. J. Appl. Phys. 42 (2003) L1–L3. doi:10.1143/JJAP.42.L1.
[40] T. Wei, J. Yang, Y. Wei, Z. Huo, X. Ji, Y. Zhang, J. Wang, J. Li, S. Fan, Cross-stacked carbon nanotubes assisted self-separation of free-standing GaN substrates by hydride vapor phase epitaxy, Sci. Rep. 6 (2016) 28620. doi:10.1038/srep28620.

[41] D. Ehrentraut, E. Meissner, M. Bockowski, Technology of gallium nitride crystal growth, Springer-Verlag, 2010.
[42] K. Xu, J.-F. Wang, G.-Q. Ren, Progress in bulk GaN growth, Chinese Phys. B. 24 (2015) 66105. doi:10.1088/1674-1056/24/6/066105.
[43] M.E. Levinshtein, S.L. Rumyantsev, M. Shur, Properties of advanced semiconductor materials : GaN, AlN, InN, BN, SiC, SiGe, Wiley, 2001.
[44] V. Avrutin, D.J. Silversmith, Y. Mori, F. Kawamura, Y. Kitaoka, H. Morkoc, Growth of bulk GaN and AlN: progress and challenges, Proc. IEEE. 98 (2010) 1302–1315. doi:10.1109/JPROC.2010.2044967.
[45] M.O. Manasreh, III-nitride semiconductors : electrical, structural, and defects properties, Elsevier, 2000.
[46] P. Boguslawski, E.L. Briggs, J. Bernholc, Amphoteric properties of substitutional carbon impurity in GaN and AlN, Appl. Phys. Lett. 69 (1998) 233. doi:10.1063/1.117934.
[47] R. Kucharski, M. Zajac, A. Puchalski, T. Sochacki, M. Bockowski, J.L. Weyher, M. Iwinska, J. Serafinczuk, R. Kudrawiec, Z. Siemiątkowski, Ammonothermal growth of GaN crystals on HVPE-GaN seeds prepared with the use of ammonothermal substrates, J. Cryst. Growth. 427 (2015) 1–6. doi:10.1016/j.jcrysgro.2015.06.019.
[48] M. Imanishi, Y. Todoroki, K. Murakami, D. Matsuo, H. Imabayashi, H. Takazawa, M. Maruyama, M. Imade, M. Yoshimura, Y. Mori, Dramatic reduction of dislocations on a GaN point seed crystal by coalescence of bunched steps during Na-flux growth, J. Cryst. Growth. 427 (2015) 87–93. doi:10.1016/j.jcrysgro.2015.07.001.
[49] S. Raghavan, J.M. Redwing, Growth stresses and cracking in GaN films on (111) Si grown by metal-organic chemical-vapor deposition. I. AlN buffer layers, J. Appl. Phys. 98 (2005) 23514. doi:10.1063/1.1978991.
[50] R.F. Davis, T.W. Weeks, M.D. Bremser, K.S. Ailey, W.G. Perry, Growth via MOCVD and characterization of GaN and $Al_xGa_{1-x}N(0001)$ alloys for optoelectronic and microelectronic device applications, MRS Proc. 415 (1995) 3. doi:10.1557/PROC-415-3.
[51] J.E. Northrup, J. Neugebauer, Theory of GaN (1010) and (1120) surfaces, Phys. Rev. B. 53 (1996) R10477–R10480. doi:10.1103/PhysRevB.53.R10477.
[52] P.R. Tavernier, P.M. Verghese, D.R. Clarke, Photoluminescence from laser assisted debonded epitaxial GaN and ZnO films, Appl. Phys. Lett. 74 (1999) 2678. doi:10.1063/1.123934.
[53] E. V. Etzkorn, D.R. Clarke, Cracking of GaN films, J. Appl. Phys. 89 (2001) 1025–1034. doi:10.1063/1.1330243.
[54] F. Gao, Theoretical model of intrinsic hardness, Phys. Rev. B. 73 (2006) 132104. doi:10.1103/PhysRevB.73.132104.
[55] J. Singh, Physics of semiconductors and their heterostructures, McGraw-Hill, 1993.
[56] J. Isberg, E. Johansson, A.J. Whitehead, D.J. Twitchen, J. Hammersberg, S.E. Coe, T. Wikstrom, G.A. Scarsbrook, High carrier mobility in single-crystal plasma-deposited diamond, Science. 297 (2002) 1670–1672. doi:10.1126/science.1074374.
[57] H.P. Bovenkerk, F.P. Bundy, H.T. Hall, H.M. Strong, R.H. Wentorf, Preparation of diamond, Nature. 184 (1959) 1094–1098. doi:10.1038/1841094a0.
[58] M. Kamo, Y. Sato, S. Matsumoto, N. Setaka, Diamond synthesis from gas phase in microwave plasma, J. Cryst. Growth. 62 (1983) 642–644. doi:10.1016/0022-0248(83)90411-6.
[59] T. Evans, C. Phaal, Imperfections in type I and type II diamonds, Proc. R. Soc. A Math. Phys. Eng. Sci. 270 (1962) 538–552. doi:10.1098/rspa.1962.0243.
[60] Patent, Red diamond, pink diamond and method of producing the same, Sumitomo Electric Industries Ltd, 1994.
[61] G. Davies, M.F. Hamer, Optical studies of the 1.945 eV vibronic band in diamond, Proc. R. Soc. London A Math. Phys. Eng. Sci. 348 (1976) 285–298. doi:10.1098/rspa.1976.0039.
[62] R. Schirhagl, K. Chang, M. Loretz, C.L. Degen, Nitrogen-vacancy centers in diamond: nanoscale sensors for physics and biology, Annu. Rev. Phys. Chem. 65 (2014) 83–105. doi:10.1146/annurev-physchem-040513-103659.
[63] M.L. Markham, J.M. Dodson, G.A. Scarsbrook, D.J. Twitchen, G. Balasubramanian, F. Jelezko, J. Wrachtrup, CVD diamond for spintronics, Diam. Relat. Mater. 20 (2011) 134–139. doi:10.1016/j.diamond.2010.11.016.
[64] J. Chevallier, B. Theys, A. Lusson, C. Grattepain, A. Deneuville, E. Gheeraert, Hydrogen-boron interactions in p-type diamond, Phys. Rev. B. 58 (1998) 7966–7969. doi:10.1103/PhysRevB.58.7966.
[65] J. Chevallier, F. Jomard, Z. Teukam, S. Koizumi, H. Kanda, Y. Sato, A. Deneuville, M. Bernard, Hydrogen in n-type diamond, Diam. Relat. Mater. 11 (2002) 1566–1571. doi:10.1016/S0925-

9635(02)00063-8.
[66] R. Kalish, Doping of diamond, Carbon. 37 (1999) 781–785. doi:10.1016/S0008-6223(98)00270-X.
[67] S. Koizumi, M. Kamo, Y. Sato, H. Ozaki, T. Inuzuka, Growth and characterization of phosphorous doped {111} homoepitaxial diamond thin films, Appl. Phys. Lett. 71 (1998) 1065. doi:10.1063/1.119729.
[68] R. Erni, B. Freitag, P. Hartel, H. Müller, P. Tiemeijer, M. van der Stam, M. Stekelenburg, D. Hubert, P. Specht, V. Garibay-Febles, Atomic scale analysis of planar defects in polycrystalline diamond, Microsc. Microanal. 12 (2006) 492–497. doi:10.1017/S1431927606060594.
[69] J.P. Goss, B.J. Coomer, R. Jones, C.J. Fall, P.R. Briddon, S. Öberg, Extended defects in diamond: the interstitial platelet, Phys. Rev. B. 67 (2003) 165208. doi:10.1103/PhysRevB.67.165208.
[70] T. Evans, Z. Qi, The kinetics of the aggregation of nitrogen atoms in diamond, Proc. R. Soc. A Math. Phys. Eng. Sci. 381 (1982) 159–178. doi:10.1098/rspa.1982.0063.
[71] G.S. Woods, G. S., Electron microscopy of "giant" platelets on cube planes in diamond, Philos. Mag. 34 (1976) 993–1012. doi:10.1080/00318087608227724.
[72] V.C. Raman, P. Nilakantan, Reflection of X-rays with change of frequency- Part 2. The case of diamond, Proc. Indian Acad. Sci. A11 (1940) 389–397.
[73] E.J. Olivier, J.H. Neethling, R.E. Kroon, S.R. Naidoo, C.S. Allen, H. Sawada, P.A. van Aken, A.I. Kirkland, Imaging the atomic structure and local chemistry of platelets in natural type Ia diamond, Nat. Mater. 17 (2018) 243–248. doi:10.1038/s41563-018-0024-6.
[74] R.S. Sussmann, CVD diamond for electronic devices and sensors, J. Wiley, 2009.
[75] H.P. Maruska, J.J. Tietjen, The preparation and properties of vapor-deposited single-crystal-line GaN, Appl. Phys. Lett. 15 (1969) 327–329. doi:10.1063/1.1652845.
[76] E.A. Jones, F.F. Wang, D. Costinett, Review of commercial GaN power devices and GaN-based converter design challenges, IEEE J. Emerg. Sel. Top. Power Electron. 4 (2016) 707–719. doi:10.1109/JESTPE.2016.2582685.
[77] Y. Tsai, K. Lai, M. Lee, Y. Liao, B. Ooi, H. Kuo, J. He, Photon management of GaN-based optoelectronic devices via nanoscaled phenomena, Prog. Quantum Electron. 49 (2016) 1–25. doi:10.1016/J.PQUANTELEC.2016.08.001.
[78] S. Suihkonen, S. Pimputkar, J.S. Speck, S. Nakamura, Infrared absorption of hydrogen-related defects in ammonothermal GaN, Appl. Phys. Lett. 108 (2016) 202105. doi:10.1063/1.4952388.
[79] M. Sumiya, S. Fuke, Review of polarity determination and control of GaN, MRS Internet J. Nitride Semicond. Res. 9 (2004) e1. doi:10.1557/S1092578300000363.
[80] R. Velazquez, A. Aldalbahi, M. Rivera, P. Feng, Fabrications and application of single crystalline GaN for high-performance deep UV photodetectors, AIP Adv. 6 (2016) 85117. doi:10.1063/1.4961878.
[81] M. Kamo, H. Yurimoto, Y. Sato, Epitaxial growth of diamond on diamond substrate by plasma assisted CVD, Appl. Surf. Sci. 33–34 (1988) 553–560. doi:10.1016/0169-4332(88)90352-2.
[82] D. Ehrentraut, R.T. Pakalapati, D.S. Kamber, W. Jiang, D.W. Pocius, B.C. Downey, M. McLaurin, M.P. D'Evelyn, High quality, low cost ammonothermal bulk GaN substrates, Jpn. J. Appl. Phys. 52 (2013) 08JA01. doi:10.7567/JJAP.52.08JA01.
[83] K. Tsugawa, A. Hokazono, H. Noda, K. Kitatani, K. Morita, H. Kawarada, MESFETs and MOSFETs on hydrogen-terminated diamond surfaces, Mater. Sci. Forum. 264–268 (1998) 977–980. doi:10.4028/www.scientific.net/MSF.264-268.977.
[84] J. Liu, H. Ohsato, X. Wang, M. Liao, Y. Koide, Design and fabrication of high-performance diamond triple-gate field-effect transistors., Sci. Rep. 6 (2016) 34757. doi:10.1038/srep34757.
[85] M. Willander, M. Friesel, Q. Wahab, B. Straumal, Silicon carbide and diamond for high temperature device applications, J. Mater. Sci. Mater. Electron. 17 (2006) 1–25. doi:10.1007/s10854-005-5137-4.
[86] M. Hodgson, A. Lohstroh, P. Sellin, D. Thomas, Characterization of silicon carbide and diamond detectors for neutron applications, Meas. Sci. Technol. 28 (2017) 105501. doi:10.1088/1361-6501/aa7f8b.
[87] E.M. Handy, M. V. Rao, O.W. Holland, P.H. Chi, K.A. Jones, M.A. Derenge, R.D. Vispute, T. Venkatesan, Al, B, and Ga ion-implantation doping of SiC, J. Electron. Mater. 29 (2000) 1340–1345. doi:10.1007/s11664-000-0135-z.
[88] J.M. Mánuel, F.M. Morales, R. García, R. Aidam, L. Kirste, O. Ambacher, Threading dislocation propagation in AlGaN/GaN based HEMT structures grown on Si(111) by plasma assisted molecular beam epitaxy, J. Cryst. Growth. 357 (2012) 35–41. doi:10.1016/J.JCRYSGRO.2012.07.037.

[89] D. Zhu, C.J. Humphreys, Low-cost high-efficiency GaN LED on large-area Si substrate, in: CS MANTECH Conf., New Orleans, 2013: pp. 269–272.
[90] M.A. Moram, M.E. Vickers, X-ray diffraction of III-nitrides, Reports Prog. Phys. 72 (2009) 36502. doi:10.1088/0034-4885/72/3/036502.
[91] Tapping Mode - Imaging Modes of AFM | Bruker, (n.d.). www.bruker.com (accessed April 13, 2018).
[92] W. Deferme, A. Bogdan, G. Bogdan, K. Haenen, W. De Ceuninck, M. Nesládek, Electrical transport measurements and emission properties of freestanding single crystalline CVD diamond samples, Phys. Status Solidi. 204 (2007) 3017–3022. doi:10.1002/pssa.200776343.
[93] H. Pernegger, S. Roe, P. Weilhammer, V. Eremin, H. Frais-Kölbl, E. Griesmayer, H. Kagan, S. Schnetzer, R. Stone, W. Trischuk, D. Twitchen, A. Whitehead, Charge-carrier properties in synthetic single-crystal diamond measured with the transient-current technique, J. Appl. Phys. 97 (2005) 73704. doi:10.1063/1.1863417.
[94] C.E. Nebel, M. Stutzmann, F. Lacher, P. Koidl, R. Zachai, Carrier trapping and release in CVD-diamond films, Diam. Relat. Mater. 7 (1998) 556–559. doi:10.1016/S0925-9635(97)00203-3.
[95] E. Gaubas, T. Ceponis, J.V. Vaitkus, Pulsed capacitance technique for evaluation of barrier structures, LAMBERT Academic Publishing, Saarbrucken-Berlin, 2013.
[96] E. Gaubas, A. Uleckas, J. Vaitkus, J. Raisanen, P. Tikkanen, Instrumentation for the *in situ* control of carrier recombination characteristics during irradiation by protons, Rev. Sci. Instrum. 81 (2010) 53303. doi:10.1063/1.3429944.
[97] E. Gaubas, A. Kaniava, Determination of recombination parameters in silicon wafers by transient microwave absorption, Rev. Sci. Instrum. 67 (1998) 2339. doi:10.1063/1.1146943.
[98] T.H. Gfroerer, Gfroerer, T. H., Photoluminescence in analysis of surfaces and interfaces, in: Encycl. Anal. Chem., John Wiley & Sons, Ltd, Chichester, UK, 2006. doi:10.1002/9780470027318.a2510.
[99] L. Bergman, R.J. Nemanich, Raman spectroscopy for characterization of hard, wide-bandgap semiconductors: Diamond, GaN, GaAlN, AlN, BN, Annu. Rev. Mater. Sci. 26 (1996) 551–579. doi:10.1146/annurev.ms.26.080196.003003.
[100] Z. Li, Systematic modelling and comparisons of capacitance and current-based microscopic defect analysis techniques for measurements of high-resistivity silicon detectors after irradiation, Nucl. Instruments Methods Phys. Res. Sect. A Accel. Spectrometers, Detect. Assoc. Equip. 403 (1998) 399–416. doi:10.1016/S0168-9002(97)01099-1.
[101] C.J. Li, Z. Li, Development of current-based microscopic defect analysis methods and associated optical filling techniques for the investigation on highly irradiated high resistivity silicon detectors, Nucl. Instruments Methods Phys. Res. Sect. A Accel. Spectrometers, Detect. Assoc. Equip. 364 (1995) 108–117. doi:10.1016/0168-9002(95)00437-8.
[102] A. Avila García, M. Alfredo, R. Barranca, Computerized DLTS system to characterize deep levels in semiconductors, Rev. Mex. Fis. 48 (2002) 539–547.
[103] FT 1030 DLTS System, (n.d.). www.phystech.de (accessed March 8, 2018).
[104] E. Gaubas, A. Kaniava, J. Vaitkus, Investigation of recombination parameters in silicon structures by infrared and microwave transient absorption techniques, Semicond. Sci. Technol. 12 (1997) 1–10. doi:10.1088/0268-1242/12/1/002.
[105] N.G. Nilsson, K.G. Svantesson, The role of free carrier absorption in laser annealing of silicon at 1.06μm, J. Phys. D. Appl. Phys. 13 (1980) 39–44. doi:10.1088/0022-3727/13/1/013.
[106] V. Rumbauskas, D. Meskauskaite, T. Ceponis, E. Gaubas, Anneal induced transforms of radiation defects in heavily electron irradiated Si diodes, J. Instrum. 11 (2016) P09004–P09004. doi:10.1088/1748-0221/11/09/P09004.
[107] T. Aoki, Photoluminescence spectroscopy, John Wiley & Sons, Inc., Hoboken, NJ, USA, 2012. doi:10.1002/0471266965.com058.pub2.
[108] E. Gaubas, E. Simoen, J. Vanhellemont, Review—Carrier lifetime spectroscopy for defect characterization in semiconductor materials and devices, ECS J. Solid State Sci. Technol. 5 (2016) P3108–P3137. doi:10.1149/2.0201604jss.
[109] G. Lucovsky, On the photoionization of deep impurity centers in semiconductors, Solid State Commun. 3 (1965) 299–302. doi:10.1016/0038-1098(65)90039-6.
[110] A. Chantre, G. Vincent, D. Bois, Deep-level optical spectroscopy in GaAs, Phys. Rev. B. 23 (1981) 5335–5359. doi:10.1103/PhysRevB.23.5335.
[111] J. Bourgoin, M. Lannoo, Point Defects in Semiconductors II, Springer Berlin Heidelberg, Berlin, Heidelberg, 1983. doi:10.1007/978-3-642-81832-5.
[112] A.M. Stoneham, Phonon coupling and photoionisation cross-sections in semiconductors, J. Phys. C Solid State Phys. 12 (1979) 891–897. doi:10.1088/0022-3719/12/5/018.

[113] G. Lamouche, Y. Lépine, Impurity photoionization in the presence of a static electric field: Phonon coupling and non-uniform electric field effects, J. Appl. Phys. 78 (1995) 4015–4019. doi:10.1063/1.359924.
[114] A.A. Kopylov, A.N. Pikhtin, Effect of temperature on the optical-absorption spectra of deep centers in semiconductors, Sov. Phys. Solid State. 16 (1975) 1200.
[115] K. Huang, A. Rhys, Theory of light absorption and non-radiative transitions in F-centres, Proc. R. Soc. A Math. Phys. Eng. Sci. 204 (1950) 406–423. doi:10.1098/rspa.1950.0184.
[116] A. Alkauskas, M.D. McCluskey, C.G. Van de Walle, Tutorial: Defects in semiconductors—Combining experiment and theory, J. Appl. Phys. 119 (2016) 181101. doi:10.1063/1.4948245.
[117] K.M. Salikhov, N.E. Zavoiskaya, Zavoisky and the discovery of EPR, Resonance. 20 (2015) 963–968. doi:10.1007/s12045-015-0264-6.
[118] A. Schweiger, G. Jeschke, Principles of pulse electron paramagnetic resonance, Oxford University Press, 2001.
[119] D.M. Murphy, EPR (Electron Paramagnetic Resonance) spectroscopy of polycrystalline oxide systems, in: Met. Oxide Catal., Wiley-VCH Verlag GmbH & Co. KGaA, Weinheim, Germany, 2009: pp. 1–50. doi:10.1002/9783527626113.ch1.
[120] D.J. Gardiner, P.R. Graves, Practical Raman Spectroscopy, Springer Berlin Heidelberg, 1989.
[121] H. Harima, Properties of GaN and related compounds studied by means of Raman scattering, J. Phys. Condens. Matter. 14 (2002) R967–R993. doi:10.1088/0953-8984/14/38/201.
[122] Ammono-top quality GaN manufacturer, (n.d.). http://ammono.com/ (accessed March 9, 2018).
[123] L. Snoj, G. Žerovnik, A. Trkov, Computational analysis of irradiation facilities at the JSI TRIGA reactor, Appl. Radiat. Isot. 70 (2012) 483–488. doi:10.1016/J.APRADISO.2011.11.042.
[124] M. Moll, Radiation tolerant semiconductor sensors for tracking detectors, Nucl. Instrum. Methods Phys. Res. Sect. A-Accel. Spectrom. Dect. Assoc. Equip. 565 (2006) 202–211. doi:10.1016/j.nima.2006.05.001.
[125] EasySpin - EPR spectrum simulation, (n.d.). www.easyspin.org (accessed December 9, 2016).
[126] T. Graf, M. Gjukic, M. Hermann, M.S. Brandt, M. Stutzmann, O. Ambacher, Spin resonance investigations of Mn^{2+} in wurtzite GaN and AlN films, Phys. Rev. B. 67 (2003) 165215. doi:10.1103/PhysRevB.67.165215.
[127] G.R. Eaton, S.S. Eaton, D.P. Barr, R.T. Weber, Quantitative EPR, Springer, 2010.
[128] M.E. Zvanut, Y. Uprety, J. Dashdorj, M. Moseley, W. Alan Doolittle, Passivation and activation of Mg acceptors in heavily doped GaN, J. Appl. Phys. 110 (2011) 44508. doi:10.1063/1.3626461.
[129] N.T. Son, C.G. Hemmingsson, T. Paskova, K.R. Evans, A. Usui, N. Morishita, T. Ohshima, J. Isoya, B. Monemar, E. Janzén, Identification of the gallium vacancy-oxygen pair defect in GaN, Phys. Rev. B - Condens. Matter Mater. Phys. 80 (2009) 153202. doi:10.1103/PhysRevB.80.153202.
[130] N.T. Son, C.G. Hemmingsson, N. Morishita, T. Ohshima, T. Paskova, K.R. Evans, A. Usui, J. Isoya, B. Monemar, E. Janzén, Radiation-induced defects in GaN, Phys. Scr. T141 (2010) 14015. doi:10.1088/0031-8949/2010/T141/014015.
[131] H.J. Von Bardeleben, J.L. Cantin, U. Gerstmann, A. Scholle, S. Greulich-Weber, E. Rauls, M. Landmann, W.G. Schmidt, A. Gentils, J. Botsoa, M.F. Barthe, Identification of the nitrogen split interstitial $(N\text{-}N)_N$ in GaN, Phys. Rev. Lett. 109 (2012) 206402. doi:10.1103/PhysRevLett.109.206402.
[132] H.J. von Bardeleben, J.L. Cantin, H. Vrielinck, F. Callens, L. Binet, E. Rauls, U. Gerstmann, Nitrogen split interstitial center $(N{-}N)_N$ in GaN: High frequency EPR and ENDOR study, Phys. Rev. B. 90 (2014) 85203. doi:10.1103/PhysRevB.90.085203.
[133] M.I. Zhang, R.X. Yang, X.L. Wang, S.F. Liu, Neutron irradiation effect on GaN-based materials, ECS Trans. 66 (2015) 33–52. doi:10.1149/06601.0033ecst.
[134] U. Haboeck, H. Siegle, A. Hoffmann, C. Thomsen, Lattice dynamics in GaN and AlN probed with first- and second-order Raman spectroscopy, Phys. Status Solidi. 0 (2003) 1710–1731. doi:10.1002/pssc.200303130.
[135] G. Callsen, M.R. Wagner, T. Kure, J.S. Reparaz, M. Bügler, J. Brunnmeier, C. Nenstiel, A. Hoffmann, M. Hoffmann, J. Tweedie, Z. Bryan, S. Aygun, R. Kirste, R. Collazo, Z. Sitar, Optical signature of Mg-doped GaN: Transfer processes, Phys. Rev. B - Condens. Matter Mater. Phys. 86 (2012). doi:10.1103/PhysRevB.86.075207.
[136] H. Lei, H.S. Leipner, J. Schreiber, J.L. Weyher, T. Wosiński, I. Grzegory, Raman and cathodoluminescence study of dislocations in GaN, J. Appl. Phys. 92 (2002) 6666–6670. doi:10.1063/1.1518793.
[137] P. Perlin, T. Suski, H. Teisseyre, M. Leszczynski, I. Grzegory, J. Jun, S. Porowski, P.

Bogusławski, J. Bernholc, J.C. Chervin, A. Polian, T.D. Moustakas, Towards the identification of the dominant donor in GaN, Phys. Rev. Lett. 75 (1995) 296–299. doi:10.1103/PhysRevLett.75.296.
[138] F. Tuomisto, T. Kuittinen, M. Zajac, R. Doradzinski, D. Wasik, Vacancy-hydrogen complexes in ammonothermal GaN, J. Cryst. Growth. 403 (2014) 114–118. doi:10.1016/j.jcrysgro.2014.06.005.
[139] M.P. D'Evelyn, H.C. Hong, D.S. Park, H. Lu, E. Kaminsky, R.R. Melkote, P. Perlin, M. Lesczynski, S. Porowski, R.J. Molnar, Bulk GaN crystal growth by the high-pressure ammonothermal method, J. Cryst. Growth. 300 (2007) 11–16. doi:10.1016/j.jcrysgro.2006.10.232.
[140] W.H. Sun, K.M. Chen, Z.J. Yang, J. Li, Y.Z. Tong, S.X. Jin, G.Y. Zhang, Q.L. Zhang, G.G. Qin, Using Fourier transform infrared grazing incidence reflectivity to study local vibrational modes in GaN, J. Appl. Phys. 85 (1999) 6430. doi:10.1063/1.370148.
[141] M.O. Manasreh, J.M. Baranowski, K. Pakula, H.X. Jiang, J. Lin, Localized vibrational modes of carbon-hydrogen complexes in GaN, Appl. Phys. Lett. 75 (1999) 659. doi:10.1063/1.124473.
[142] G.C. Yi, B.W. Wessels, Carbon–hydrogen complexes in vapor phase epitaxial GaN, Appl. Phys. Lett. 70 (1997) 357. doi:10.1063/1.118388.
[143] S. Pimputkar, S. Suihkonen, M. Imade, Y. Mori, J.S. Speck, S. Nakamura, Free electron concentration dependent sub-bandgap optical absorption characterization of bulk GaN crystals, J. Cryst. Growth. 432 (2015) 49–53. doi:10.1016/j.jcrysgro.2015.09.016.
[144] A. Wolos, M. Palczewska, M. Zajac, J. Gosk, M. Kaminska, A. Twardowski, M. Bockowski, I. Grzegory, S. Porowski, Optical and magnetic properties of Mn in bulk GaN, Phys. Rev. B. 69 (2004) 115210. doi:10.1103/PhysRevB.69.115210.
[145] M.A. Reshchikov, H. Morkoç, Luminescence properties of defects in GaN, J. Appl. Phys. 97 (2005) 61301. doi:10.1063/1.1868059.
[146] M.A. Reshchikov, H. Morkoç, S.S. Park, K.Y. Lee, Two charge states of dominant acceptor in unintentionally doped GaN: evidence from photoluminescence study, Appl. Phys. Lett. 81 (2002) 4970. doi:10.1063/1.1531227.
[147] J. Rodrigues, M. Peres, M.J. Soares, K. Lorenz, J.G. Marques, A.J. Neves, T. Monteiro, Influence of neutron irradiation and annealing on the optical properties of GaN, Phys. Status Solidi C. (2012) 1–5. doi:10.1002/pssc.201100200.
[148] M.A. Reshchikov, D.O. Demchenko, A. Usikov, H. Helava, Y. Makarov, Carbon defects as sources of the green and yellow luminescence bands in undoped GaN, Phys. Rev. B. 90 (2014) 235203. doi:10.1103/PhysRevB.90.235203.
[149] J.L. Lyons, A. Janotti, C.G. Van de Walle, Carbon impurities and the yellow luminescence in GaN, Appl. Phys. Lett. 97 (2010) 152108. doi:10.1063/1.3492841.
[150] D.O. Demchenko, I.C. Diallo, M.A. Reshchikov, Yellow luminescence of gallium nitride generated by carbon defect complexes, Phys. Rev. Lett. 110 (2013) 87404. doi:10.1103/PhysRevLett.110.087404.
[151] R. Dingle, M. Ilegems, Donor-acceptor pair recombination in GaN, Solid State Commun. 9 (1971) 175–180. doi:10.1016/0038-1098(71)90112-8.
[152] D.G. Thomas, J.J. Hoizreld, M. Augustyniak, Kinetics of radiative recombination at randomly distributed donors and acceptors, Phys. Rev. 140 (1965) A202.
[153] T. Graf, M. Gjukic, M.S. Brandt, M. Stutzmann, O. Ambacher, The Mn acceptor level in group III nitrides, Appl. Phys. Lett. 81 (2002) 5159. doi:10.1063/1.1530374.
[154] S. Sintonen, S. Wahl, S. Richter, S. Meyer, S. Suihkonen, T. Schulz, K. Irmscher, A.N. Danilewsky, T.O. Tuomi, R. Stankiewicz, M. Albrecht, Evolution of impurity incorporation during ammonothermal growth of GaN, J. Cryst. Growth. (2016). doi:10.1016/j.jcrysgro.2016.08.044.
[155] R.Y. Korotkov, J.M. Gregie, B.W. Wessels, Optical properties of the deep Mn acceptor in GaN:Mn, Appl. Phys. Lett. 80 (2002) 1731–1733. doi:10.1063/1.1456544.
[156] Z. Zhang, A.R. Arehart, E.C.H. Kyle, J. Chen, E.X. Zhang, D.M. Fleetwood, R.D. Schrimpf, J.S. Speck, S.A. Ringel, Proton irradiation effects on deep level states in Mg-doped p-type GaN grown by ammonia-based molecular beam epitaxy, Appl. Phys. Lett. 106 (2015) 22104. doi:10.1063/1.4905783.
[157] A. Armstrong, A.R. Arehart, B. Moran, S.P. DenBaars, U.K. Mishra, J.S. Speck, S.A. Ringel, Impact of carbon on trap states in n-type GaN grown by metalorganic chemical vapor deposition, Appl. Phys. Lett. 84 (2004) 374–376. doi:10.1063/1.1643540.
[158] Z. Zhang, C.A. Hurni, A.R. Arehart, J. Yang, R.C. Myers, J.S. Speck, S.A. Ringel, Deep traps in nonpolar m-plane GaN grown by ammonia-based molecular beam epitaxy, Appl. Phys. Lett.

100 (2012) 52114–42102. doi:10.1063/1.126580.
[159] G.C. Yi, B.W. Wessels, Deep level defects in Mg-doped GaN, in: MRS Proc., Cambridge University Press, Pittsburgh, 1996: p. 525. doi:10.1557/PROC-423-525.
[160] C.H. Qiu, J.I. Pankove, Deep levels and persistent photoconductivity in GaN thin films, Appl. Phys. Lett. 70 (1997) 1983–1985. doi:10.1063/1.118799.
[161] E. Gaubas, T. Ceponis, L. Deveikis, D. Meskauskaite, S. Miasojedovas, J. Mickevicius, J. Pavlov, K. Pukas, J. Vaitkus, M. Velicka, M. Zajac, R. Kucharski, Study of neutron irradiated structures of ammonothermal GaN, J. Phys. D. Appl. Phys. 50 (2017) 135102. doi:10.1088/1361-6463/aa5c6c.
[162] J. Pavlov, T. Čeponis, E. Gaubas, D. Meskauskaite, I. Reklaitis, J. Vaitkus, R. Grigonis, V. Sirutkaitis, Comparative study of deep levels in HVPE and MOCVD GaN by combining O-DLTS and pulsed photo-ionization spectroscopy, J. Instrum. 10 (2015) C12015–C12015. doi:10.1088/1748-0221/10/12/C12015.
[163] E. Gaubas, T. Čeponis, A. Jasiunas, E. Jelmakas, S. Juršėnas, A. Kadys, T. Malinauskas, A. Tekorius, P. Vitta, Study of carrier recombination transient characteristics in MOCVD grown GaN dependent on layer thickness, AIP Adv. 3 (2013) 112128. doi:10.1063/1.4835056.
[164] M. Meneghini, G. Meneghesso, E. Zanoni, Power GaN Devices : Materials, Applications and Reliability, Springer, 2017.
[165] R.W. Erickson, D. Maksimović, Fundamentals of power electronics, Kluwer Academic, 2001.
[166] U. Honda, Y. Yamada, Y. Tokuda, K. Shiojima, Deep levels in n-GaN doped with carbon studied by deep level and minority carrier transient spectroscopies, Jpn. J. Appl. Phys. 51 (2012) 04DF04. doi:10.1143/JJAP.51.04DF04.
[167] A.D. Kurtz, S.A. Kulin, B.L. Averbach, Effect of dislocations on the minority carrier lifetime in semiconductors, Phys. Rev. 101 (1956) 1285–1291. doi:10.1103/PhysRev.101.1285.
[168] Y. Sugawara, Y. Ishikawa, A. Watanabe, M. Miyoshi, T. Egawa, Observation of reaction between a-type dislocations in GaN layer grown on 4-in. Si(111) substrate with AlGaN/AlN strained layer superlattice after dislocation propagation, J. Cryst. Growth. 468 (2017) 536–540. doi:10.1016/J.JCRYSGRO.2016.11.010.
[169] Y. Yao, Y. Ishikawa, Y. Sugawara, D. Yokoe, M. Sudo, N. Okada, K. Tadatomo, Revelation of dislocations in HVPE GaN single crystal by KOH etching with Na_2O_2 additive and cathodoluminescence mapping, Superlattices Microstruct. 99 (2016) 83–87. doi:10.1016/J.SPMI.2016.05.002.
[170] G.D. Papasouliotis, J. Su, B. Krishnan, R. Arif, Epitaxial III-nitride film growth in a single wafer rotating disk MOCVD reactor, ECS Trans. 69 (2015) 73–95. doi:10.1149/06911.0073ecst.
[171] J.R. Creighton, W.G. Breiland, M.E. Coltrin, R.P. Pawlowski, Gas-phase nanoparticle formation during AlGaN metalorganic vapor phase epitaxy, Appl. Phys. Lett. 81 (2002) 2626–2628. doi:10.1063/1.1510580.
[172] H.F. Mataré, Defect electronics in semiconductors, Wiley-Interscience, 1971.
[173] M. Haugk, J. Elsner, T. Frauenheim, T.E.M. Staab, C.D. Latham, R. Jones, H.S. Leipner, T. Heine, G. Seifert, M. Sternberg, Structures, energetics and electronic properties of complex III-V semiconductor systems, Phys. Status Solidi. 217 (2000) 473–511. doi:10.1002/(SICI)1521-3951(200001)217:1<473::AID-PSSB473>3.0.CO;2-N.
[174] D. Wang, M. Ichikawa, S.S. Yoshida, Dislocation core structures in GaN grown on Si(111) substrate, Philos. Mag. Lett. 82 (2002) 119–124. doi:10.1080/095008302317262615.
[175] J.C. Phillips, Microscopic aspects of stretched exponential relaxation (SER) in homogeneous molecular and network glasses and polymers, J. Non. Cryst. Solids. 357 (2011) 3853–3865. doi:10.1016/j.jnoncrysol.2011.08.001.
[176] H. Tang, Z.Q. Fang, S. Rolfe, J.A. Bardwell, S. Raymond, Growth kinetics and electronic properties of unintentionally doped semi-insulating GaN on SiC and high-resistivity GaN on sapphire grown by ammonia molecular-beam epitaxy, J. Appl. Phys. 107 (2010) 103701. doi:10.1063/1.3415527.
[177] A.M. Fischer, Y.O. Wei, F.A. Ponce, M. Moseley, B. Gunning, W.A. Doolittle, Highly luminescent, high-indium-content InGaN film with uniform composition and full misfit-strain relaxation, Appl. Phys. Lett. 103 (2013) 131101. doi:10.1063/1.4822122.
[178] Optosupply Limited, (n.d.). http://www.optosupply.com/ (accessed April 26, 2017).
[179] E. Gaubas, T. Ceponis, A. Jasiunas, A. Uleckas, J. Vaitkus, E. Cortina, O. Militaru, Correlated evolution of barrier capacitance charging, generation, and drift currents and of carrier lifetime in Si structures during 25 MeV neutrons irradiation, Appl. Phys. Lett. 101 (2012) 232104. doi:10.1063/1.4769370.
[180] E. Gaubas, I. Brytavskyi, T. Ceponis, V. Kalendra, A. Tekorius, Spectroscopy of deep traps in

Cu2S-CdS junction structures, Materials (Basel). 5 (2012) 2597–2608.
[181] N. Nepal, M.L. Nakarmi, J.Y. Lin, H.X. Jiang, Photoluminescence studies of impurity transitions in AlGaN alloys, Appl. Phys. Lett. 89 (2006) 92107. doi:10.1063/1.2337856.
[182] K.H. Lee, J.H. Crawford, Luminescence of the F center in sapphire, Phys. Rev. B. 19 (1979) 3217–3221. doi:10.1103/PhysRevB.19.3217.
[183] A. Castaldini, A. Cavallini, A. Castaldini, L. Polenta, Deep levels and irradiation effects in n-GaN, J. Phys. Condens. Matter. 12 (2000) 10161–10167. doi:10.1088/0953-8984/12/49/315.
[184] A.Y. Polyakov, S.J. Pearton, P. Frenzer, F. Ren, L. Liu, J. Kim, Radiation effects in GaN materials and devices, J. Mater. Chem. C. 1 (2013) 877–887. doi:10.1039/C2TC00039C.
[185] E.E. Patrick, M. Choudhury, F. Ren, S.J. Pearton, M.E. Law, Simulation of radiation effects in AlGaN/GaN HEMTs, ECS J. Solid State Sci. Technol. 4 (2015) Q21–Q25. doi:10.1149/2.0181503jss.
[186] B.D. Weaver, T.J. Anderson, A.D. Koehler, J.D. Greenlee, J.K. Hite, D.I. Shahin, F.J. Kub, K.D. Hobart, On the radiation tolerance of AlGaN/GaN HEMTs, ECS J. Solid State Sci. Technol. 5 (2016) Q208–Q212. doi:10.1149/2.0281607jss.
[187] E. Patrick, M.E. Law, L. Liu, C. Velez Cuervo, Y. Xi, F. Ren, S.J. Pearton, Modeling proton irradiation in AlGaN/GaN HEMTs: understanding the increase of critical voltage, IEEE Trans. Nucl. Sci. 60 (2013) 4103–4108. doi:10.1109/TNS.2013.2286115.
[188] H.M. Strong, R.M. Chrenko, Diamond growth rates and physical properties of laboratory-made diamond, J. Phys. Chem. 75 (1971) 1838–1843. doi:10.1021/j100681a014.
[189] Element six synthetic industrial diamonds, (n.d.). https://www.e6.com/en/Home (accessed April 11, 2018).
[190] S. Nokhrin, J. Rosa, M. Vanecek, A.G. Badalyan, M. Nesladek, EPR study of preferential orientation of crystallites in N-doped high quality CVD diamond, Diam. Relat. Mater. 10 (2001) 480–484. doi:10.1016/S0925-9635(00)00539-2.
[191] J. Isoya, H. Kanda, J.R. Norris, J. Tang, M.K. Bowman, Fourier-transform and continuous-wave EPR studies of nickel in synthetic diamond: Site and spin multiplicity, Phys. Rev. B. 41 (1990) 3905–3913. doi:10.1103/PhysRevB.41.3905.
[192] K. Iakoubovskii, G.J. Adriaenssens, Optical detection of defect centers in CVD diamond, Diam. Relat. Mater. 9 (2000) 1349–1356. doi:10.1016/S0925-9635(00)00248-X.
[193] A. Yelisseyev, Y. Babich, V. Nadolinny, D. Fisher, B. Feigelson, Spectroscopic study of HPHT synthetic diamonds, as grown at 1500°C, Diam. Relat. Mater. 11 (2002) 22–37. doi:10.1016/S0925-9635(01)00526-X.
[194] W. Shockley, Currents to conductors induced by a moving point charge, J. Appl. Phys. 9 (1938) 635–636. doi:10.1063/1.1710367.
[195] S. Ramo, Currents induced by electron motion, Proc. IRE. 27 (1939) 584–585. doi:10.1109/JRPROC.1939.228757.
[196] Z. He, Review of the Shockley-Ramo theorem and its application in semiconductor gamma-ray detectors, Nucl. Instruments Methods Phys. Res. Sect. A Accel. Spectrometers, Detect. Assoc. Equip. 463 (2001) 250–267. doi:10.1016/S0168-9002(01)00223-6.
[197] E. Gaubas, T. Ceponis, V. Kalesinskas, Currents Induced by Injected Charge in Junction Detectors, Sensors. 13 (2013) 12295–12328. doi:10.3390/s130912295.
[198] P. Blood, J.W. Orton, The electrical characterization of semiconductors:majority carriers and eletron states, Academic Press Inc., San Diego, 1992.
[199] E. Gaubas, J. Vaitkus, K.M. Smith, Monitoring of carrier lifetime in GaAs substrate–epi-layer structures by space-resolved transient microwave absorption, Nucl. Instruments Methods Phys. Res. Sect. A Accel. Spectrometers, Detect. Assoc. Equip. 460 (2001) 35–40. doi:10.1016/S0168-9002(00)01092-5.
[200] E. Gaubas, J. Vaitkus, E. Simoen, C. Claeys, J. Vanhellemont, Excess carrier cross-sectional profiling technique for determination of the surface recombination velocity, Mater. Sci. Semicond. Process. 4 (2001) 125–131. doi:10.1016/S1369-8001(00)00140-2.
[201] B.M. Budak, A collection of problems on mathematical physics, Pergamon Press, 1964.
[202] E. Gaubas, T. Čeponis, J. Vaitkus, J. Raisanen, Study of variations of the carrier recombination and charge transport parameters during proton irradiation of silicon pin diode structures, AIP Adv. 1 (2011) 22143. doi:10.1063/1.3605715.
[203] I. Mandić, V. Cindro, A. Gorišek, G. Kramberger, M. Mikuž, M. Zavrtanik, Edge-TCT measurements with the laser beam directed parallel to the strips, J. Instrum. 10 (2015) P08004–P08004. doi:10.1088/1748-0221/10/08/P08004.
[204] E. Gaubas, T. Ceponis, V. Kalesinskas, J. Pavlov, J. Vysniauskas, Simulations of operation dynamics of different type GaN particle sensors, Sensors. 15 (2015) 5429–5473.

doi:10.3390/s150305429.
[205] J.D. Jackson, Classical electrodynamics, Wiley, 1962.
[206] O. Dushek, S. V Kuzmin, The fields of a moving point charge: a new derivation from Jefimenko's equations, Eur. J. Phys. 25 (2004) 343–350. doi:10.1088/0143-0807/25/3/001.
[207] B. Di Bartolo, Classical theory of electromagnetism, World Scientific, 2004.
[208] M. Pomorski, E. Berdermann, M. Ciobanu, A. Martemyianov, P. Moritz, M. Rebisz, B. Marczewska, Characterisation of single crystal CVD diamond particle detectors for hadron physics experiments, Phys. Status Solidi. 202 (2005) 2199–2205. doi:10.1002/pssa.200561929.
[209] A. Lohstroh, P.J. Sellin, S.G. Wang, A.W. Davies, J.M. Parkin, Mapping of polarization and detrapping effects in synthetic single crystal chemical vapor deposited diamond by ion beam induced charge imaging, J. Appl. Phys. 101 (2007) 63711. doi:10.1063/1.2653669.
[210] H. Spieler, Semiconductor Detector Systems, Oxford University Press, 2005. doi:10.1093/acprof:oso/9780198527848.001.0001.
[211] E. Gaubas, A. Kadys, A. Uleckas, J. Vaitkus, Investigation of carrier recombination in Si heavily irradiated by neutrons, Acta Phys, Pol. 113 (2008) 829. doi:10.12693/APhysPolA.113.829.
[212] M.L. David, E. Oliviero, C. Blanchard, J. Barbot, Generation of defects induced by MeV proton implantation in silicon - influence of nuclear losses, Nucl. Instruments Methods Phys. Res. Sect. B Beam Interact. with Mater. Atoms. 186 (2002) 309–312. doi:10.1016/S0168-583X(01)00895-3.
[213] M. Bruzzi, D. Menichelli, M. Scaringella, J. Härkönen, E. Tuovinen, Z. Li, Thermal donors formation via isothermal annealing in magnetic Czochralski high resistivity silicon, J. Appl. Phys. 99 (2006) 93706. doi:10.1063/1.2192307.
[214] N. Ganagona, L. Vines, E. V. Monakhov, B.G. Svensson, Formation kinetics of trivacancy-oxygen pairs in silicon, J. Appl. Phys. 116 (2014) 124510. doi:10.1063/1.4896066.
[215] I. Pintilie, E. Fretwurst, G. Lindström, Cluster related hole traps with enhanced-field-emission—the source for long term annealing in hadron irradiated Si diodes, Appl. Phys. Lett. 92 (2008) 24101. doi:10.1063/1.2832646.